UNIVERSITY OF CALIFORNIA,
IRVINE

Nonlinear Spin-Torque Oscillator Dynamics and Spin-Torque Microwave Detectors

DISSERTATION

submitted in partial satisfaction of the requirements
for the degree of

DOCTOR OF PHILOSOPHY

in Physics

by

Jieyi Zhang

Dissertation Committee:
Professor Ilya Krivorotov, Chair
Professor Jing Xia
Professor Zuzanna Siwy

2017

DEDICATION

To my parents, Ming and Lingfeng.

TABLE OF CONTENTS

Page

LIST OF FIGURES **v**

LIST OF TABLES **x**

ACKNOWLEDGMENTS **xi**

CURRICULUM VITAE **xii**

ABSTRACT OF THE DISSERTATION **xiv**

1 Introduction and Background **1**
- 1.1 Magnetization Dynamics . . . 2
- 1.2 Giant and Tunneling Magnetoresistances . . . 5
- 1.3 Spin Transfer Torque . . . 9
- 1.4 Spin Torque Oscillator . . . 14
- 1.5 Spin Torque Ferromagnetic Resonance . . . 15
  - 1.5.1 Conventional Ferromagnetic Resonance . . . 15
  - 1.5.2 Spin Torque assisted Ferromagnetic Resonance . . . 17

2 Nonlinear Spin Torque Oscillator Dynamics **20**
- 2.1 Experimental Methods . . . 20
  - 2.1.1 Microwave Probe Stations . . . 20
    - 2.1.1.1 Probe Usage and Maintenance . . . 22
  - 2.1.2 Time Domain Measurement of STO Dynamics . . . 24
- 2.2 Angular Dependence of GMR . . . 28
- 2.3 Characterization in Frequency Domain . . . 36
- 2.4 Analysis of Time Domain Data . . . 42
- 2.5 Macrospin Simulations . . . 52
  - 2.5.1 Interactions with Stochastic Field . . . 57
  - 2.5.2 Analysis of Macrospin Simulation Results . . . 58
- 2.6 Calculation in the Fokker-Planck Theory . . . 60
  - 2.6.1 Introduction of General Fokker-Planck Equation . . . 60
  - 2.6.2 Calculations in the Effective Energy Framework . . . 64
  - 2.6.3 Result Analysis in comparison with Experiment . . . 67

3 Microwave Radiation Detector based on Spin Torque Diode Effect 74
3.1 Detector Design 75
3.2 Experimental Results 81
3.3 Discussion 88

4 Frequency Determination by a pair of Spin-Torque Microwave Detectors 92
4.1 Introduction 92
4.2 Theory 93
4.3 Experiment 98
4.4 Results and Discussion 99

5 Conclusion 105

Bibliography 108

A Appendices 113
A.1 Sliding FFT Angle Mapping for Time Traces for Multi-currents 113
A.2 Mapping distributions between real signals and toy model 122
A.3 Macrospin Simulation with Stochastic Fields 127
A.4 Derivation of E_{eff} via Fokker-Planck Approach 136
A.5 E_{eff} calculation via Fokker-Planck Approach 141

LIST OF FIGURES

Page

1.1 [1]Band structure for ferromagnet. Due to Stoner energy splitting, the majority and minority spins have different density of states at Fermi level. 6

1.2 [1]Spin-dependent resistance across a heterostructure. The structure consists of two FM layers seperated by NMs. Left figure shows the parallel state (R_p), while the right one represents the anti-parallel state (R_{ap}). $R_1(R_2)$ is the resistance when electrons transmit through ferromagnet of the same(opposite) spin polarization. The interfacial resistance has been merged into the overall layer resistance in this case. It is clear that $R_{ap} > R_p$. 7

1.3 Electrons interact with a ferromagnetic layer. 10

1.4 How spin torque acts in a magnetic multilayer heterostructure. FM1 and FM2 are the ferromagnetic layers. NM is the non-magnetic spacer in between two ferromagnetic layers. FM1 and FM2 represent the thicker fixed layer and the thinner free layer, respectively. 11

1.5 a. schematic diagram showing the direction of conservative torque (τ_H), the competition between spin transfer torque (τ_{st}) and damping torque (τ_d) during the magnetization precession; b. damped motion of magnetization at low current; c. steady state of oscillation at relatively higher current; d. switching process under high current. Figure from Ref.[2]. 12

2.1 [1]Photograph of the probe station. The optics, ring light and a monitor are hooked up to the CCD to project and enlarge the sample image. A 200 μm pitch microwave probe is positioned to touch down onto a typical sample's leads. 21

2.2 [1](a) the microwave probe positioner (b) the probe mounted on the positioner arm (c) the reversed positioner mounted through vacuum base attached to the stage bottom 24

2.3 [1](a) Microwave circuit for time domain measurements. The same instrument(Keitheley 2400) is utilized to supply DC current and measure the sample resistance across the inductor of the bias-T. The auto-oscillatory voltage signals generated by the spin valve device are observed by the real-time scope, after 40dB amplification. To improve bandwidth and communication rate, the scope is connected to the controlling computer via its ethernet port. (b) Real-time oscilloscope used in the setup with 12GHz bandwidth and maximal 40GS/s sampling rate. (c) Effective circuit diagram, including contact and probe resistances in the Rex, as well as the 50Ω scope impedance. The voltage oscillations $\Delta V(t)$ from the sample are evidently equal to $I\Delta R(t)$. . 27
2.4 [3]Circuit design diagram for low noise bridge measurement of resistance. . . 29
2.5 Resistance vs. field along easy axis of a $90\,\mathrm{nm}^2$ GMR device, measured by Wheatstone bridge setup. 31
2.6 Resistance of the same $90\,\mathrm{nm}^2$ GMR device at different fields along hard axis, from Wheatstone bridge measurement. 32
2.7 Schematic diagram of the sample's layer structure. 33
2.8 Schematic diagram describing how magnetization vectors of free and pinned layer response to external fields. Easy axis is defined as the axis along exchange bias; hard axis is perpendicular to exchange bias. 34
2.9 Fitting for the parameter χ in the angular dependence formula of GMR. The blue dots are the numerical data points at different applied fields along hard axis. The red curve is the best fitting result of the numerical data based on the angular dependent expression $\frac{R(\theta_m)-R_p}{R_{ap}-R_p} = \frac{1-\cos(\theta_m)}{2+\chi+\chi\cdot\cos(\theta_m)}$, which gives $\chi = 3.05$. 36
2.10 Blue circles represent maximal excitation power at several different applied fields along hard axis. The DC current applied onto the sample is swept from 0 up to 6 mA for each different field. The power is the integrated power of the quasi-uniform mode and is normalized by the maximum value. Red curve shows the corresponding frequency of each oscillating mode. 37
2.11 Power spectrum density (PSD) at different currents under $H = 600\,G$ along in-plane hard axis. Two oscillation modes are observed. The quasi-uniform mode is excited around 6.4 GHz. 38
2.12 Integrated power and linewidth of the quasi-uniform mode as a function of DC current applied to the sample under 600 G field along in-plane hard axis. 39
2.13 Inverse of the integrated power for the quasi-uniform mode in near-threshold range of currents. Same external field is applied. Dashed blue line corresponds to the approximate expression $(1/\bar{p} \propto (I_{th} - I)$ [4]) valid for small currents. Intersection of this line with x-axis gives the value of the critical current: ~ 0.8 mA.[4] 40
2.14 (a) Part of the time trace of the generated voltage signals at 2.7 mA, showing hoping between two modes; (b) zoom in oscillation signals of the quasi-uniform mode; (c) separate fourier transform spectra for the corresponding time intervals shown in (a). 41

2.15 (a) A schematic diagram describes the magnetization orbits across the sample plane at both zero and room temperature; (b) generated output voltages according to the oscillating orbits and magnetoresistance; (c) distributions of the extremes of the voltage signals, corresponding to the left and right crossings over the sample plane by the orbits in (a). 42
2.16 Raw data of volrage time trace. Some of the extrema near and far from the polarization vector $\vec{p}$ are indicated. 44
2.17 [1] Local extreme selection constraint. The $\Delta\varphi$ values are defined as φ minus the average angle of the trace $< \varphi >$. (a) Accepted extrema, which satisfy the condition of Eq. 2.7. (b) Rejected extrema based on the same critierion. 47
2.18 In-plane crossing angle distributions for quasi-uniform mode at currents from 1.9 mA to 3.1 mA. External field is applied along in-plane hard axis. X-axis represents the free layer's oscillation cone-angle with respect to the equilibrium position. 50
2.19 Corrected in-plane crossing angle distributions for quasi-uniform mode under currents from 1.9 mA to 3.1 mA. Inverse mapping from toy model of $\varphi(t)$. . . 52
2.20 A simulation example of the auto-oscillatory state for the free layer of our STO device at $T = 0$. 600 G field is applied perpendicular to the exchange bias. (a) FFT of x component of the oscillating magnetization. (b) Projection of the magnetization trajectories: z-component vs. x-component. (c) 3D plotting of the magnetization trajectories. 59
2.21 A stochastic simulation example of the auto-oscillatory state for the free layer of our STO device at $T > 0$. 600 G field is applied perpendicular to the exchange bias. (a) FFT of x component of the oscillating magnetization. (b) Projection of the magnetization trajectories: z-component vs. x-component. (c) 3D plotting of the magnetization trajectories. 60
2.22 Comparison of auto-oscillation frequency at the critical current for constant Gilbert damping and nonlinear damping ($q_1 = 0.3$) in the macrospin approximation. HeffAng is the effective field angle with respect to the opposite direction of the polarizer. The effective field is composed of external field and dipolar field from pinned layer. Three regimes of auto-oscillatory dynamics at the critical current are observed: small-amplitude, large-amplitude in-plane and large-amplitude out-of-plane oscillations. Nonlinear damping is found to extend the angular range of auto-oscillatory dynamics. 70
2.23 Effective energy profiles for various currents developed by the spin-torque dependent Fokker-Plank model. Constant damping is applied. 71
2.24 (a) Measured in-plane crossing angle distributions for currents far above the critical. (b) Experimental effective energy profiles calculated by the Fokker-Planck method, based on the measured crossing distributions shown in (a). . 72
2.25 (a) Effective energies predicted by the macrospin Fokker-Planck theory with constant damping applied. (b) Experimentally measured effective energy profiles. 72
2.26 (a) Effective energies predicted by the macrospin Fokker-Planck theory with implementation of non-linear damping ($q_1 = 4.35$). (b) Experimentally measured effective energy profiles. 73

3.1 Schematic circuit diagram of an MTJ microwave detector. Part A: K-connector; part B: ESD protection circuit; part C: bias tee; part D: magnet with tunable position; part E: MTJ device; part F: coplanar waveguide antenna for receiving microwave signal. 76
3.2 Cross-sectional view of a coplanar waveguide showing relevant dimensions. The yellow section stands for the metal part of the coplanar waveguide. The grey part represents the dielectric substrate in the middle, which is made of Duroid. 77
3.3 Microwave detector layout design 79
3.4 Dimensions of the assembled microwave detector 80
3.5 Resistance vs field curve for a typical type A(a), and type B(b) MTJ device, with nominal lateral dimensions 160 nm × 65 nm and 150 nm × 70 nm, respectively. Both fields are along in-plane hard axis. 82
3.6 Detector response to P = +15 dBm RF power: (a) Response of a type A detector. (b) Response of a type B detector. (c) Response of the best detector, a type B detector. 84
3.7 Response of a type B MTJ to a direct microwave input at -36 dBm power. . 86
3.8 Response of a type B detector under different applied field. Labels for each curve represent the distance between the MTJ and the magnet surface which is closer to the MTJ. 87
3.9 Response of a detector assembled with a pair of parallel MTJs (type B with $170 \times 70\,nm^2$ and $170 \times 60\,nm^2$ lateral dimensions) under different applied fields. The detector is placed under a horn antenna connected to a microwave generator, which outputs +15 dBm RF power. Labels for each curve represent the distance between the MTJ array and the magnet surface which is closer to the MTJ array. 88
3.10 Response of the same detector with a pair of parallel MTJs under the exact same condition after ESD protection test. Labels for each curve represent the distance between the MTJ array and the magnet surface which is closer to the MTJ array. 89
3.11 Response of the same detector with a pair of parallel MTJs under the exact same condition after vanish sealing and dropping test. Labels for each curve represent the distance between the MTJ array and the magnet surface which is closer to the MTJ array. 90

4.1 Schematic diagram of the amplitude-modulation ST-FMR setup. 97
4.2 Measured FMR signals (solid lines) and fitted curves (dashed lines) versus microwave drive frequency for three sets of detector arrays of different FL thicknesses: (a) $l = 3.0$ nm, (b) $l = 2.3$ nm, and (c) $l = 1.6$ nm. The insets show the determined frequency error Δf as a function of the drive frequency. 103

4.3 Frequency errors $\Delta f = |f_{\text{det}} - f_{\text{real}}|$ (color points) calculated from the determined frequency f_{det} [given by Eq. (4.4)] and real frequency f_{real} as a function of microwave drive frequency f_{real} for three studied cases of detector arrays: (a) orange squares, (b) violet circles, and (c) green triangles. The values of the detector's FMR linewidths for three detector arrays are indicated by color-coded solid (Γ_1) and dashed (Γ_2) horizontal lines, respectively. Black dash-dotted line is the theoretically calculated dependence Δf from Eq. (4.5) for the third detector array (c). 104

LIST OF TABLES

Page

4.1 The FL thicknesses l, applied external fields $B_{\mathrm{dc},1}$, $B_{\mathrm{dc},2}$ and delivered microwave power P_{rf} for the three detector arrays studied in the experiment (see Fig. 4.2) 99

4.2 The resonance frequencies $f_{\mathrm{res},1}$ and $f_{\mathrm{res},2}$ (in GHz units), FMR linewidths Γ_1 and Γ_2 (in GHz units), and resonance volt-watt sensitivities $\varepsilon_{\mathrm{res},1}$ and $\varepsilon_{\mathrm{res},2}$ (in mV/mW units) calculated from the fitted curves shown in Fig. 4.2 for the three detector arrays studied in the experiment 100

ACKNOWLEDGMENTS

I would like to first express my deepest gratitude to my advisor Ilya Krivorotov. Without his thoughtful guidance and patience to my research projects, it would not be possible for me to fulfill my current research achievement. Following his sharp wisdom and insights in the study of physics, I really learned a lot of knowledge of physics and gained much capability on debugging and problem solving skills. It is such a valuable experience for me to be a graduate student in his group and will be a great treasure for my whole life.

I also would like to offer my thanks to my other committee members, Professor Jing Xia and Zuzanna Siwy for their time on reviewing my thesis and giving me helpful suggestions.

Additionally, I would like to thank all my lab mates in Krivorotov's group: Zheng Duan, Graham Rowlands, Brian Youngblood, Yu-Jin Chen, Andrew Smith, Igor Barsukov, Jenru Chen, Alejandro Jara, Han Kyu Lee, Chris Safranski. They have been offered me great amount of help during my research life.

I thank my parents Ming Zhang and Lingfeng Tan for all of their understanding and support. Finally, I want to express my deepest appreciation to my husband Zheng Duan, who has been assisting and encouraging me all the time.

CURRICULUM VITAE

Jieyi Zhang

EDUCATION

Doctor of Philosophy in Physics **2017**
University of California, Irvine *Irvine, CA*

Master of Science in Physics **2017**
University of California, Irvine *Irvine, CA*

Bachelor of Science in Physics **2011**
Nankai University *Tianjin, China*

RESEARCH EXPERIENCE

Graduate Research Assistant **2011–2017**
University of California, Irvine *Irvine, California*

TEACHING EXPERIENCE

Teaching Assistant **2012**
University of California, Irvine *Irvine, California*

REFEREED JOURNAL PUBLICATIONS

Time Domain Mapping of Spin Torque Oscillator Dynamics **2017**
to be submitted to Physics Review B

Microwave radiation detector based on spin torque diode effect **2017**
to be submitted to Journal of Applied Physics

Determination of an external microwave signal frequency in array of two uncoupled spin-torque microwave detectors **2017**
to be submitted to Applied Physics Letters

Measurement of magnetic anisotropy and Gilbert damping of perpendicular STT-MRAM by spin torque ferromagnetic resonance **2017**
to be submitted to Applied Physics Letters

REFEREED CONFERENCE TALKS

Time Domain Mapping of Spin Torque Oscillator Dynamics **Nov 2014**
Magnetism and Magnetic Materials Conference

Time Domain Mapping of Spin Torque Oscillator Dynamics **Mar 2015**
American Physical Society March Meeting

Effect of nonlinear damping on spin torque driven auto oscillatory dynamics **Nov 2016**
Magnetism and Magnetic Materials Conference

ABSTRACT OF THE DISSERTATION

Nonlinear Spin-Torque Oscillator Dynamics and Spin-Torque Microwave Detectors

By

Jieyi Zhang

DOCTOR OF PHILOSOPHY in Physics

University of California, Irvine, 2017

Professor Ilya Krivorotov, Chair

This dissertation mainly describes the study of the spin-torque induced magnetic dynamics in patterned nanostructures from two aspects. The first study discusses the nonlinear damping effect in spin-torque oscillators(STOs). The direct time domain measurements on the stochastic STO dynamics will be described. We apply the time domain data to reconstruct statistical distributions of the STO free layer trajectories and analyze them in the framework of the effective Fokker-Planck energy approach. The prior work has been investigated for the dynamics near critical current[5]. This thesis will focus on the regime far above critical current and explain the nonlinear damping effect on the dynamics in this regime.

The second session presents detection of microwave signals by magnetic tunnel junctions(MTJs) based on the spin-torque diode effect. We show a wireless detection of microwave signals using a MTJ based detector. This MTJ detector is integrated with compact coplanar waveguide antennas and non-magnetic, microwave-transparent, reusable antenna holder. We compare the experimental results with MTJs of different magnetic layer structures. The tested structures can achieve comparable sensitivities to those of commercial semiconductor, diode-based microwave sensors. The detection frequencies can be tuned by a permanent magnet attached to the detector. In addition, we demonstrate a microwave frequency determination method by a pair of MTJs as microwave detectors. A resonance-type spin-torque microwave detec-

tor (STMD) can be used to determine the frequency of an input microwave signal. But the accuracy is limited by the STMD's ferromagnetic resonance linewidth. By applying a pair of uncoupled STMDs connected in parallel to a microwave signal source, we show that the accuracy of frequency measurement is improved significantly.

Chapter 1

Introduction and Background

The magnetic tunnel junction (MTJ)[6, 7, 8, 9, 10, 11, 12] based spin-torque microwave detector (STMD)[13] relies on three fundamental properties of MTJs: (i) the tunneling magnetoresistance (TMR)[14, 9, 15, 16] effect, (ii) the spin-transfer torque (STT)[17, 18] effect and (iii) the spin-torque diode effect[19, 20]. The STT effect in magnetic multilayers can transfer spin angular momentum between magnetic layers separated by a thin non-magnetic spacer when electrical current is applied. Magnetization dynamics can be excited in the free magnetic layer (FL) of an MTJ structure by external microwave signal due to the transfer of spin angular momentum. The magnetization dynamics lead to oscillating resistance of the MTJ structure due to TMR effect, which furthermore generates a dc rectified voltage when coupled with the ac microwave current injected to the system. This phenomenon is the so called spin-torque diode effect[19, 20]. Because of this, MTJ becomes a very promising candidate for making nano-scale ultra-sensitive microwave detectors[13].

Chapter 2 will report the design of wireless STMD based on MTJ devices and discuss about the experimental results on detecting radiation microwave signals. MTJ devices have already been employed as sensing elements for microwave detections[21, 22, 23, 24, 25, 26]. Wireless

detection of microwave signals by MTJs has not been demonstrated yet. Compared to microwave signals confined in a transmission line, a radiated microwave signal decays rapidly. Thus, a MTJ device with relatively high microwave detection sensitivity is desirable. In addition, a special design of compact antenna is presented for the purpose of coupling microwave signals to MTJ device and improving the impedance match. Furthermore, a detector assembled with a pair of parallel MTJs will be shown, which is capable of detecting microwave signals of different frequency ranges (around 1 GHz and 2.7 GHz).

Chapter 3 presents a signal frequency determination method based on a pair of uncoupled STMDs connected in parallel to a microwave signal source, which dramatically reduces the frequency measurement error. For a single STMD, the frequency detection error is quite large and comparable to ferromagnetic resonance (FMR) linewidth (typically exceeding 100MHz) [19, 20, 23, 27]. Meanwhile, the detector's frequency operation range is also limited by this FMR linewidth of the single MTJ. In this work, we demonstrate that by employing a pair of uncoupled MTJs in parallel, the frequency detection error can be 2 - 5 times lower and the frequency operation regime is expanded about 3 times. The theoretical investigation on this phenomenon done in collaboration with Prof. Prokopenko will also be present.

1.1 Magnetization Dynamics

In the absence of any non-conservative torques, the overall energy of a small magnetic structure is governed by four energy terms:

$$E = E_{demag} + E_{exch} + E_{anis} + E_{ext} \tag{1.1}$$

where the four terms represent the energy contributions from demagnetizing field (E_{demag}), exchange (E_{exch}), anisotropy (E_{anis}), and any external fields (E_{ext}). The demagnetizing and exchange energies govern the competition between achieving minimal micromagnetic curvature and minimizing the magnetic charge accumulated at the sample boundaries. The exchange length defines the length scale over which the magnetization remains constant:

$$l_{exch} = \sqrt{\frac{2A}{\mu_0 M_s^2}} \tag{1.2}$$

where A is the exchange constant, μ_0 is permeability in vacuum, and M_s is the saturation magnetization of the sample. If the sample size becomes comparable or larger than l_{exch}, the system will undergo a transition toward to a non-uniform magnetization state. The anisotropy energy has many potential contributions: crystalline anisotropy, perpendicular anisotropy at the interface between certain materials, and exchange-induced anisotropy[28, 29, 16].

Based on the assumption that our system is uniformly magnetized, E can be expressed only as a function of the magnetization $\vec{M}$. The magnetization dynamics are governed by the Landau-Lifshitz (LL) or Landau-Lifshitz-Gilbert (LLG) equation[17]:

$$\frac{\partial \vec{M}}{\partial t} = -\gamma_L \vec{M} \times \vec{H}_{eff} - \frac{\alpha \gamma_L}{M_s} \vec{M} \times (\vec{M} \times \vec{H}_{eff}) \qquad (LL) \tag{1.3}$$

$$\frac{\partial \vec{M}}{\partial t} = -\gamma_G \vec{M} \times \vec{H}_{eff} + \frac{\alpha}{M_s} \vec{M} \times \frac{\partial \vec{M}}{\partial t} \qquad (LLG) \tag{1.4}$$

where γ_L and γ_G are the gyromagnetic constans similar to the gyromagnetic ratio γ, α is the constant damping term, $\vec{H}_{eff}$ is the effective field which can be derived from Equation(1.1) :

$$\vec{H}_{eff} = -\frac{\partial E}{\partial \vec{M}} \tag{1.5}$$

Also, it can be easily proved that these two above equations are equivalent to each other by a modification of the gyromagnetic constants:

$$\gamma_G = (1 + \alpha^2)\gamma_L \tag{1.6}$$

Therefore, these two equations describe the identical magnetic dynamics. The first term represents the conservative torque by the effective field. The second term describes the damping torque caused by the energy lost during the magnetization precession. In the absence of any damping torque, the magnetization will process along conservative trajectories around the effective field $\vec{H}_{eff}$. When $\vec{H}_{eff}$ only consists of an external field $\vec{H}_{ext}$, the precession trajectory of $\vec{M}$ will be circular and with constant projection on $\vec{H}_{eff}$. This will occur only when the system has spherical symmetry. In real systems, any anisotropy can break the spherical symmetry, such as the shape anisotropy arising from the demagnetization field, which is given by the equation below.

$$\vec{H}_{demag} = -\underline{N} \cdot \vec{M} \tag{1.7}$$

where $\underline{N}$ is the demag tensor. In systems with high-symmetry, such as thin cylindrical disks or ellipsoids, $\underline{N}$ is diagonal, and therefore the shape anisotropy will lead to dynamics with a uniaxial or biaxial symmetry. When the damping torque is included, the magnetization vector will damp towards $\vec{H}_{eff}$ – the energy minimum direction of the system.

1.2 Giant and Tunneling Magnetoresistances

Discovery of magnetoresistance enables a direct electrical read-out of the magnetization orientation, which provides substantial opportunities of application. The origin of magnetoresistance is due to the imbalanced populations of spin-up (↑) and spin-down (↓) electrons caused by the Stoner energy splitting in some 3d transition metal ferromagnets. Thus, for electrons incident into such a ferromagnetic layer, both the transport and scattering for spin-up (↑) and spin-down (↓) electrons are spin-dependent. Interfacial scattering due to different band structures is also one major contribution to this spin-dependent scattering process. If the ferromagnet has a band structure like figure 1.1 typical for 3d transition metal ferromagnets, spin-up (↑) electrons will be the majority. In this case, the spin filter effect leads to a greater resistance for the incoming spin-down (↓) electrons, which points to the opposite direction of the majority spins (↑)[14, 30, 17].

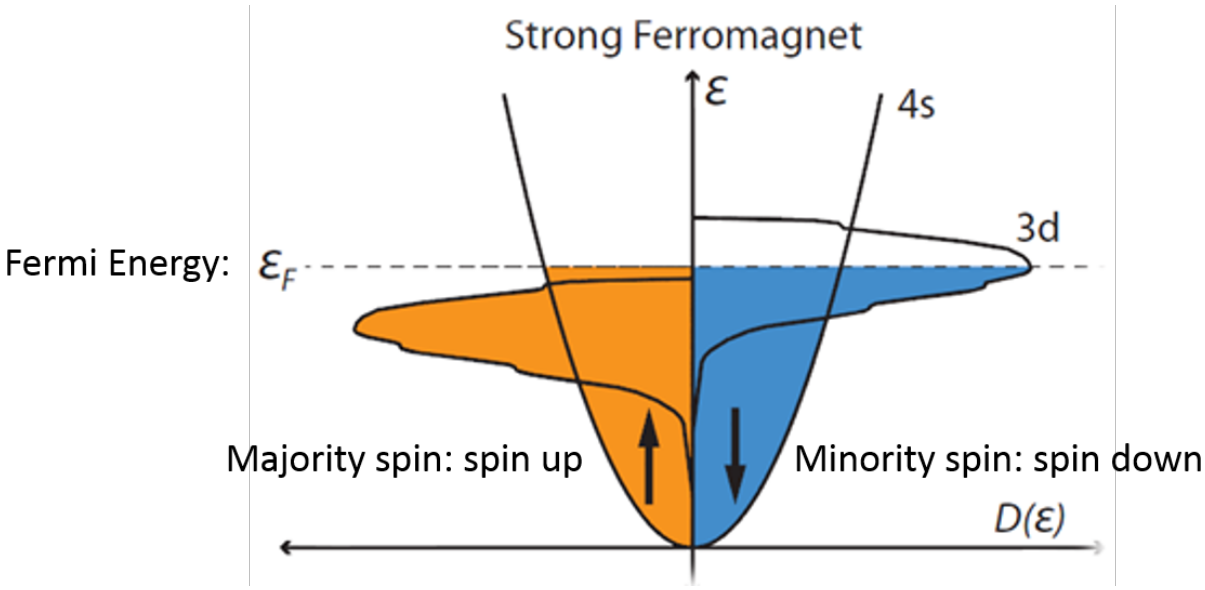

Figure 1.1: [1]Band structure for ferromagnet. Due to Stoner energy splitting, the majority and minority spins have different density of states at Fermi level.

Therefore, in a heterostructure composed of two ferromagnetic (FM) layers separated by non-magnetic (NM) spacers, the total resistance across the structure depends on the relative orientation of the magnetization vectors of the two FM layers[14, 6, 30]. Transport through this stack can be modeled as a network of resistors with parallel channels for spin-up and spin-down electrons shown in figure 1.2. When the magnetization of the two FM layers are aligned in parallel, the majority spin channel is the same in both ferromagnets and is therefore of lower resistance (R_p). Otherwise, when the FM layers are anti-parallel to each other, the system will be in a high resistance state (R_{ap}).

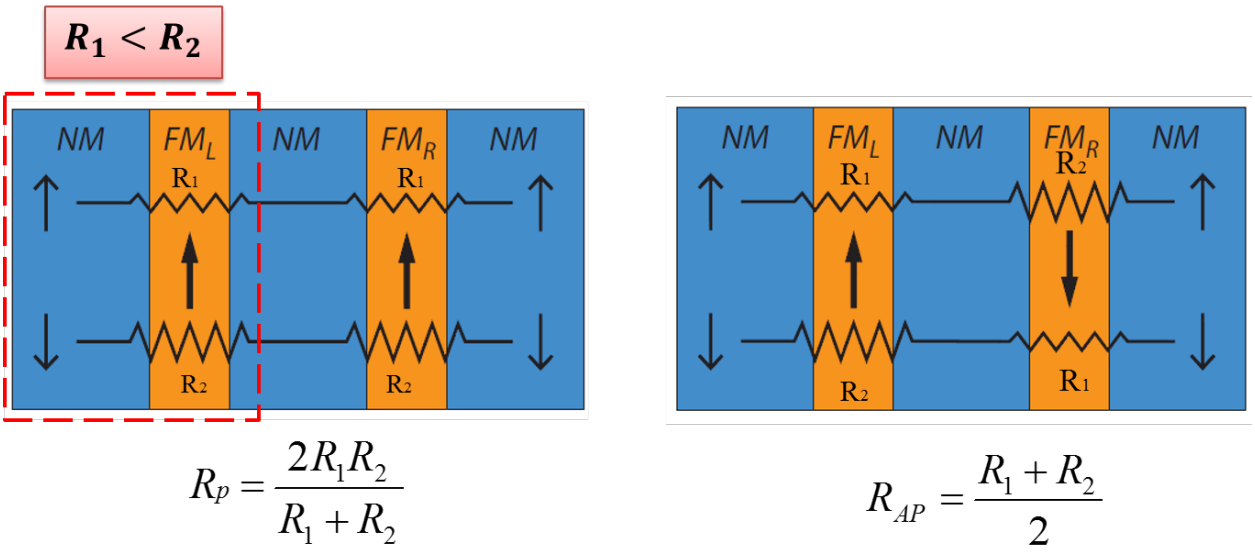

Figure 1.2: [1]Spin-dependent resistance across a heterostructure. The structure consists of two FM layers seperated by NMs. Left figure shows the parallel state (R_p), while the right one represents the anti-parallel state (R_{ap}). $R_1(R_2)$ is the resistance when electrons transmit through ferromagnet of the same(opposite) spin polarization. The interfacial resistance has been merged into the overall layer resistance in this case. It is clear that $R_{ap} > R_p$.

In case that the NM spacer is metallic, this effect is referred as the giant magnetoresistance (GMR). It was first discovered in the current in-plane geometry[31, 32]. The full scale GMR value is defined as below:

$$\Delta R_{GMR} \equiv \frac{R_{ap} - R_p}{R_p} \tag{1.8}$$

GMR is typically on the order of tenths of a percent of the total resistance of samples in many materials. When the two magnetizations are in between parallel and anti-parallel state, the resistance of the structure in the current-perpendicular-to-plane geometry with any intermediate angle between the two magnetizations can be expressed by the angular

dependence of GMR:

$$R = R_p + \Delta R_{GMR} \frac{\sin(\theta/2)^2}{1 + \chi \cos(\theta/2)^2} \tag{1.9}$$

where θ is the angle between the two magnetizations, and χ is a constant [33], which depends on layers' materials.

The motivation of looking for larger magnetoresistance drives the development of the heterostructure FM/NM/FM with a insulating barrier NM as the spacer. The tunneling magnetoresistance (TMR) was found in such magnetic tunnel junctions (MTJs). Originally this effect was observed across amorphous AlO_2 barriers, but later significantly larger TMR was found across MgO barrier with crystalline interface adjacent to FeCo electrodes[9, 15]. Compared to the previous metallic spin-valves, MTJs display much larger magnetoresistance and can achieve several hundred percent TMR at room temperature. The cause of the large MR lies in band structure of this FeCo/MgO/FeCo multilayer sandwich. There is only one major tunneling channel through the particular Δ_0 band in Fe electrodes. The tunneling channels through other bands are strongly suppressed, resulting in a half-metallic like property of the MTJ[7, 8]. The angular dependence of the conductance across an MTJ has a simple cosine dependence:

$$G = G_0(1 + P^2 \vec{m} \cdot \vec{p}) \tag{1.10}$$

where G_0 is the average conductance, P describes the spin polarization efficiency. Meanwhile, MTJs also have some drawbacks from the application perspective, especially the relatively

low break down voltage[34]. It is typically around 1.0 V. Due to the high resistance of MTJs, the critical current of the magnetization switching is always above or comparable to this break down level. Therefore, it does not satisfy all the ideal requirements for memory applications yet. However, MTJs are still believed to be one of the most promising candidates for the next generation of non-volatile memories . In addition, the high impedance of MTJs can cause difficulties in applications such as microwave communications, due to the poor impedance match to the surrounding electrical circuits.

1.3 Spin Transfer Torque

As one of the consequences of spin-dependent scattering first proposed by Slonczewski and Berger, electrons can transfer angular momentum to the ferromagnetic layer during the transmission process[17, 18]. When a charge current is injected to a ferromagnetic thin film, electrons will be either transmitted or reflected. Due to the band structure mismatch, electrons will undergo spin filtering process. As illustrated in figure 1.3, all the transmitted electrons are spin-up ($\uparrow$) polarized, while the spin-down ($\downarrow$) electrons will be reflected. Such transmission/reflection process generates a spin polarized current. Electrons that enter the ferromagnet are subject to a huge exchange field and will precess around the magnetization. As different electrons travel along different paths in the ferromagnet, each electron would process at different angles when they exit the ferromagnet. By summing over electrons from the entire Fermi surface, the transverse components of the spins cancel out. Similar behavior also applies to the reflected electrons. As a consequence, the total polarization of the spin polarized current leaving the ferromagnet, summed over relevant states of the Fermi surface, is approximately collinear with the magnetization of the ferromagnetic layer. Thus, the entire transverse component of the spin current is absorbed at the interface, giving rise to reciprocal spin transfer torque (STT) exerted on this ferromagnet, which can alter the

orientation of the magnetization[17].

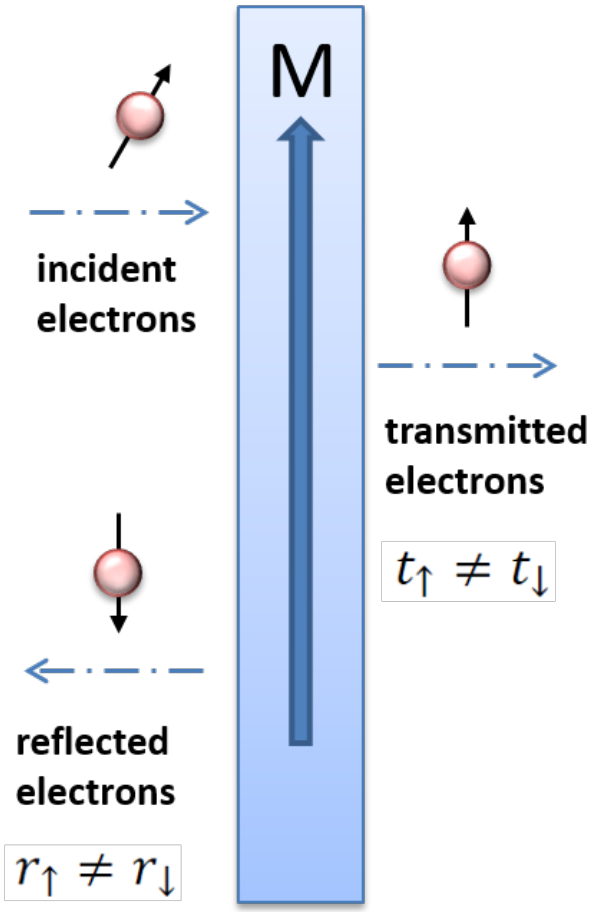

Figure 1.3: Electrons interact with a ferromagnetic layer.

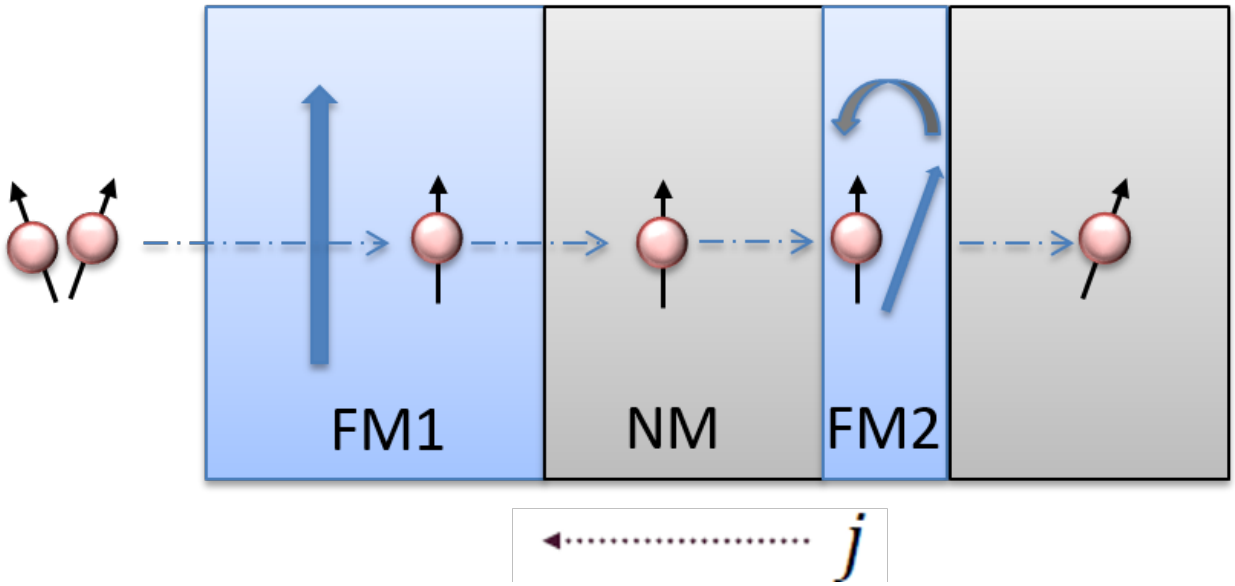

Figure 1.4: How spin torque acts in a magnetic multilayer heterostructure. FM1 and FM2 are the ferromagnetic layers. NM is the non-magnetic spacer in between two ferromagnetic layers. FM1 and FM2 represent the thicker fixed layer and the thinner free layer, respectively.

As shown in the schematic diagram 1.4, when electric current interacts with ferromagnetc multilayers, the current will first be spin polarized by FM1 layer. It then carries spin angular moment to the second ferromagnetic layer (FM2) and becomes polarized along the direction of magnetization in FM2. In return, a spin transfer torque (STT) is exerted onto the second layer (FM2). Since FM2 layer is designed to be thinner (free layer), the magnetization of FM2 will be pulled towards the polarization direction of the current, same with the direction of FM1 (fixed layer). This procedure describes how a current going through a GMR structure alters the free layer's magnetization by spin transfer torque (STT).

The expression for this spin transfer torque is shown below[2]:

$$\vec{\tau}_{st} = -\beta(I)g(\theta)\vec{m} \times (\vec{m} \times \vec{p}) \tag{1.11}$$

where $\beta(I)$ represents the spin torque strength as a function of current, $g(\theta)$ describes the angular dependence arising from material properties of the heterostructure, and $\vec{p}$ is the

normalized polarization vector. According to the equation above, the STT is an in-plane torque and perpendicular to the magnetic moment. Its amplitude is proportional to the current density[2].

It has also been demonstrated that an additional torque may arise from the spin accumulation, which has a similar expression to the torque given by from effective field:

$$\vec{\tau}_{fl} = -\beta'(I)g'(\theta)\vec{m} \times \vec{p} \tag{1.12}$$

where $\beta'(I)$ and $g'(\theta)$ have the same meanings as before. This field-like torque was observed to be negligibly small for metallic spin valves, however, its magnitude is generally much larger and plays a more important role in magnetic tunnel junctions[35, 36].

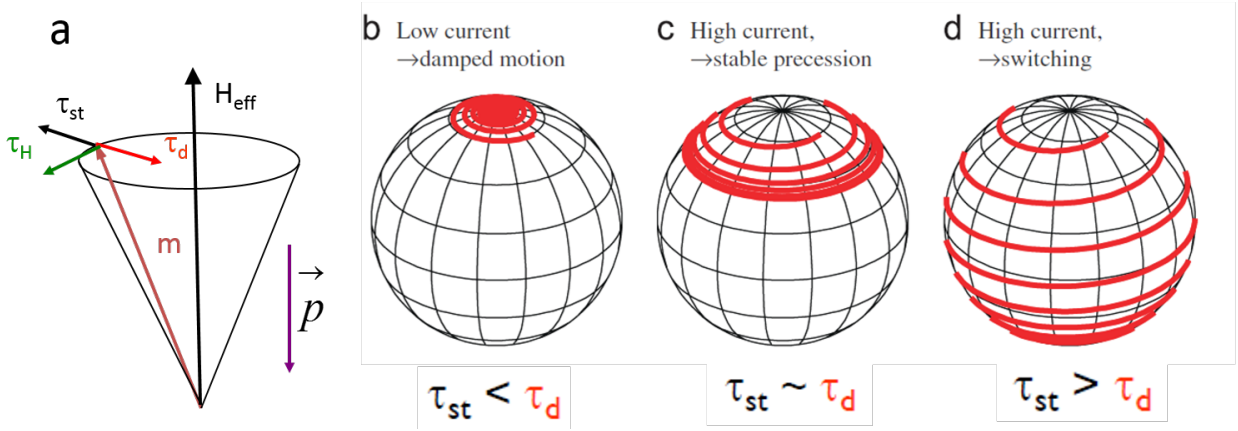

Figure 1.5: a. schematic diagram showing the direction of conservative torque (τ_H), the competition between spin transfer torque (τ_{st}) and damping torque (τ_d) during the magnetization precession; b. damped motion of magnetization at low current; c. steady state of oscillation at relatively higher current; d. switching process under high current. Figure from Ref.[2].

In reality, the dynamics of magnetization can be describe by the full version of LLG equation

including the spin transfer torque[2]:

$$\frac{\partial \vec{M}}{\partial t} = -\gamma_G \vec{M} \times \vec{H}_{eff} + \frac{\alpha}{M_s} \vec{M} \times \frac{\partial \vec{M}}{\partial t} - \beta(I) g(\theta) \vec{m} \times (\vec{m} \times \vec{p}) \tag{1.13}$$

where the first term stands for the conservative field torque (τ_H), the second term is the damping torque (τ_d), and the third part represents the spin transfer torque (τ_{st}). The directions of these three torques are shown in figure 1.5(a).

In absence of any spin torque or damping, if the free layer's magnetization is perturbed away from $\vec{H}_{eff}$, it will begin processing around $\vec{H}_{eff}$. However, due to the existence of the damping torque in real samples, $\vec{M}$ will always damp back towards the lowest energy configuration along $\vec{H}_{eff}$[2].

When a charge current is applied, the direction of the spin transfer torque (STT) is either towards or opposite to the damping torque, depending on the current polarization. When the STT is parallel to the damping torque, the effective damping is enhanced by the applied current, therefore the magnetization will be pulled back more rapidly toward $\vec{H}_{eff}$. On the other hand, when the STT is anti-parallel to the damping torque, in case of a small applied current, the STT can only reduce the effective damping slightly, leading to a longer damping process till the magnetization reaches its equilibrium direction (shown in Fig. 1.5(b)). When the magnitude of the charge current reaches sufficiently high such that the spin transfer torque is comparable to or even larger than the damping torque, the magnetization will oscillate away from $\vec{H}_{eff}$ following any perturbations and two possible dynamic states will occur depending on the strength of the spin transfer torque. The first scenario is when the STT is comparable to the damping torque, a steady precession state occurs (Fig. 1.5(c)). This phenomenon is called spin torque oscillation and was first found in experiments by

Kiselev et al. in metallic spin valves [37], and subsequently by Rippard et al. in point contacts thin film composed of NiFe/Cu/CoFe [38]. The other possible state is the magnetization reversal, which occurs when the STT is much larger than the damping torque as illustrated in Fig. 1.5(d)[2]. The first experimental discovery of magnetization reversal was performed by Katine et al. in a Co/Cu/Co multilayer structure[39]. Later on, a large variety of magnetic nano-devices have been developed as one of the most promising candidates for the next generation of random access memories.

1.4 Spin Torque Oscillator

Spin torque oscillators(STOs) are one of the outcomes of the spin torque induced dynamics in nano-scale spin valves and magnetic tunnel junctions. When the damping torque from effective magnetic field and the spin torque from DC polarized current contribute equal but opposite work along the oscillation trajectories, the magnetic moment will reach a steady oscillation state – processing around the equilibrium magnetization direction along a constant energy trajectory. This auto-oscillatory state has frequency determined by the eigenmode frequency of the excited state[37]. These magnetic oscillations generate AC voltage signals due to the oscillating magnetoresistance and the DC electric current, which can then be measured by a spectrum analyzer or real-time oscilloscope.

Since STOs can generate microwave power at a frequency tunable by the DC current or external magnetic field, these nano-devices exhibit application potentials in many fields, such as nano-scale tunable microwave sources, ultra-fast spectrum analyzer, and magnetic field sensors in hard drives[40]. Because of the nano-scale dimensions, thermal fluctuations can strongly disturb the oscillation trajectories at room temperature and thus ruin the coherence of oscillations[41, 42]. Moreover, strong nonlinearity can be induced at larger oscillation amplitude, mixing amplitude noise in the magnetization dynamics into phase

noise, which further reduces the coherence and broadens the oscillation line-width. Therefore, quantitative understanding of these stochastic dynamics and nonliear effect becomes crucial for the development of devices with desired properties such as narrow linewidth and high frequency excitation. In chapter 2, we demonstrate a reconstruction method of a metallic spin valve's oscillation trajectories by collecting time domain data with a real-time scope. Further investigation on the large angle oscillation dynamics will be described by applying the Fokker-Planck effective energy approach to analyze the nonlinear damping effect at large oscillating regime.

1.5 Spin Torque Ferromagnetic Resonance

So far, we have discussed how the LLG equation describes the magnetic processional dynamics in a ferromagnet. As mentioned before, in absence of any damping-like torque, the frequency of the magnetization precession is (for a spherical sample) given by the Larmor frequency $\omega = \gamma H_{eff}$ in the linear regime. Once the linear dynamics has been resonantly excited, this is what is referred to as ferromagnetic resonance (FMR) frequency. FMR can be detected via a number of approaches. We will discuss two of them in details in the following. The FMR spectra can provide deeper insight of the physics properties of the magnetic materials, such as the saturation magnetization, damping constant, magnetic anisotropy, sensitivity, spin-torque vector, etc..

1.5.1 Conventional Ferromagnetic Resonance

Most of the prior ferromagnetic resonance measurements were made by determining the microwave absorption of the ferromagnetic samples. This is so called the conventional ferromagnetic resonance[43]. Assuming there is a ferromagnetic ellipsoid placed in the Cartesian

coordinate and a DC magnetic field applied along the longest axis ($\hat{z}$). The ferromagnetic ellipsoid is also exposed to microwave radiation, which produces RF magnetic field perpendicular to the DC field (along the $\hat{x}$ axis). As discussed in the previous chapter, the RF magnetic field drives the magnetization to process around $\vec{H}_{eff}$. When the microwave frequency coincides with the eigenfrequency of the device, a large absorption of the microwave power would appear. The applied magnetic field can be expressed as follows:

$$\vec{H}_{app} = \hat{z}H_{DC} + \hat{x}H_{RF}e^{i\omega t} \tag{1.14}$$

Taking into account the demagnetization field in $\vec{H}_{eff}$, the x, y, z components of the effective magnetic field are:

$$H'_x = H_x - N_x M_x \tag{1.15}$$

$$H'_y = -N_y M_y \tag{1.16}$$

$$H'_z = H_z - N_z M_z \tag{1.17}$$

Ignoring any damping-like torques (they would not influence the resonance frequency significantly) and taking $H_x = \hat{x} \cdot \vec{H}_{app}$,$H_z = \hat{z} \cdot \vec{H}_{app}$, three orthogonal components of the LLG equation become:

$$\partial_t M_x = \gamma[H_z + (N_y - N_z)M_z]M_y \tag{1.18}$$

$$\partial_t M_y = \gamma[M_z H_x - (N_x - N_z) M_x M_z - M_x H_z] \tag{1.19}$$

$$\partial_t M_z \approx 0 \tag{1.20}$$

The resonant frequency can be obtained theoretically by solving the equations above:

$$\omega_0 = \gamma \sqrt{[H_z + (N_y - N_z) M_z][H_z + (N_x - N_z) M_z]} \tag{1.21}$$

In experiment, the microwave absorption can be measured by placing a ferromagnetic sample in a microwave cavity under the drive of RF magnetic field. The microwave absorption is generally measured as a function of the applied external field, and the magnetic resonance can be determined from the peaks of the absorption curves. This technique has been adopted for the study of various magnetic properties, such as the saturation magnetization, the exchange constant, Gilbert damping, etc[44].

1.5.2 Spin Torque assisted Ferromagnetic Resonance

Spin transfer torque assisted ferromagnetic resonance(ST-FMR) [19, 20] is another technique recently developed for the study of magnetic properties. It is similar to the conventional FMR, except that the magnetization driving source is mainly the spin-torque instead of RF magnetic field produced by the microwave radiation. Briefly, when a microwave current is injected to a MTJ or spin valve, as discussed in the prior chapter, a microwave spin

polarized current is induced and drives the free layer's magnetization precession, leading to an oscillating sample resistance caused by the magnetoresistance effect. A DC rectified voltage is therefore generated by averaging the product of this oscillating resistance and the ac current. The dependence of such a rectified voltage signal on the microwave drive frequency can be measured as the ST-FMR spectrum. Under a certain circumstance, the frequency of the external microwave drive coincides with the intrinsic frequency of the system, and a voltage peak appears in the measured ST-FMR spectrum. Detailed derivation is shown below:

$$R(t) = R_0 + \Delta R(t) = R_0 + Re(\sum_n \Delta R_{nf} e^{in2\pi ft}) \tag{1.22}$$

Then by Ohm's law

$$V_{dc} =< I_{rf}\cos(2\pi ft)R(t) >= \frac{1}{2} I_{rf}|\Delta R_f|\cos(\delta_f) \tag{1.23}$$

where f is the driving frequency, δ_f is the phase difference between the ac resistance and driven current[19, 20].

In terms of DC bias (I,V), V_{dc} can be approximated as [45]

$$\frac{1}{4}\frac{\partial^2 V}{\partial I^2} I_{rf}^2 + \frac{1}{2}\frac{\partial^2 V}{\partial\theta\partial I}\frac{\hbar\gamma_0 \sin\theta}{4eM_s\mathcal{V}\sigma} \times I_{rf}^2(\varepsilon_\parallel S(\omega) - \varepsilon_\perp \Omega_\perp A(\omega)) \tag{1.24}$$

where

$$\varepsilon_{\parallel,\perp} = \left[\frac{2e/\hbar}{\sin(\theta)}\right]\frac{d\tau_{\parallel,\perp}}{dI} \tag{1.25}$$

are dimensionless differential torques, $S(\omega)$ and $A(\omega)$ are symmetric and anti-symmetric

lorentzians given by

$$S(\omega) = \frac{1}{1 + \frac{(\omega - \omega_m)^2}{\sigma^2}} \tag{1.26}$$

$$A(\omega) = \frac{(\omega - \omega_m)}{\sigma} S(\omega) \tag{1.27}$$

Here, ω_m is the resonance precession frequency of the magnetization, $\Omega_\perp = \gamma(4\pi M_{eff} + H)/\omega_m$ in case of an elliptical thin film. σ is the line-width of the ST-FMR spectrum given by [45]

$$\sigma = \frac{\alpha\omega_m}{2}(\Omega_\perp + \Omega_\perp^{-1}) - \cot(\theta)\frac{\gamma\tau_\parallel(V,\theta)}{2M_s\mathcal{V}} \tag{1.28}$$

This equation reveals that the damping constant α can be obtained from ST-FMR measurement of the spectra line-width at $V = 0$:

$$\alpha_{eff} = \frac{2\sigma}{\omega_m(\Omega_\perp + \Omega_\perp^{-1})} \tag{1.29}$$

It is clear from equation (1.24) that by fitting the symmetric and antisymmetric components of an ST-FMR spectrum, one can obtain both the contributions from the in-plane and out-of-plane spin torque experimentally[45].

In ST-FMR measurement, usually we sweep the microwave frequency at a constant field when obtaining the spectra. Compared to the conventional absorptive FMR technique, one advantage of ST-FMR is that much smaller samples can be properly measured. The ST-FMR measurement on MTJs provides the foundation for the development of microwave detectors to be discussed in chapter 3 and chapter 4.

Chapter 2

Nonlinear Spin Torque Oscillator Dynamics

2.1 Experimental Methods

2.1.1 Microwave Probe Stations

In order to study the physics of magnetic dynamics ferromagnetic heterostructures, reliable electrical connections to these magnetic devices must be established first. Moreover, microwave signals in the characteristic frequency range of magnetic dynamics (a few to tens of gigahertz) must be able to be delivered and captured in the nanostructures. In practice such connections are established using either a coplanar waveguide wire-bonded directly to the sample leads, or using specially designed microwave probes to touch down on the lead patterns of the sample. We use the latter method for the room temperature measurements described in this chapter, which has several advantages. The wire-bonding approach enables extremely stable electrical connections between the sample and the surrounding measure-

ment circuits. However, it is prohibitively slow for testing on numerous samples, since each wire bonding preparation to a sample is a time consuming process. In comparison, manually positioned microwave probes doesn't require any preparation and thus is much more efficient. Such a measurement setup is shown in Fig. 2.1.

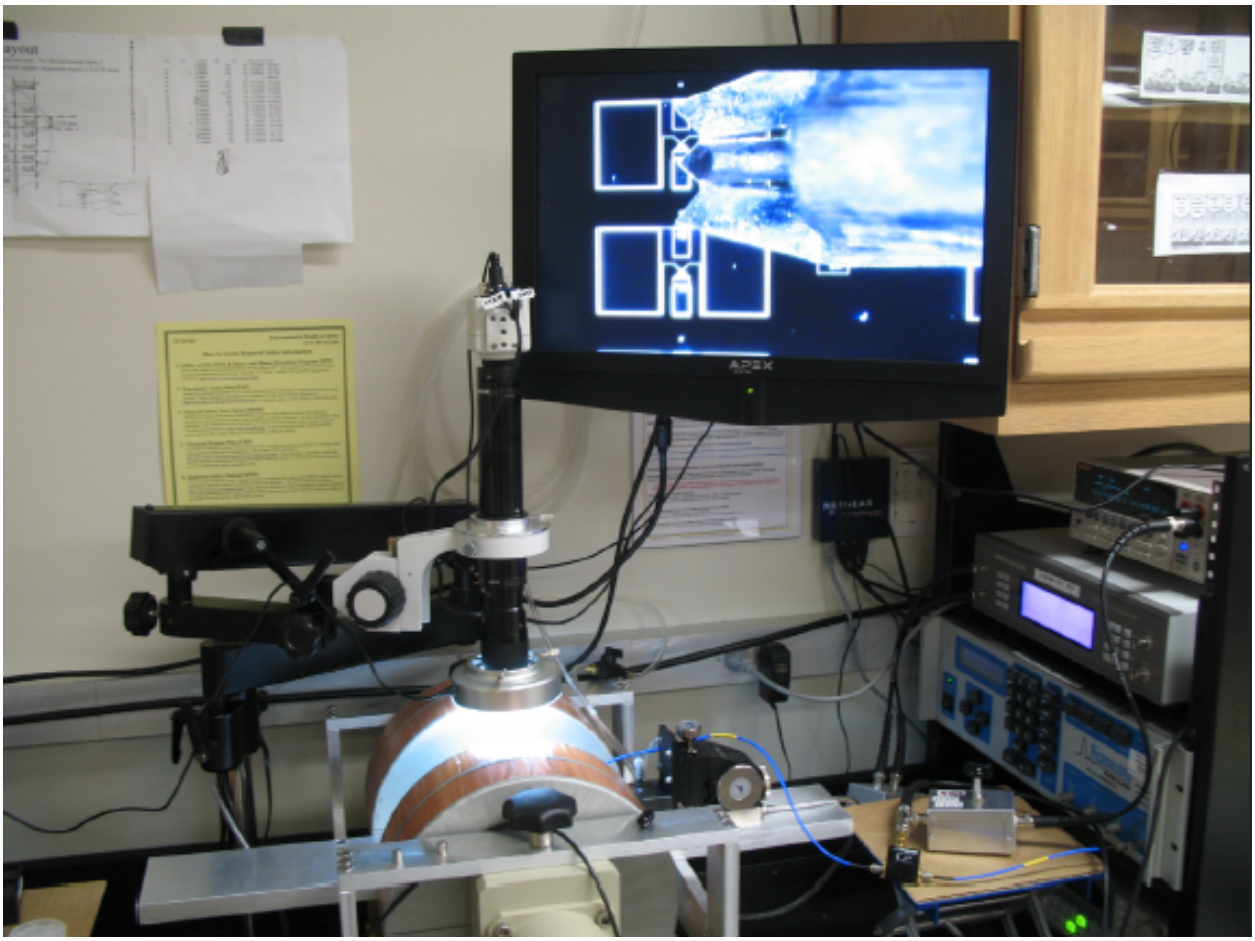

Figure 2.1: [1]Photograph of the probe station. The optics, ring light and a monitor are hooked up to the CCD to project and enlarge the sample image. A 200 μm pitch microwave probe is positioned to touch down onto a typical sample's leads.

The essential components for the construction of the probe station are as follows:

GMW Electromagnet: Model 5403, designed with adjustable semi-tapered poles. The magnet is capable of producing a 3 kOe in-plane magnetic field at maximum. Power is supplied to the coils by two Kepco BOP 20-20M power supplies. A hall bar is mounted on one of the

pole pieces for field calibration. It enables the accurate deliver and read of the field value at the center of the gap regardless of any pole hysteresis.

Cascade Micropositioners: Model RPP210, assembled with a probe arm of specially designed length. Both the arm and the positioner are made with non-magnetic material. Vacuum mounting is attached to its bottom.

GGB Microwave Probes: Model GSG-200/250, specially manufactured with no magnetic material. This model is designed to have a 200 or 250 μm pitch, ground-signal-ground configuration with minimal losses up to 40 GHz.

Diaphragm Pump: Supplying a low vacuum to hold the positioners and vacuum chuck.

Navitar Optics: With larger focus range to avoid placing any of the optics in between the electromagnet coils. The model assembled with a 12X body with 1X adaptor, 0.5 Lens adapter, and Sentech 1/3" CCD Analog Camera with S-Video output to a monitor nearby. An LED ring light is applied to illuminate the sample stage.

Most of the system's components do not need maintenance very frequently, except for the probes. The microwave probes are very fragile and mechanically strained with every contact procedure. Therefore, extreme protection is required to maintain reasonable lifetimes of the probes.

2.1.1.1 Probe Usage and Maintenance

The standard operation procedures for the safe use of the probe are introduced in the following. Nevertheless, the probe tips will be degraded anyway with frequent use and will require replacement or repair eventually.

1. When installing (or removing) the probes onto the positioners, orient the positioners as

in Fig. 2.2(b) such that the probe arm points to an empty space. Make sure that the probe is always secured with at least one mounting screw before entirely releasing it.

2. To align the planarity of the probe, a contact substrate (with gold surface) is needed for testing. Touch down the probe tips to the contact substrate and travel back and forth for a little distance several times. Then observe whether the ground leaves of the probe make equivalent marks on the substrate. If not, adjust the planarity control of the positioner accordingly, until the marks are roughly about the equivalent size.

3. The probe must be retracted far away from the sample surface before moving the entire positioner. Then one can move the positioner by releasing the vacuum mount and lifting up the positioner with one hand holding the probe arm. One should not slide the positioner along the stage, as the sliding motion is less controllable and will cause damage to the vacuum seal. Clean the vacuum seal repeatedly after a certain period of time (use a cotton swab with alcohol free cleanser).

4. The microwave cable connected to the probe must be secured by the cable clamp on the positioner. The cable can be surrounded with a piece of foam for mechanical protection. To tighten the cable properly, one need to make sure that smooth moving of the free end of the cable does not lead to any substantial change in the probe orientation.

5. When trying to make contact to the sample, slowly move the z-axis control until a minimal amount of over-travel is observed. Always keep the least amount of over-travel which still allows for stable electrical connection. If excessive amount of over-travel is required for good contact, the probe might need to be cleaned or repair.

6. Prevent the probe from touching any unclean or non-uniform surface, since it may cause damage to the probe.

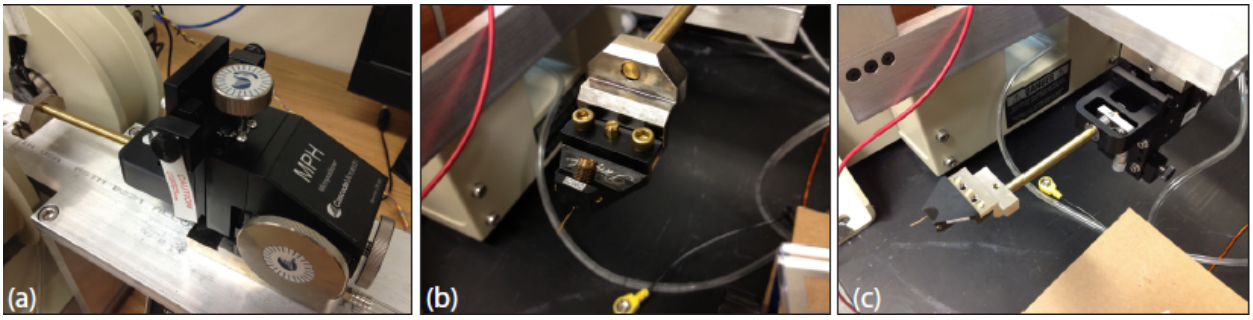

Figure 2.2: [1](a) the microwave probe positioner (b) the probe mounted on the positioner arm (c) the reversed positioner mounted through vacuum base attached to the stage bottom

Despite following the standard procedures above, the microwave probes will still become dirty, or damaged after a while. If the probe is worn and cannot provide stable contacts, we need to send it back to the factory for refurbishment.

If noisy contacts happens due to dirt on the probe leads, proper cleaning of the probe can solve this problem. Firstly, one needs to float the probe leads over free space either as shown in Fig. 2.2(a) or upsidedown as in Fig. 2.2, and take the optics to focus on the probe tips. Loosen the fibers of a cotton swab and soak them in isopropyl alcohol, then gently clean the leads of the probe. With further care, one may reverse the positioner and attach it to the bottom of the stage, then observe the status of the bottom of the probe leads, where most dusts tend to accumulate.

2.1.2 Time Domain Measurement of STO Dynamics

Typically magnetic dynamics in STOs are observed in the frequency domain, while some features of the dynamics cannot be captured in the frequency domain. Time domain analysis offers a direct look at the dynamics and therefore can provide wealthier information [46, 47]. When a STO device is excited by a DC electrical current, periodical voltage signals will be generated due to the oscillating magneto-resistance and DC current. By recording the

oscillating voltage signals, the ensemble of magnetization trajectories within the free layer can be reconstructed. The required assumption is that the oscillating orbits are symmetric with respect to the sample plane. Thus, those points where the magnetization crosses the sample plane are corresponding to the extrema of the time-dependent resistance oscillations (R(t)) [5].

Since our study focuses on the STO dynamics regime far above critical current, we apply this measurement for STOs based on metallic spin valves, which are able to survive at much higher current range than MTJs. The sample we used are 90 nm × 90 nm circular GMR nanopillar with the fixed layer pinned by an anti-ferromagnet(IrMn). The multilayer structure is composed of Substrate/IrMn(6)/Co(0.5)/$CoFe_{50}$(1)/$CoFeGe_{27}$(3)/ $CoFe_{50}$(0.5)/Cu(4)/$CoFe_{50}$(0.5)/$CoFeGe_{27}$(4)/$CoFe_{50}$(0.5)/Cap, with in-plane magnetization in both free and fixed layer. The exchange bias field given by the anti-ferromagnet layer is not very large such that the magnetization of pinned layer can keep its orientation fixed all the time. Detailed charaterization of the sample's properties is introduced in the next section.

The circuit setup for this time domain measurement is shown in figure 2.3. In the circuit, we separately measure both average and time-dependent resistance of the sample:

$$R = R_{ex} + < R > + \Delta R(t) \tag{2.1}$$

where R_{ex} represents all external resistance contributions(e.g. contact resistance, probe impedance) to the sample itself. $< R >$ is the average resistance measured by a Keithley 2400 sourcemeter. $\Delta R(t)$ stands for the oscillatory component which is recorded by a oscilloscope with the highest possible bandwidth and sampling rate. We use an Agilent DSO81204B

oscilloscope possessing a 12 GHz bandwidth and maximum sampling rate of 40 GS/s (giga-sample-points per second), which is depicted in Fig.2.3(b).

In order to observe decent signal to noise ratio(SNR) at the scope, we utilize a certain amplifier in the measurement circuit. The amplifier must be chosen based on its working bandwidth, noise figure, and the gain value necessary for analysis of the particular sample. In our experiment, we applied a Miteq model AFS5-00100800-14-1DP-5 with nearly constant 40dB gain across the operational range of 0.1-8.0 GHz. The noise floor shown at the oscilloscope with this type of amplifier is around 5 mV.

The amount of space for storing the real-time traces is not insubstantial: the maximum trace length of 2^{19} 8 bit data points yields 0.5 MB of data, and multiple traces are usually required for obtaining high statistics. The GPIB bus does not possess sufficient bandwidth to enable rapid and continuous acquisition of these traces, hence alternative faster transfer protocol is necessary. In the case of the older instrument the 100 Mb/s ethernet port may be used for VISA communications, while on even more modern instruments USB 2.0/3.0 is also an available option. Either of these communication ports increases the maximum rate of data acquisition by nearly an order of magnitude. In addition, the controlling computer needs to free up enough space on hard drive for the storage of data traces.

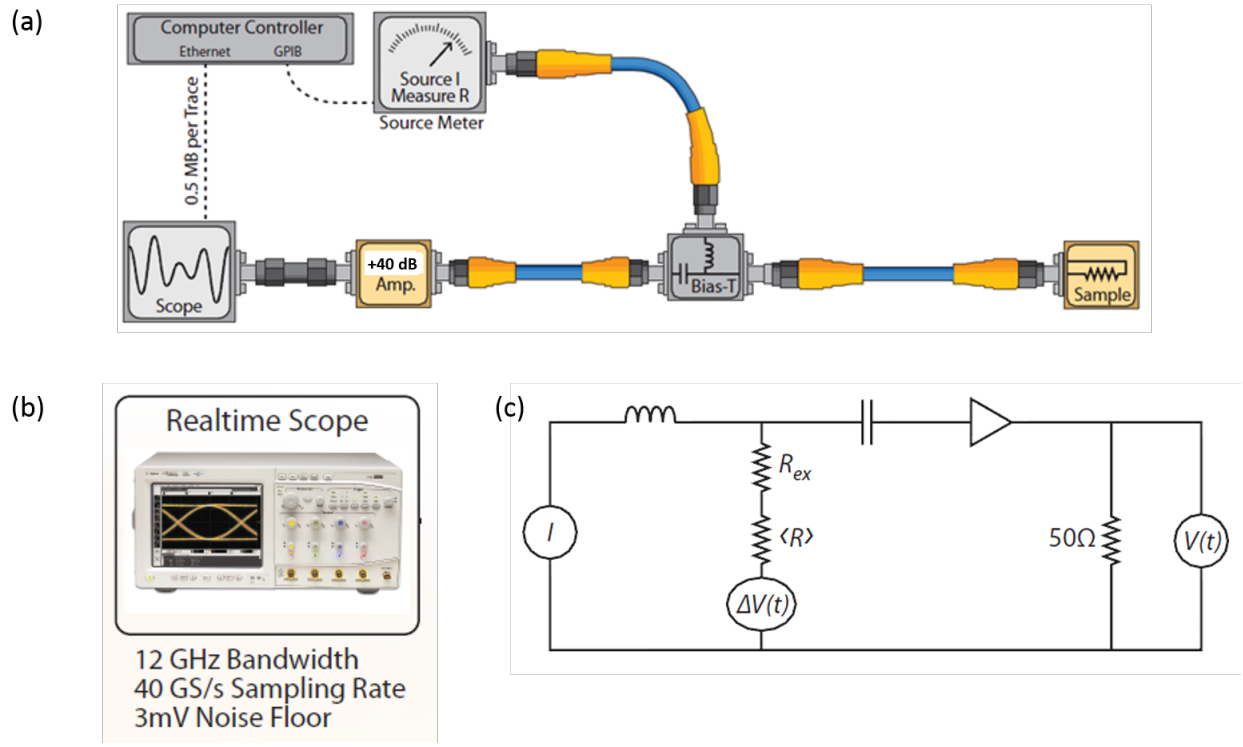

Figure 2.3: [1](a) Microwave circuit for time domain measurements. The same instrument(Keitheley 2400) is utilized to supply DC current and measure the sample resistance across the inductor of the bias-T. The auto-oscillatory voltage signals generated by the spin valve device are observed by the real-time scope, after 40dB amplification. To improve bandwidth and communication rate, the scope is connected to the controlling computer via its ethernet port. (b) Real-time oscilloscope used in the setup with 12GHz bandwidth and maximal 40GS/s sampling rate. (c) Effective circuit diagram, including contact and probe resistances in the Rex, as well as the 50Ω scope impedance. The voltage oscillations $\Delta V(t)$ from the sample are evidently equal to $I\Delta R(t)$.

According to the voltage signals measured at the scope, the oscillating component of the sample's resistance can be expressed as following (after taking into account of the amplification value):

$$\Delta R(t) = \frac{V(t)}{I} \frac{50\Omega + R_{ex} + < R >}{50\Omega} \tag{2.2}$$

where the 50Ω resistance corresponds to the scope impedance shown in Fig.2.3(c).

Since the magnetization procession orbits are symmetric about the sample plane, those points at which $\vec{M}$ cross the equator correspond to extrema of the $\Delta R(t)$ traces. Also, the metallic spin valve resistance depends only on the projection of $\vec{M}$ onto the polarization vector $\vec{P}$. Therefore, the in-plane crossing angles between $\vec{M}_f$ and $\vec{M}_p$ can be mapped from the $\Delta R(t)$ extrema, if the angular dependence of GMR is known. This angular dependence is described as the formula below:

$$\frac{\Delta R(\varphi(t)) + < R > - R_p}{R_{ap} - R_p} \equiv \frac{\delta R(\varphi(t))}{\Delta R} = \frac{1 - \cos(\varphi(t))}{2 + \chi + \chi \cos(\varphi(t))} \tag{2.3}$$

where $\varphi(t)$ is the in-plane crossing angle between free layer's magnetization and the polarizer, R_p and R_{ap} are the resistance of parallel(P) and antiparallel(AP) state accordingly. χ is a constant asymmetry parameter of the giant magnetoresistance[33], which only depends on the material of the ferromagnetic stack.

To fit the parameter χ, accurate measurement of P and AP resistance is required as well as the curve of δR vs. φ composed of numerical points. The study of this angular dependence relationship is fully described in the next section.

2.2 Angular Dependence of GMR

In order to obtain the fitting parameter χ as accurate as possible, one needs to lower the noise in the resistance measurement. Compared to the measurement using Keitheley sourcemeter, employing a Wheatstone bridge can provide better measurement accuracy. The circuit design of this Wheatstone bridge measurement is shown in Fig.2.4.

The main circuit is composed of two parallel paths. Both paths contain two arm resistors(R), while the left path has one adjustable resistor box (R_{change}) and the right path includes the sample(R_s) in between. All the arm resistors are adjustable from 10 K to 1 M and are normally set to the same values. The arm resistance is required to be nearly two orders of magnitude larger than the sample resistance. Both of the two parallel paths are connected to the lock-in amplifier, which is the AC voltage output from the amplifier's internal oscillator(V_{osc}). Since the sample resistance is a lot smaller thatn the arm resistances, the current going through each path can be considered as a constant value($I = \frac{V_{osc}}{2R_{arm}}$). In the two parallel paths, one end of the adjustable resistor box and the sample is grounded; at the other end, the lock-in amplifier is applied to measure the voltage difference between the two paths. The voltage difference($V = I(R_s - R_{change})$) reflects the difference between R_s and R_{change}. The sign of the difference indicates which resisntace is larger. By adjusting the value of the resistor box and checking the reading output of the lock-in amplifier, one can record the value of the resistor box when it is closest to the sample resistance. Resistance vs. direct current can also be captured using this bridge by connecting a current source to the voltage leads of the sample.

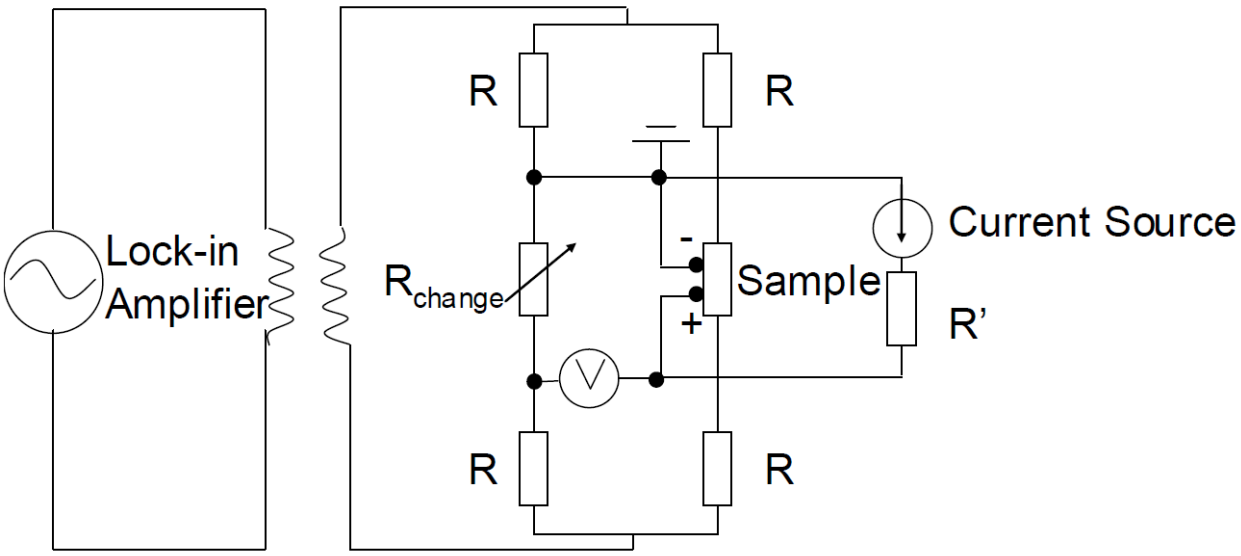

Figure 2.4: [3]Circuit design diagram for low noise bridge measurement of resistance.

The step-by-step instruction for running this experiment is as following:

1. connect the "sample current" and "sample voltage" ports on the bridge to the device.

2. On the lock-in amplifier, either use remote control or manual setting, set the oscillator output to a small AC value (depending on the range of sample resistance and the selection of arm resistors). Then set the oscillator frequency to a reasonable value (normally a prime number within 800-1200 Hz), as well as the lock-in reference to internal. Connect the "oscillation-out" port of the lock-in amplifier to the corresponding port on the bridge.

3. Connect the "lock-in input" port on the bridge to the connection box separating signals from one single port to two separate ports. Then connect the two ports correspondingly to the lock-in input A and B. Set the lock-in measurement mode to "A-B".

4. If necessary, connect a current source directly to the "current source" port on the bridge.

5. Use the LabView VI of the dV/dI vs. I at different H or dV/dI vs. H at different I. Fix the applied field or direct current, sweep the current or field accordingly, then record the sample resistance.

Fig.2.5 shows the resistance vs. field curves along easy axis for a 90 nm $\times$ 90 nm circular GMR heterostructure measured by this Wheatstone bridge method. Fig.2.6 represents the R vs. H dependence when field is applied along hard axis. The positive direction of easy axis is pointing along the exchange bias, while the hard axis is the perpendicular to the exchange bias direction. Such a bridge measurement lowers down the error of resistance to about 1 $m\Omega$, which improves the fitting accuracy of the asymmetry parameter χ.

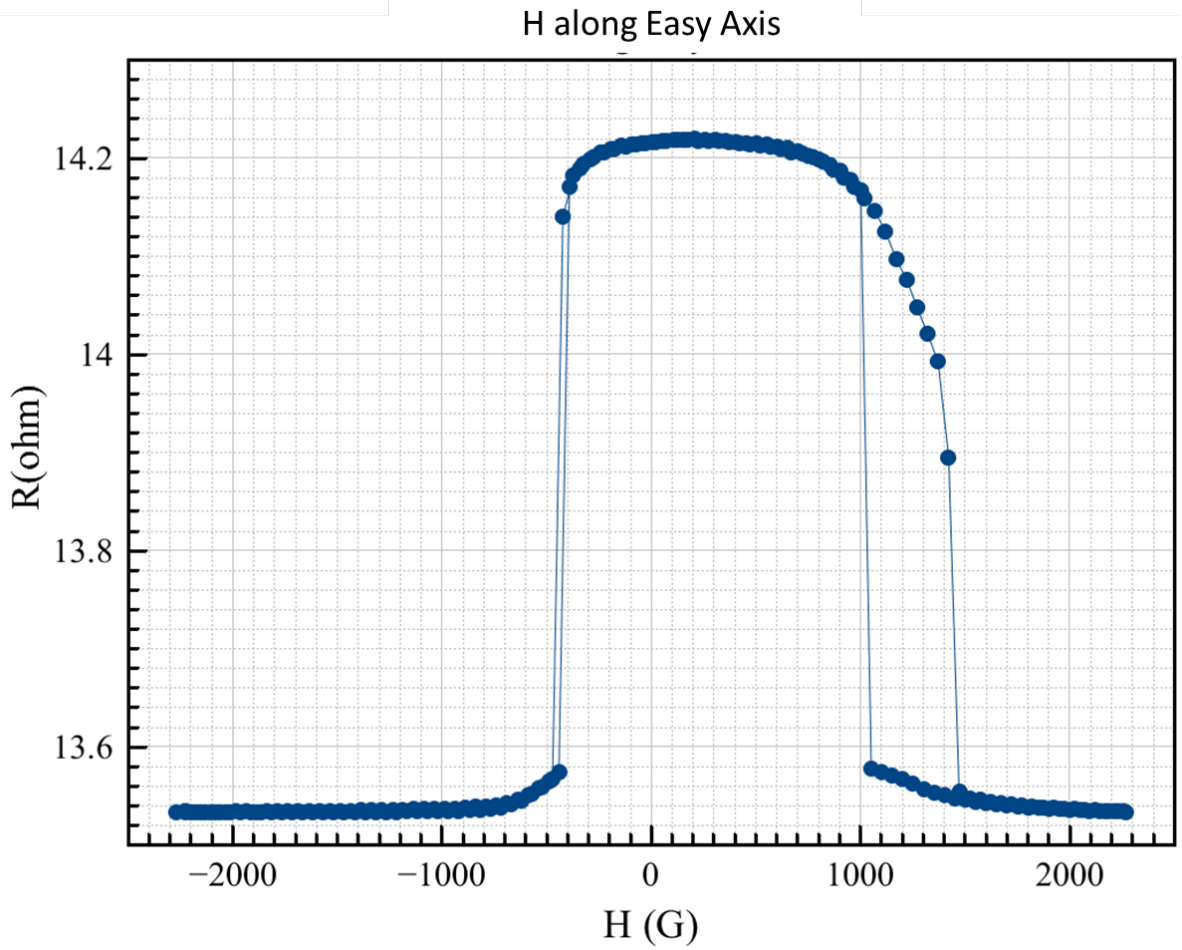

Figure 2.5: Resistance vs. field along easy axis of a 90 nm^2 GMR device, measured by Wheatstone bridge setup.

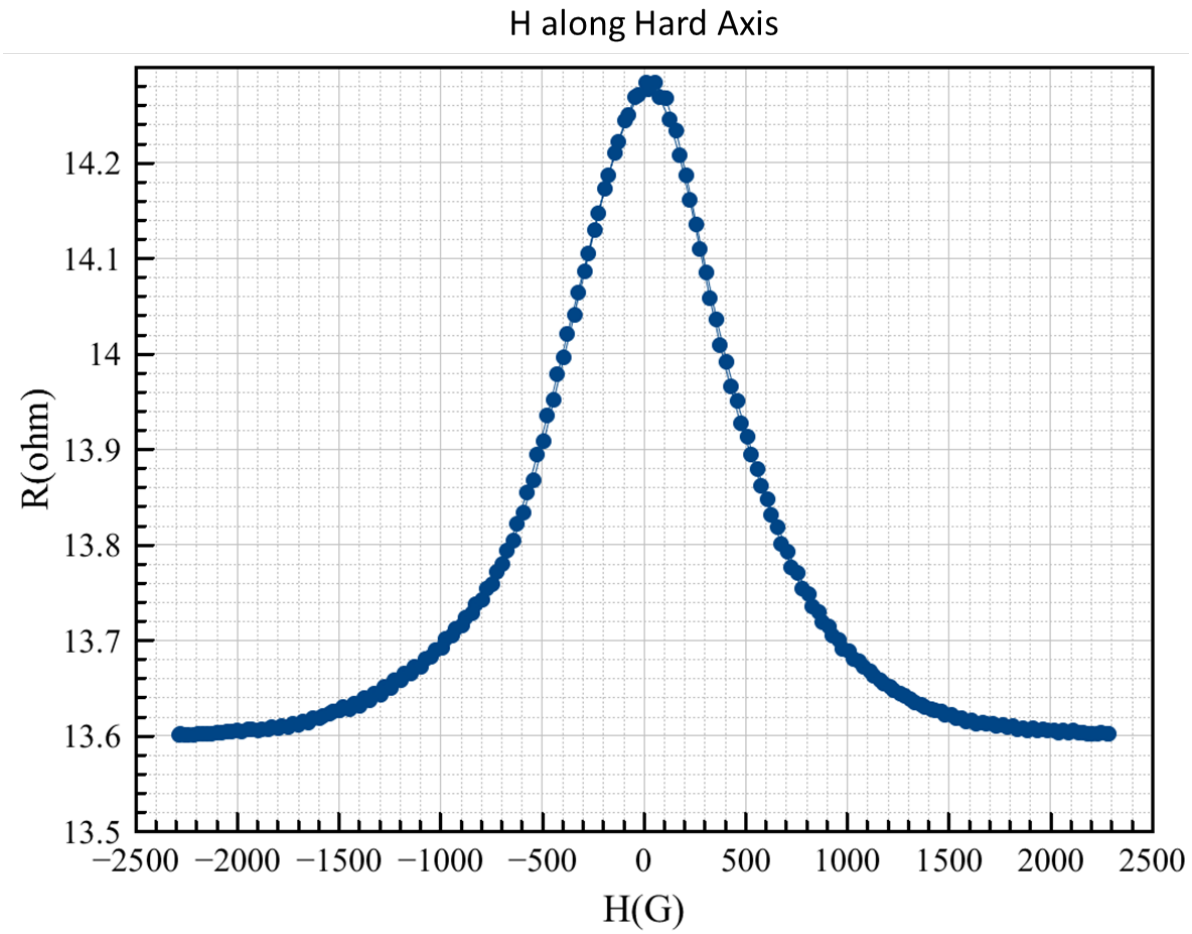

Figure 2.6: Resistance of the same 90 nm^2 GMR device at different fields along hard axis, from Wheatstone bridge measurement.

To fit χ, one needs to know the relationship between R and φ. So far, the R vs. H along hard axis is measurable. Thus, if the H vs. φ can be achieved by solving a macrospin energy minimum model of the system, the R vs. φ should be mapped directly. According to the schematic diagram of the sample's structure shown in Fig.2.7, the total magnetic energy of the entire structure can be expressed in the formula below:

$$E = -\vec{H} \cdot (\vec{m}_f + \vec{m}_p) - \vec{H}_{ex} \cdot \vec{m}_p - J \cdot (-\vec{m}_p \cdot \vec{m}_f) \tag{2.4}$$

where $\vec{m}_f$ and $\vec{m}_p$ describe the magnetization vector of the free and pinned layer correspondingly, $\vec{H}_{ex}$ is the exchange bias field acting on the pinned layer, J represents the constant parameter within the dipolar interaction between $\vec{m}_f$ and $\vec{m}_p$. The total energy contains contributions from three fields seen in Eq.2.4: the applied field, exchange coupling field, and dipolar field respectively.

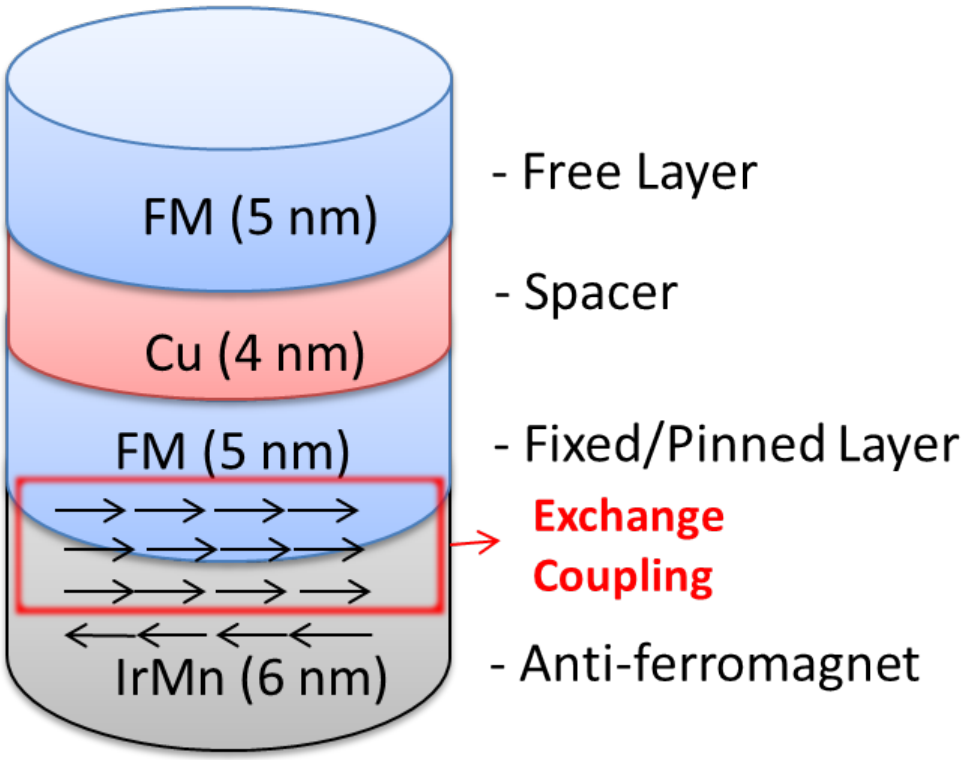

Figure 2.7: Schematic diagram of the sample's layer structure.

Two assumptions are associate with this model: 1. the exchange bias is fixed, which can be considered as an external field acting on the pinned layer; 2. $\vec{m}_p$ does change with $\vec{H}$, not always along exchange bias.

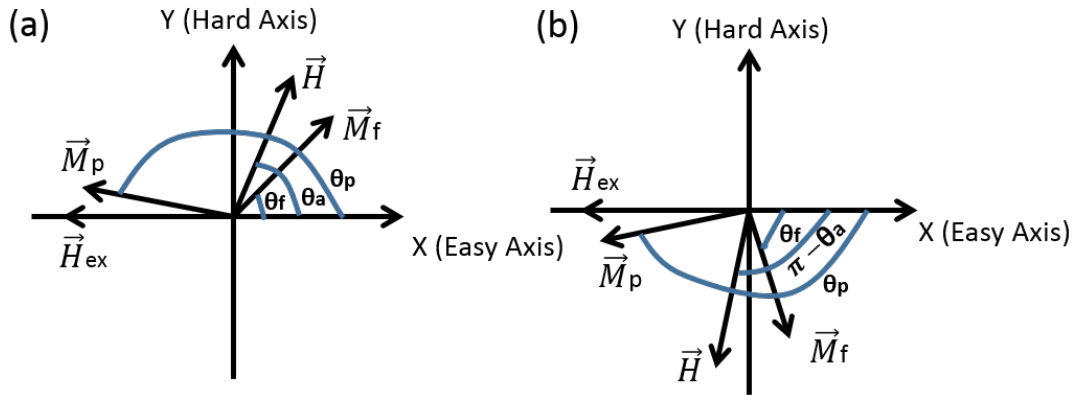

Figure 2.8: Schematic diagram describing how magnetization vectors of free and pinned layer response to external fields. Easy axis is defined as the axis along exchange bias; hard axis is perpendicular to exchange bias.

As illustrated in Fig.2.8, Eq.2.4 can be derived in terms of scalar products as following:

$$\begin{aligned} E = &- H \cdot M_f \cdot V_f \cdot \cos(\theta_a - \theta_f) - H \cdot M_p \cdot V_p \cdot \cos(\theta_p - \theta_a) \\ &- H_{ex} \cdot M_p \cdot V_p \cdot \cos(\pi - \theta_p) + J \cdot M_p \cdot V_p \cdot M_f \cdot V_f \cdot \cos(\theta_p - \theta_f) \quad (H_y > 0) \end{aligned} \tag{2.5}$$

$$\begin{aligned} E = &- H \cdot M_f \cdot V_f \cdot \cos(\pi - \theta_a - \theta_f) - H \cdot M_p \cdot V_p \cdot \cos(\theta_p + \theta_a - \pi) \\ &- H_{ex} \cdot M_p \cdot V_p \cdot \cos(\pi - \theta_p) + J \cdot M_p \cdot V_p \cdot M_f \cdot V_f \cdot \cos(\theta_p - \theta_f) \quad (H_y < 0) \end{aligned} \tag{2.6}$$

M_p and M_f are on behalf of the magnitude of magnetization density. V_f and V_p are the corresponding volumes for free and pinned layer. θ_f, θ_p and θ_a represent the angle of $\vec{H}$, $\vec{M}_f$ and $\vec{M}_f$ respectively in the coordinate shown in Fig.2.8. Several coefficients in the above equations can be obtained through the R vs. H data along easy axis (Fig.2.5): $J \cdot M_p \cdot V_p$ is equal to 430.4 G, as it represents the dipolar field from $\vec{M}_p$, which is provided by the shift of the switching field (P to AP) from zero; $J \cdot M_f \cdot V_f$ is 366.9 G as $J \cdot M_f \cdot V_f = J \cdot M_p \cdot V_p \cdot \frac{M_f}{M_p} \cdot \frac{t_f}{t_p}$

($M_p = 1208.5e^3(A/m)$, $M_f = 1030.1e^3(A/m)$, $t_p = t_f = 5(nm)$, according to sample's structure); $\vec{H}_{ex}$ equals to 858.1 G, calculated by subtracting $J \cdot M_f \cdot V_f$ from the AP to P switching field.

In the case of $\theta_a = 90°$ ($\vec{H}$ along hard axis), by minimizing the energy model (Eq. 2.5 and Eq. 2.6) with respect to θ_f and θ_p, one can obtain the numerical relationship between the magnitude of H and $\cos(\theta_m)$ ($\cos(\theta_m) = \cos(\theta_p) \cdot \cos(\theta_f) + \sin(\theta_p) \cdot \sin(\theta_f)$). θ_m stands for the angle between free and pinned layer, which is equivalent to $\theta_p - \theta_f$. Combining the data of $\cos(\theta_m)$ vs. H from energy minimal model and R vs. H from experiment, both of which are under hard axis applied field, numerical dependence between $\cos(\theta_m)$ and R can be easily achieved. Therefore, a $\cos(\theta_m)$ vs. R curve is ready for fitting the asymmetry constant χ in Eq. 2.3. The fitting procedure is depicted in Fig. 2.9, giving $\chi = 3.05$.

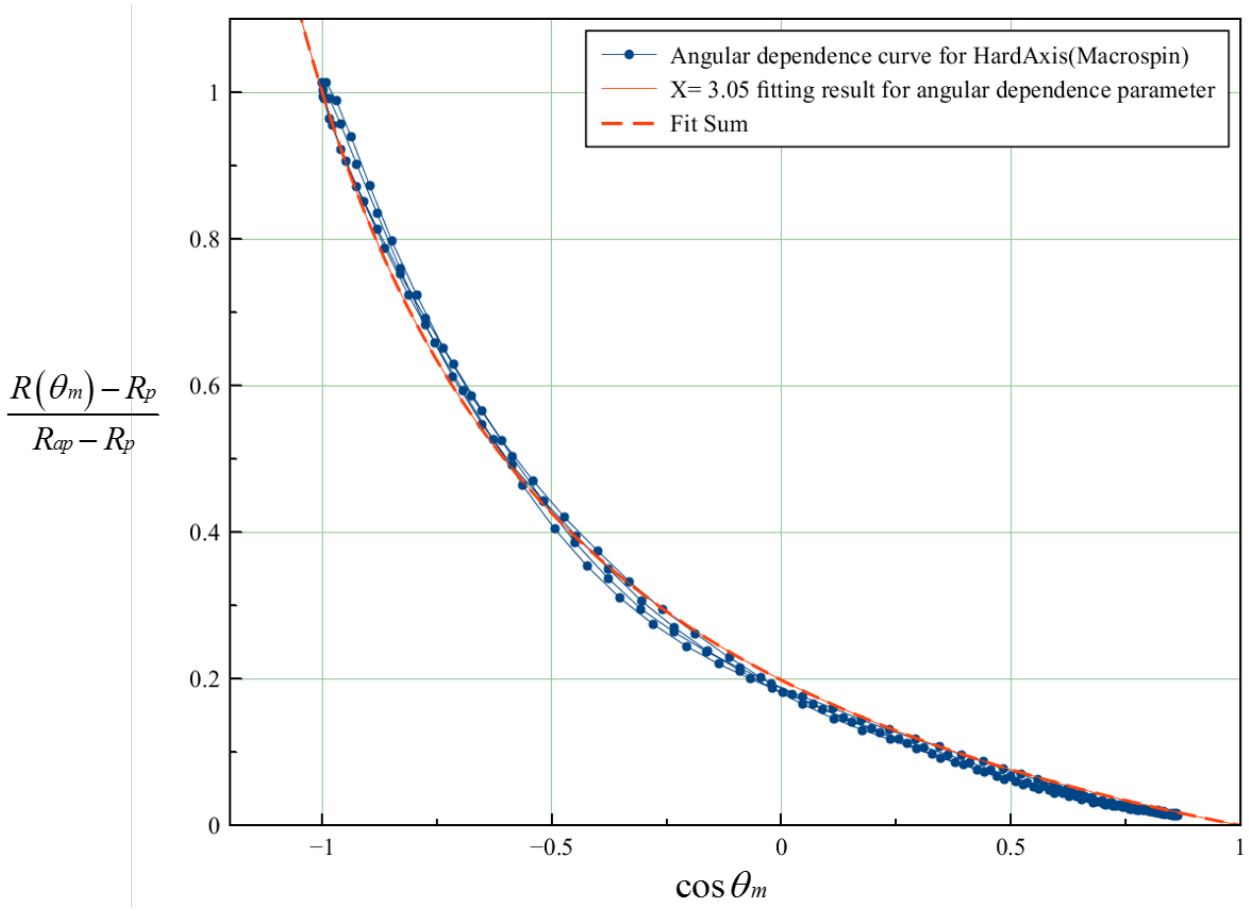

Figure 2.9: Fitting for the parameter χ in the angular dependence formula of GMR. The blue dots are the numerical data points at different applied fields along hard axis. The red curve is the best fitting result of the numerical data based on the angular dependent expression $\frac{R(\theta_m)-R_p}{R_{ap}-R_p} = \frac{1-\cos(\theta_m)}{2+\chi+\chi\cdot\cos(\theta_m)}$, which gives $\chi = 3.05$.

2.3 Characterization in Frequency Domain

Before the analysis of data in the time domain measurement, one should firstly understand the auto-oscillatory modes excited in the GMR device measured in frequency domain. Fig. 2.10 shows the maximal integrated power of the quasi-uniform mode excited at different fields along hard axis. One can easily tell that maximum power occurs at 600 G. Thus, we then focus on collecting data under 600 G applied field along in-plane hard axis.

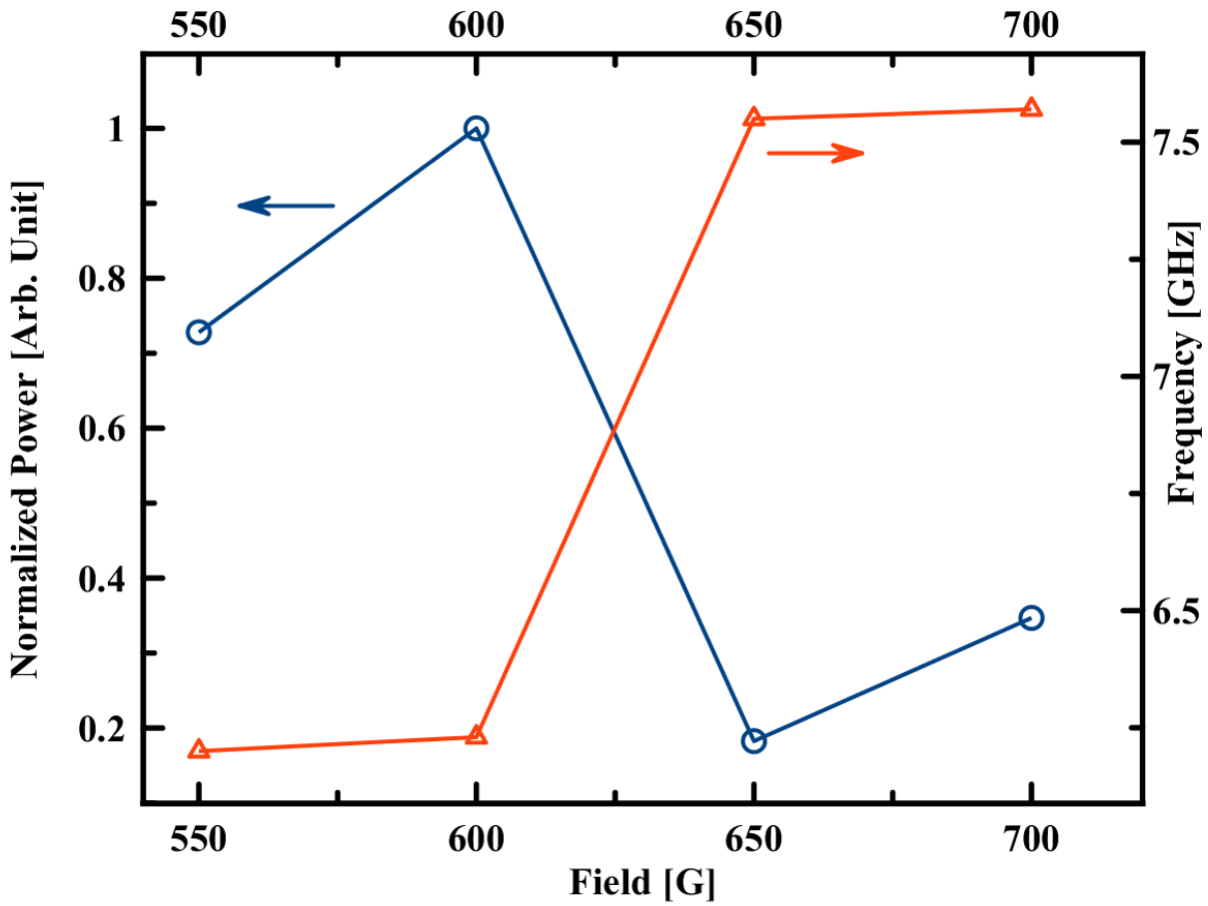

Figure 2.10: Blue circles represent maximal excitation power at several different applied fields along hard axis. The DC current applied onto the sample is swept from 0 up to 6 mA for each different field. The power is the integrated power of the quasi-uniform mode and is normalized by the maximum value. Red curve shows the corresponding frequency of each oscillating mode.

As illustrated in Fig. 2.11, two spin wave modes are observed in this STO device. We will concentrate on the dynamics of quasi-uniform mode, which possesses higher power and lower precession frequency.

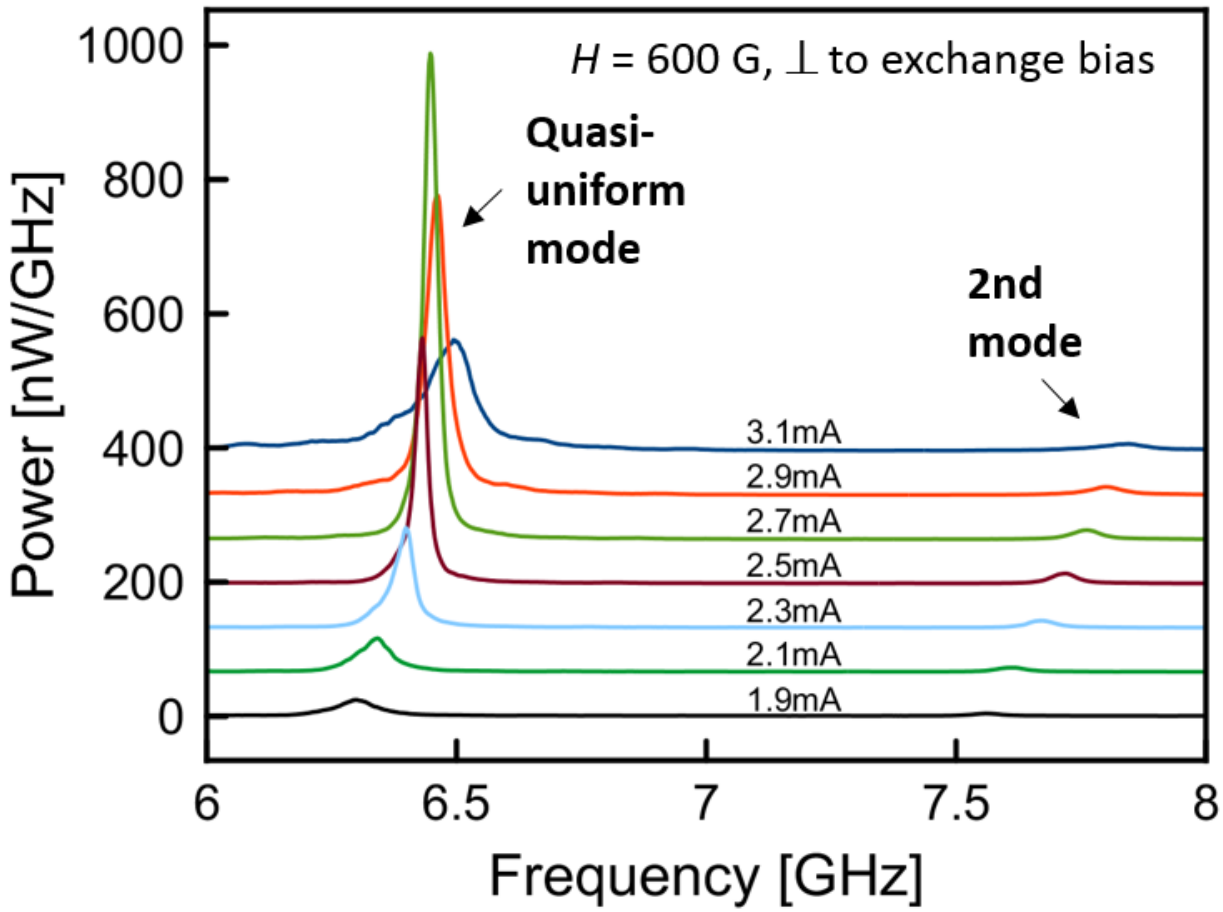

Figure 2.11: Power spectrum density (PSD) at different currents under $H = 600\,G$ along in-plane hard axis. Two oscillation modes are observed. The quasi-uniform mode is excited around 6.4 GHz.

Fig. 2.12 provides the dependence of linewidth and integrated power of quasi-uniform mode on DC current bias. The power reaches maximum at 2.8 mA, while the linewidth minimum is also observed near this maximum output power. Fig 2.13 shows the inverse of output power in Fig. 2.12 as a function of DC current. The crossing point with x-axis by the blue fitting line estimates the critical current for the onset of self-oscillation to be around 0.8 mA [4]. Meanwhile, in Fig. 2.12, an abrupt peak of linewidth also occurs around 0.8 mA, which agrees with the theoretical prediction by Prof. Slavin in Ref.[4].

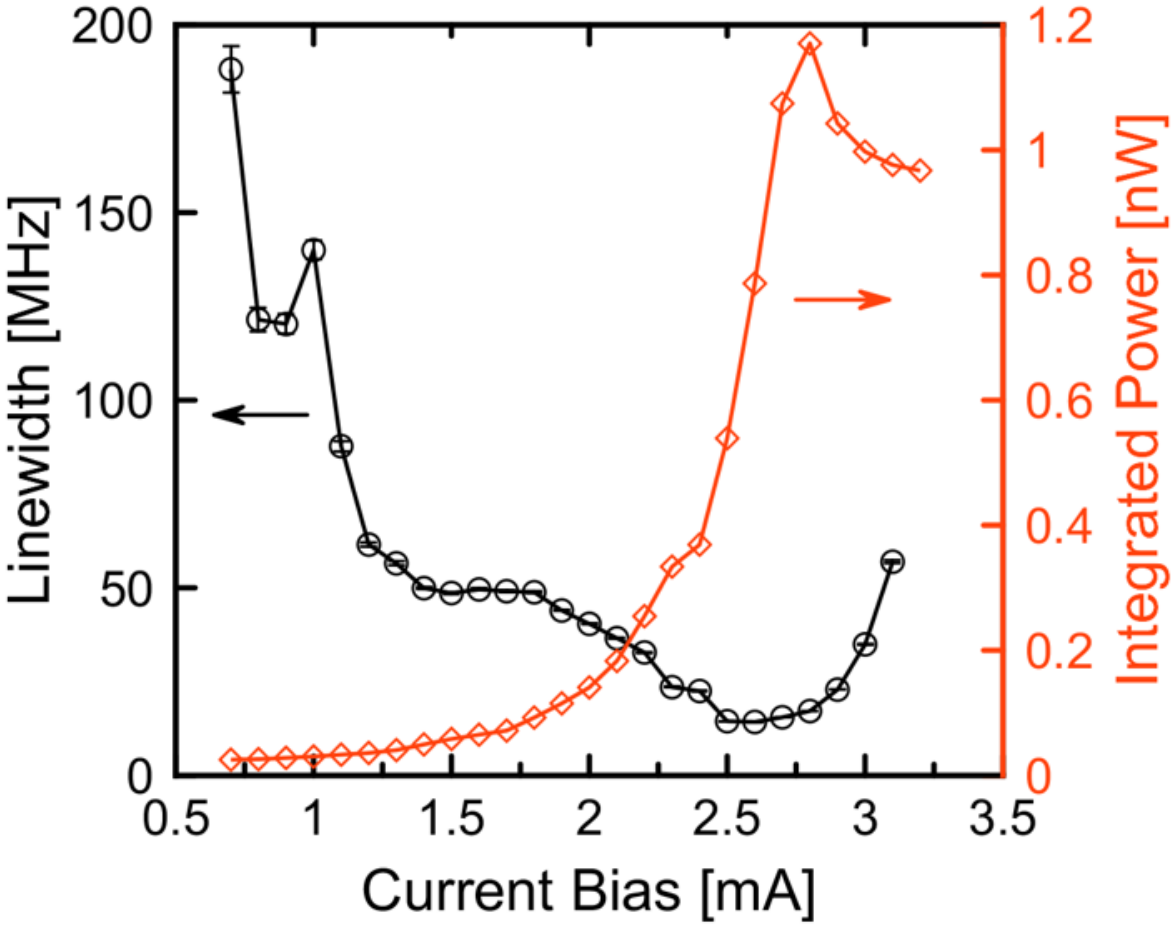

Figure 2.12: Integrated power and linewidth of the quasi-uniform mode as a function of DC current applied to the sample under 600 G field along in-plane hard axis.

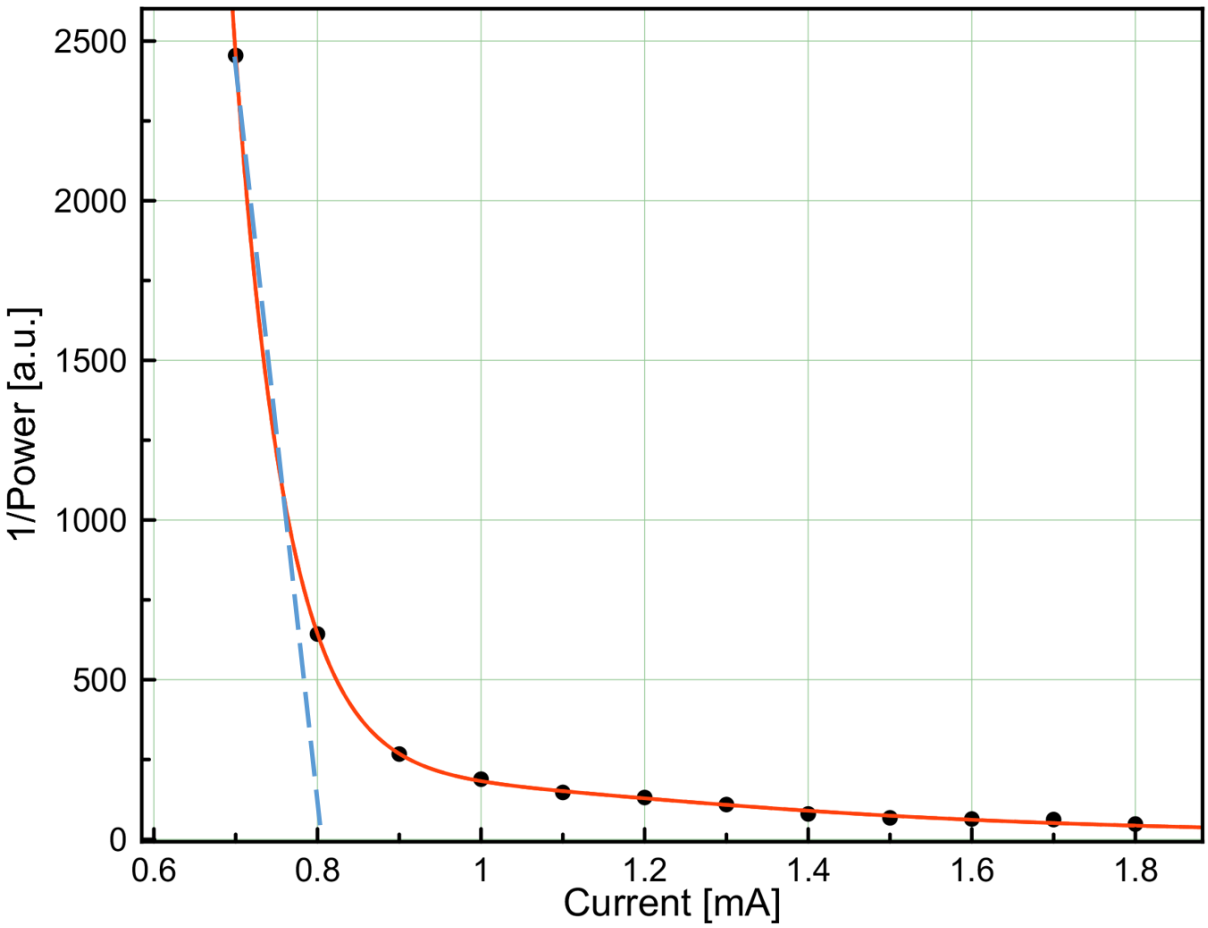

Figure 2.13: Inverse of the integrated power for the quasi-uniform mode in near-threshold range of currents. Same external field is applied. Dashed blue line corresponds to the approximate expression ($1/\bar{p} \propto (I_{th} - I)$ [4]) valid for small currents. Intersection of this line with x-axis gives the value of the critical current: $\sim 0.8\,\mathrm{mA}$.[4]

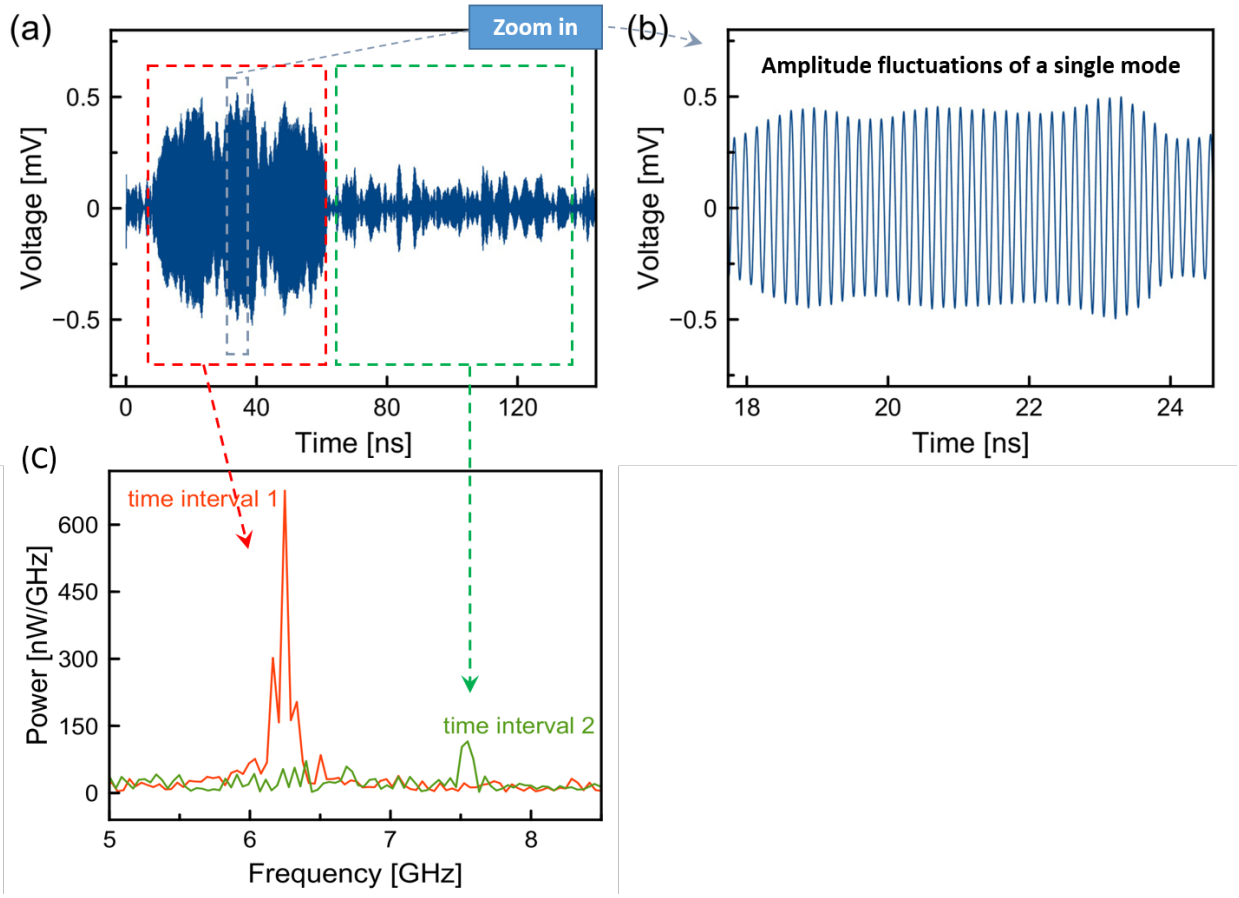

Figure 2.14: (a) Part of the time trace of the generated voltage signals at 2.7 mA, showing hoping between two modes; (b) zoom in oscillation signals of the quasi-uniform mode; (c) separate fourier transform spectra for the corresponding time intervals shown in (a).

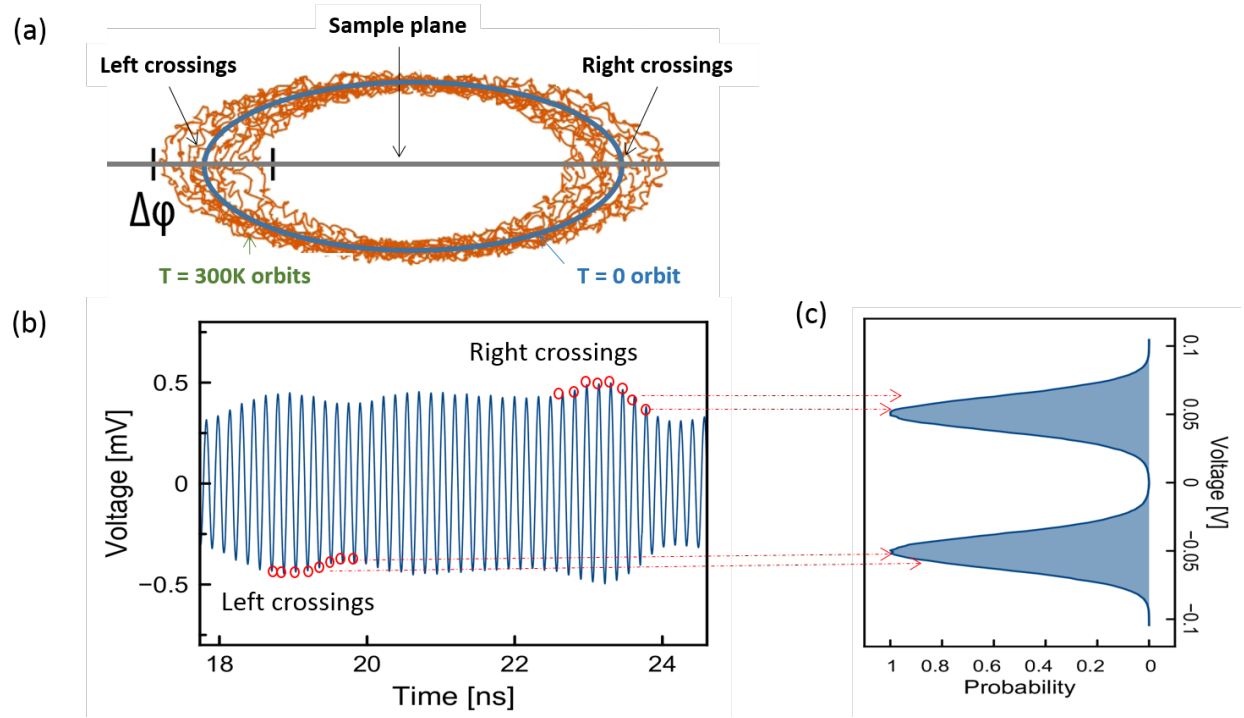

Figure 2.15: (a) A schematic diagram describes the magnetization orbits across the sample plane at both zero and room temperature; (b) generated output voltages according to the oscillating orbits and magnetoresistance; (c) distributions of the extremes of the voltage signals, corresponding to the left and right crossings over the sample plane by the orbits in (a).

2.4 Analysis of Time Domain Data

Although magnetization dynamics in spin torque oscillators (STOs) are readily observed in the frequency domain, time domain analysis can provide a comparative wealth of information. Fig. 2.14(a) shows partially time domain data of the generate voltage signals. Mode hopping is obviously captured in this time window. And respectively, fourier transforms of the two time intervals of these modes are given in Fig. 2.14(c). The quasi-uniform mode possesses lower frequency and larger amplitude, while the 2nd mode has higher frequency and much smaller amplitude. This mode hopping process is one contribution to the linewidth broadening. The zoom in observation of the quasi-uniform mode is plotted in Fig. 2.14(b).

The amplitude of this mode still fluctuates in time due to thermal kicks. We are interested in understanding these intrinsic dynamics properties of this quasi-uniform mode.

Fig. 2.15 illustrates the procedure of reconstructing in part the ensemble of magnetization trajectories followed by the sample's free layer. At zero temperature, the trajectory of magnetization is a well defined orbit symmetric with respect to the sample plane. Finite temperature results in thermal fluctuations of the orbit, but doesn't break its symmetry, as shown in Fig. 2.15(a). Due to this symmetry, crossings of the sample plane by the orbit correspond to maxima and minima of the time-dependent resistance of the device. Thus, time domain data allow us to map these plane crossing angles by recording the left and right crossing distributions. Like in Fig. 2.15(b), the maxima of the measured voltage signals correspond to the right crossings, while the minima represent the left crossings. These voltage extremes have a distribution shown in Fig. 2.15(c). Applying the angular dependence of GMR provided by Eq. 2.3, these voltage distributions can be transformed into the crossing angle distributions. This analysis relies on the error-free extraction of all successive extrema in the emitted voltage signal of the STO and a reliable mapping of the measured voltage onto the physical orientation of the free layer's magnetization vector.

The trace shown in Fig.2.16 apparently exhibits noise signals due to electronic and thermal fluctuations. Therefore, some manner of smoothing procedure is prerequisite for data processing. Since the timescale of fluctuations in the data is clearly much shorter than the oscillation period, it is feasible to smooth the data using a low-pass filter in Fourier space. The cut-off frequency for this low-pass filtering can be slightly above the frequency where the quasi-uniform oscillations produce no power. The noise feature of the amplifier increases to well above its base value of 1.3dB below 300 MHz, and thus we also perform high-pass filtering above this frequency as long as it is well separated from any spectral features of the auto-oscillations. This procedure preserves the peak amplitudes and locations, and is implemented easily using FFTs in any of a variety of free (or proprietary) libraries. After

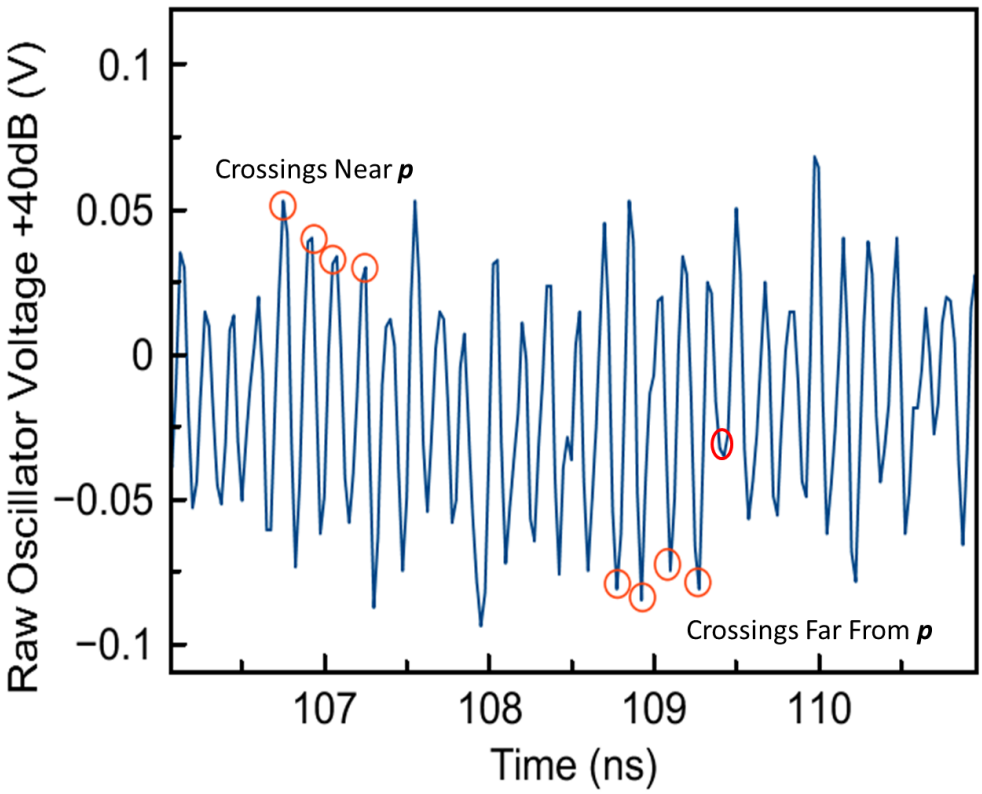

Figure 2.16: Raw data of volrage time trace. Some of the extrema near and far from the polarization vector $\vec{p}$ are indicated.

inversely fourier transforming the data back to the time domain, the ringing artifacts will be induced at the edges of the trace. The simplest methods to get rid of this artifact is to throw away the data at the edges, as we have enough time traces for mapping the crossing distributions.

In addition, about only 7 data points are recorded in each period using the maximal sampling rate of the scope (40 Gs/s), which is not enough for accurate peak extractions. Therefore, we also apply 10 times data interpolation on the filtered time traces to guarantee the accuracy of peak selections. A python implementation of the procedures above can be accomplished in just a few lines.

Band-Pass Filtering

```
import numpy as np
# phi is the experiment data mapped to in-plane angles
fft = np.fft.fft(V)
# Find the maximum frequency value fmax
maxFreq = np.abs(fft[500:np.ceil(len(fft)/2)]).argmax()+500
# High frequency cutoff determined empirically as multiple of fmax
cutoffHigh = int(np.ceil(1.4*maxEl))
# Drop anything sub 300 MHz due to amp noise
cutoffLow = int(np.ceil(300.0e6/(1.0/time[-1])))
# Trim the Fourier spectrum, remembering it is two-sided
fft[cutoffHigh:len(fft)-cutoffHigh] = np.zeros(len(fft)-2*cutoffHigh)
fft[1:cutoffLow+1] = np.zeros(cutoffLow)
fft[len(fft)-cutoffLow-1:len(fft)-1] = np.zeros(cutoffLow)
# Transform back for the smoothed data
smoothV = np.real(np.fft.ifft(fft))

# Cut 7 osc periods' data at both the beginning and end of
# the smoothed trace
smoothV_cutedge = smoothV[51:len(smoothV)-50]

#interpolation:
time_cutedge = np.linspace(0,timestep*(len(smoothV_cutedge)-1),
len(smoothV_cutedge))
V_inp = np.zeros(len(smoothV_cutedge)*10)
time_inp = np.zeros(len(smoothV_cutedge)*10)

func = interp1d(time_cutedge[:], smoothV_cutedge[:], kind = 'cubic')
```

```
time_inp = np.linspace(time_cutedge[0], time_cutedge[-1], len(V_inp))
V_inp[:] = func(time_inp[:])
```

Then these voltage signals can be converted into crossing angles quickly in Python according to Eq. 2.3:

Angle Mapping

```
Rext          = 5.0 # from probes, contacts, etc.
Ravg          = Ravg - Rext
# Circuit properties
## ampl is the calibrated amplification value for different frequency
atten         = -10.0**(-ampl/20.0) # -1 for inverting
refl          = 50.0/(Ravg + Rext + 50.0)
attenoverrefl = atten/refl
deltaR_EA     = 0.683 ## Rap - Rp
deltaR_HA     = 0.256 ## R (600G, HA) + Roffset — Rp
X = 3.05              ## const symmetry parameter
# map voltage to in-plane crossing angles
deltaR = (V_inp*attenoverrefl/current) + deltaR_HA
phi = np.arccos((deltaR_EA-(2+X)*deltaR)/(deltaR_EA+deltaR*X))
```

One may still observe that there are local extreme in the signal which cannot be removed by the Fourier filtering. The origin of such features may be either from electronic noise or from the stochastic properties of the magnetization dynamics. A simple algorithm can

be implemented for differentiating these causes: one retains local extrema (two subsequent crossings on the same side of the average angle) only when they are widely separated and on the same side of the average angle. This constraint is given by:

$$\frac{\Delta\varphi_{i+1} - \Delta\varphi_i}{\Delta\varphi_i} > a \tag{2.7}$$

which must be satisfied for subsequent values of $\Delta\varphi = \varphi - < \varphi >$ as shown in Fig. 2.17. The value of a for our data is chosen empirically as 0.2. To ensure that no artifacts result from a sharp cutoff, one may instead implement a continuous probability distribution for the rejection of observed local extrema instead of a constant a.

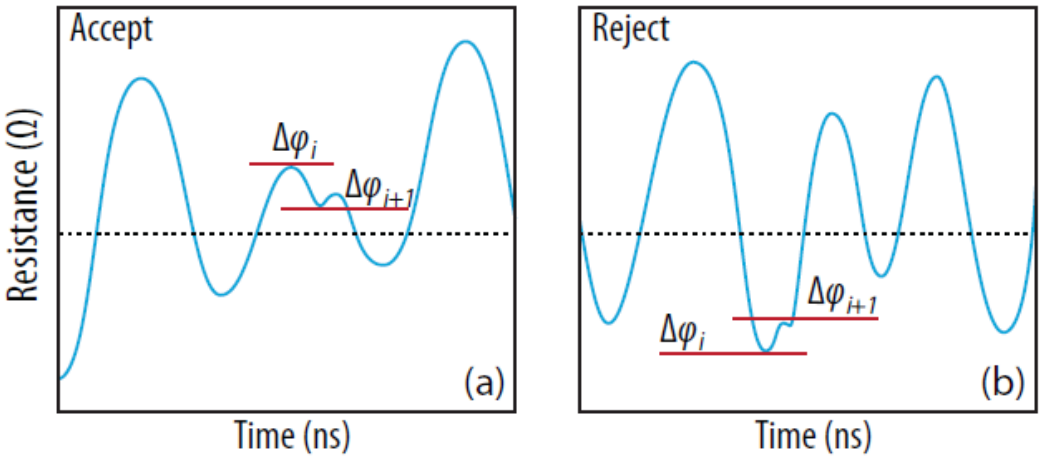

Figure 2.17: [1] Local extreme selection constraint. The $\Delta\varphi$ values are defined as φ minus the average angle of the trace $< \varphi >$. (a) Accepted extrema, which satisfy the condition of Eq. 2.7. (b) Rejected extrema based on the same critierion.

Following algorithm shows the implementation details for extracting the peaks based on the above rejection criterion:

Peak Selection

```
# Derivative of the smoothed signal
diffPhi = np.diff(phi)
# Find zero crossings in derivative (peaks in signal)
# these are the array indices of all the peaks
crossings = np.where(np.diff(np.sign(diffPhi)))[0]
# Find the heights and times of all extrema
peakPhis = phi[crossings]
peakTimes = time[crossings]
# Containers for crossings
phisUp = []
phisDown = []
timesUp = []
timesDown = []
# Loop over crossings, ignores peaks as necessary
for i in range(0,len(crossings)-8):
    thisCrossing = smoothPhi[crossings[i]]
    nextCrossing = smoothPhi[crossings[i+1]]
    thisTime = time[crossings[i]]
    nextTime = time[crossings[i+1]]
    thisDiff = thisCrossing - avgPhi # Δφ_i as defined in the text
    nextDiff = nextCrossing - avgPhi # Δφ_{i+1} as defined in the text
    thisSign = np.sign(thisDiff) # Which side of <φ>
    nextSign = np.sign(nextDiff) # Which side of <φ>

    if (ignore > 0):
        # Decrement ignore counter, but ignore this peak
        ignore -= 1
```

```
    else:
        if (thisSign==nextSign and
        np.abs((nextDiff-thisDiff)/thisDiff) < 0.2 ):
            # Crossing on the same side, and the change is small
            ignore = 2
        # omit spurious R > Rmax
        elif (resistance[crossings[i]] < Rmax[crossings[i]] - 0.02):
            if (nextCrossing < thisCrossing):
                # We are low at the next crossing, and are now high
                phisUp.append(thisCrossing)
                timesUp.append(nextTime-thisTime)
            else:
                # We are high at the next crossing, and are now low
                phisDown.append(thisCrossing)
                timesDown.append(nextTime-thisTime)

# Now the containers defined above hold all crossing events
```

However, this method needs to be employed on the time traces dominated by the low frequency quasi-uniform mode, while our real time domain signals mingle with two modes hopping randomly. To determine whether or not a certain time interval involves with the lower frequency oscillation, one can implement a sliding FFT method to calculate the integrated power within the quasi-uniform mode frequency range for each sliding time window (5 ns is used). We define the threshold value of this power as half of the integrated quasi-uniform power averaged over 20 traces. For each sliding window, only the time interval with the power of the quasi-uniform mode higher than the threshold will be kept for mapping

and recording of the crossing angle distributions. The entire data processing algorithm is included in Appendix A.1.

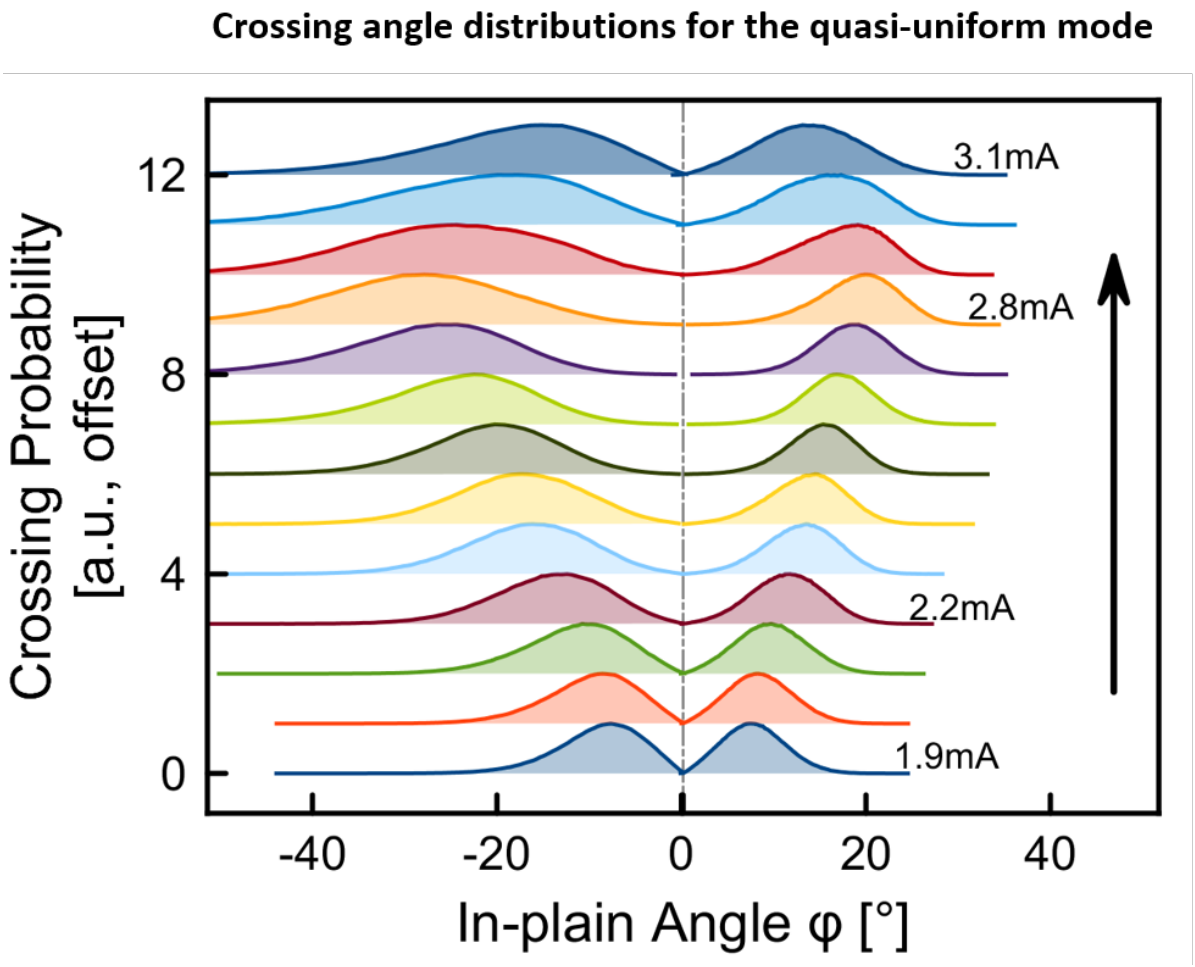

Figure 2.18: In-plane crossing angle distributions for quasi-uniform mode at currents from 1.9 mA to 3.1 mA. External field is applied along in-plane hard axis. X-axis represents the free layer's oscillation cone-angle with respect to the equilibrium position.

Fig. 2.18 illustrates the result of angular mapping distributions for the regime far above the critical current (1 mA). From 1.9 mA to 2.8 mA, the procession angle increases and then decreases above 2.9mA. For current higher than 2.2mA the orbit almost never approaches the static equilibrium point at $\varphi = 0$. Also, the equilibrium position of magnetization does not change with the current bias, which is consistent with negligible field like torque in metallic spin valves. Since the measured STO has circular shape and thus symmetric in-plane shape anisotropy, the crossing distributions of the magnetization orbits should also be symmetric,

unlike the probabilities shown in Fig. 2.18.

After further examination, we found that information loss occurs during the data collection. The limited working bandwidth of our amplifier (0.1 MHz to 8 GHz) distorts the time traces by cutting off the constant and 2nd harmonic mode in the frequency domain. Therefore, some correction procedure is required to be supplemented during the data analysis. In reality, the oscillating angle can be represented by a toy model:

$$\varphi(t) = \varphi_0 + \Delta\varphi \sin(\omega t) \tag{2.8}$$

where $\Delta\varphi$ exists with Gaussian distributions. According to the angular dependence of GMR (Eq. 2.3), one can convert this toy model $\varphi(t)$ into resistance ($R(t)$). By filtering out the higher order modes in the Fourier space and inversely transform back to the time domain, the processed $R(t)$ can reproduce the $R(t)$ time traces recorded in experiment. Thus, a numerical mapping relation between the extrema distributions of $R(t)$ from experiment and $\varphi(t)$ from toy model is able to be established. This corrected mapping procedure solves the discrepancies in our experiment and can be accomplished by some simulations in Python (seen in Appendix A.2).

Based on the dependence of experimental $R(t)$ extrema on the real $\varphi(t)$ extrema, the crossing angle distributions can be directly mapped from the distributions of $R(t)$ extrema in experiment. This corrected mapping result is shown in Fig. 2.19. Crossing distributions at each current are symmetric and have the same trend with increasing current as seen in Fig. 2.18.

These same two dimensional histograms are also reproducible in deterministic simulations with the magnetic Fokker Planck equation, as demonstrated in Section 2.6. We may then perform direct comparisons of expected and observed non-linear dynamic properties, from

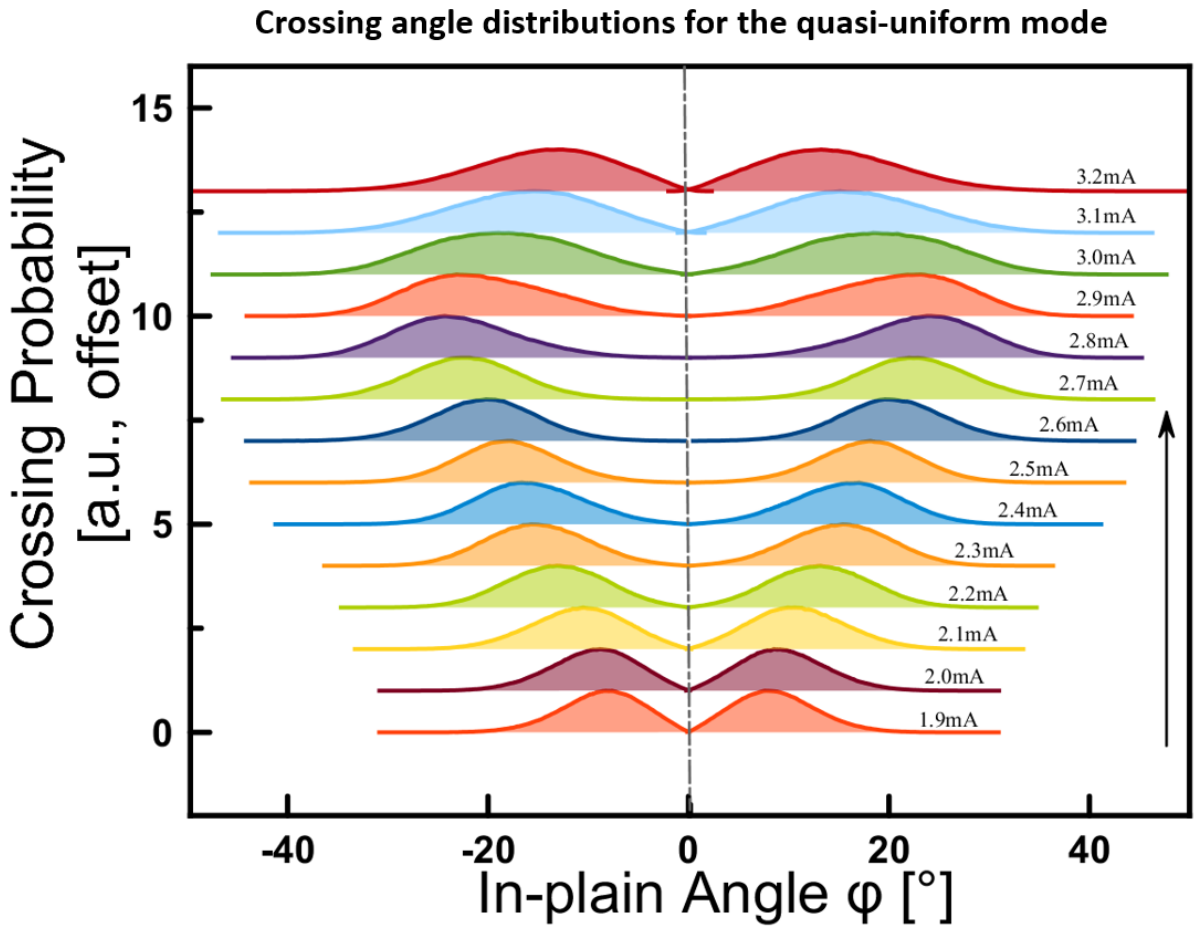

Figure 2.19: Corrected in-plane crossing angle distributions for quasi-uniform mode under currents from 1.9 mA to 3.1 mA. Inverse mapping from toy model of $\varphi(t)$.

which one may garner information regarding the non-linear damping of the sample or other quantities such as temperature.

2.5 Macrospin Simulations

As detailed in Chapter 1, the Landau-Lifshitz (LL) and Landau-Lifshitz-Gilbert (LLG) equations have provided the mathematical basis for explaining magnetization dynamics in nanoscale ferromagnetic heterostructures. For systems that do not measure more than a few exchange lengths in any direction (or those remaining uniform despite not meeting such a

criterion), the magnetization profile can be considered uniform and therefore, of one conserved overall magnetic vector. Such profile allows for a very straightforward treatment of the dynamics. Additional non-conservative spin torque developed by Slonczewski [17, 33, 30] can be included in the LL(G) equation, resulting in what is sometimes referred to as the LL(G)S equation. In the LL form, this equation is given by

$$d\vec{m} = -\vec{m} \times (\vec{h}_{eff} + \alpha\vec{m} \times (\vec{h}_{eff} + \beta_{st}\vec{p}/\alpha)) \cdot dt \tag{2.9}$$

where α represents the Gilbert damping parameter, dt is the time step measured in units of γM_s, fields ($\vec{h}_{eff}$) and magnetic moments ($\vec{m}$) are normalized by M_s, and $\vec{p}$ is a unit vector pointing along with the polarizer. The spin-torque coefficient β_{st} is determined by the mutual angle between $\vec{m}$ and $\vec{p}$ in the form of GMR angular dependence:

$$\beta_{st} = \frac{a_{st} I\hbar}{2eM_s^2 Vol}\left(\frac{P \cdot (\chi + 1)}{\chi + 2 + \chi(\vec{m} \cdot \vec{p})}\right) \tag{2.10}$$

where a_{st} gives the strength of this in-plane torque, P stands for the polarization efficiency, χ is the same asymmetry parameter in Eq. 2.3. This dependence only applies to the case of metallic spin valves.

The damping term α will not always stay as a constant value when magnetization evolves into a large (non-linear) oscillation regime. Generally, it is a function of the change of magnetic moment, and for finite but not very large angles of magnetization procession, it

can be represented as a Taylor series expansion:

$$\alpha(\xi) = \alpha_G(1 + q_1\xi + q_2\xi^2 + ...); \xi \sim \Big| \frac{\partial \vec{M}}{\partial t} \Big|^2 . \tag{2.11}$$

Such a non-linear damping model is developed by Prof. Slavin in 2009 [4], where $\alpha_G \ll 1$ is the linear Gilbert damping parameter, $q_i \sim 1$ are the phenomenological parameters characterizing nonlinear properties of the damping processes. One can tune the parameters q_i to both qualitatively and quantitatively match with our experimental results, and thus observe how this non-linear damping factor behaves in the large angle oscillation regime.

Usually, this differential equation is not able to be solved analytically, except in a case of iso-axial structure. On the other hand, numerical solutions are fairly easy to achieve. Either an explicit or implicit integration step can be chosen for discretization of this equation. In the former method, the left hand side of Eq. 2.9 describes the state at the future timestep t_{i+1}, while the right hand side is evaluated at the previous time t_i. This procedure is the so-called "Forward Euler" integration method, which is expressed as following:

$$\vec{m}_{i+1} = \vec{m}_i - \vec{m}_i \times (\vec{h}_{eff} + \alpha\vec{m}_i \times (\vec{h}_{eff} + \beta_{st}\vec{p}/\alpha)) \cdot \Delta t \tag{2.12}$$

Instead of the detailed version, one can simplify this expression as:

$$\vec{m}_{i+1} = \vec{m}_i + \vec{v}(\vec{m}_i, t_i)\Delta t \tag{2.13}$$

which emphasizes that the torques $\vec{v}$ in the new step must be calculated based on the previous magnetization $\vec{m}_i$. The Forward Euler method cannot converge to a relatively

proper level, unless a sufficiently small time step is implemented. The decent convergence of the solution, as noted in Ref. [48], is proven with a particular renormalization procedure of the magnetization. Since one cannot guarantee the conservation of $|\vec{m}| = 1$ during the Forward Euler evaluation, this periodical renormalization of $\vec{m}$ is applied to reduce this deviation.

Another choice for the discretization is the "Backward Euler" method, which yields

$$\vec{m}_i = \vec{m}_{i-1} + \vec{v}(\vec{m}_i, t_i)\Delta t \tag{2.14}$$

which now contains the future $\vec{m}_i$ on both sides of the equation. As generally there are no analytic solutions, one can rearrange this equation as following:

$$0 = \vec{m}_{i-1} - \vec{m}_i + \vec{v}(\vec{m}_i, t_i)\Delta t \tag{2.15}$$

and solve it with the Newton-Raphson methor or some other root-finding algorithm. The convergence of this Backward method performs better as well as the stability for a larger Δt.

At last we focus on an implicit midpoint integration method which preserves $|\vec{m}|$ and always yields a decreasing free energy in the presence of damping[49, 50]. This method relies on

evaluating the derivative of Eq. 2.9 at the midpoint:

$$\frac{d\vec{m}}{dt} \mid_{i+1/2} \approx \frac{\vec{m}_{i+1} - \vec{m}_i}{\Delta t} = \vec{v}(\vec{m}_{i+1/2}, t_{i+1/2}) \tag{2.16}$$

and thus leads to the midpoint stepping algorithm:

$$\vec{m}_{i+1} = \vec{m}_i + \vec{v}(\vec{m}_{i+1/2}, t_{i+1/2})\Delta t \tag{2.17}$$

which is not useful at all due to the lack of knowledge of the intermediate step $\vec{m}_{i+1/2}$. Taylor expansion of $\vec{v}(\vec{m}_{i+1/2}, t_{i+1/2})$ with respect to t_i provides a solution for this stepping algorithm:

$$\vec{m}_{i+1} = \vec{m}_i + \vec{v}(\vec{m}_i + \frac{\Delta t}{2}\vec{v}(\vec{m}_i, t_i), t_{i+1/2})\Delta t. \tag{2.18}$$

It can be demonstrated that this midpoint method is intrinsically norm preserving, and also intrinsically energy preserving if all non-conservative torques are neglected. A Python implementation of this implicit midpoint algorithm for a general case at room temperature is shown in Appendix A.3.

2.5.1 Interactions with Stochastic Field

At room temperature, thermal fluctuations plays an important role in the time evolution magnetic dynamics. Thus, deep understanding of the nature of the stochastic process and the corresponding interpretation in the differential equations are required. The noise is incorporated as a random thermal field with uncorrelated Gaussian white noise vector component, whose magnitudes are able to be learned by the fluctuation dissipation theorem. The LL and LLG equations in the presence of these noise terms needs to be modified with the calculus of random stochastic fields. Two of the most common interpretations for these differential equations are those of Stratanovich and Itō. Followed by Stratanovich's sense, Eq. 2.9 becomes

$$d\vec{m} = \vec{v}(\vec{m}, t)\, dt - \nu\vec{m} \times (d\vec{W} + \alpha\vec{m} \times d\vec{W}) \tag{2.19}$$

while an extra deterministic drift term must be added in the version of Itō:

$$d\vec{m} = [\vec{v}(\vec{m}, t) - \nu^2\vec{m}]\, dt - \nu\vec{m} \times (d\vec{W} + \alpha\vec{m} \times d\vec{W}). \tag{2.20}$$

Here ν is the magnitude of thermal fluctuations, $d\vec{W}$ stands for the isotropic Wiener (Guassian white noise) process, and $\vec{v}(\vec{m}, t)$ contains all the deterministic torques described earlier. The difference between these interpretations lies in the meaning of the sum required for the solution. The integration is ill-defined with a measure of $d\vec{W}$, so instead the limiting case of a Riemann sum is applied as the definition. In fact, a choice like that between Midpoint and Euler methods is made for the relative time steps at which the random and determin-

istic torques are evaluated. The details of this choice is related to the system's properties, and salient discussion can be found elsewhere [48]. The midpoint algorithm is nevertheless well adapted to the numerical integration, except that we don't want to evaluate $\vec{W}$ at the midpoint. Thus, a slightly different approximation has been made based on Eq. 2.18:

$$\vec{m}_{i+1} = \vec{m}_i + \vec{v}((\vec{m}_{i+1} + \vec{m}_i)/2, t_{i+1/2})\,\Delta t + \vec{u}((\vec{m}_{i+1} + \vec{m}_i)/2, t_{i+1/2}) \cdot \Delta\vec{W} \tag{2.21}$$

where function $\vec{u}()$ has absorbed the matrix representation of the stochastic torques in Eq. 2.19 or Eq. 2.20. The random thermal fluctuation $\Delta\vec{W}$ is selected once per timestep and the root-finding algorithm proceeds with that fixed variable. Appendix A.3 shows the Python implementation of our Macrospin simulation with this midpoint method including the stochastic field.

2.5.2 Analysis of Macrospin Simulation Results

Fig. 2.20 illustrates an example of the simulation result for a self-oscillation state at $T = 0$ (under 600 G in-plane applied field perpendicular to the exchange bias). The spectrum in the frequency domain is shown in Fig. 2.20 (a); 2D- and 3D-oscillation orbits of the free layer's magnetization are shown in Fig. 2.20 (b) and (c) respectively. The orbit is almost well defined and completely coherent. While Fig. 2.21 depicts the auto-oscillatory state at room temperature. It is obvious that finite temperature induces thermal fluctuations in the orbits, which results in the amplitude and phase diffusion during the oscillation. STOs exhibit spectral broadening both from these phase noise and amplitude noise coupled into phase noise by virtue of the strong nonlinearity of the system. Further investigations based on the crossing angle histograms will be combined with the Fokker Planck effective energy

approach in section 2.6.

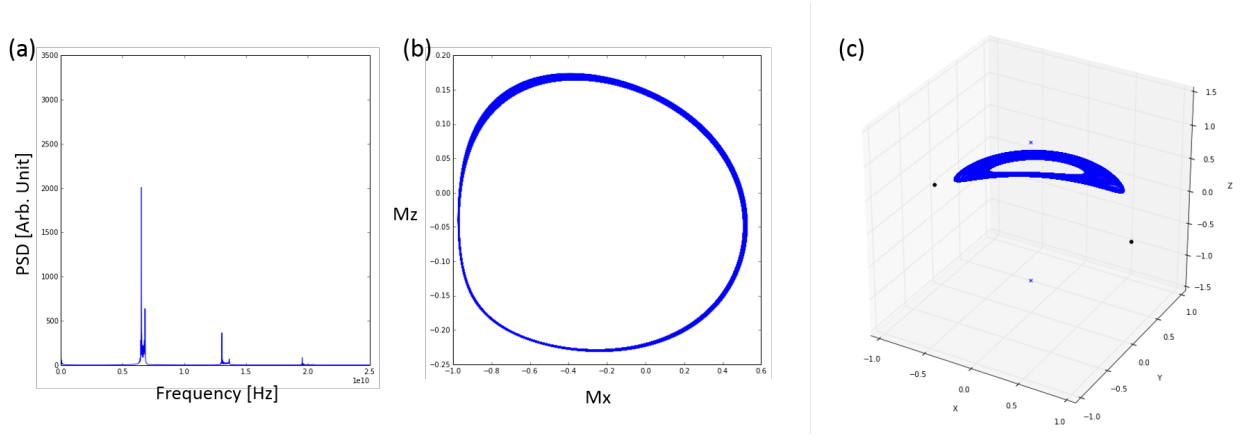

Figure 2.20: A simulation example of the auto-oscillatory state for the free layer of our STO device at $T = 0$. 600 G field is applied perpendicular to the exchange bias. (a) FFT of x component of the oscillating magnetization. (b) Projection of the magnetization trajectories: z-component vs. x-component. (c) 3D plotting of the magnetization trajectories.

One interesting phenomenon occurs for the macrospin simulation in the case of external field $H_{ext} = 600\,G$ perpendicular to the exchange bias: auto-oscillation cannot be excited with constant damping and correct angular dependence of spin-torque ($\chi = 3.05$), while self-oscillation does exist in experiment under the same applied field. Hence, we further examine the effect of nonlinear damping [4, 51] on spin torque driven auto-oscillations in our sample's free layer by numerically solving Landau-Lifshitz equation with a nonlinear damping term in the macrospin approximation. Fig. 2.22 describes the dependence of the excited auto-oscillation frequency on the angle of effective field, which is defined with respect to the opposite direction of the polarizer. Three regimes of self-oscillatory dynamics are observed. For small applied field angles, the onset of self-oscillations is soft – the amplitude of self-oscillations is small just above the critical current. For higher angles, hard onset of self-oscillations is observed – large-amplitude in-plane oscillations are observed immediately above the critical current. At yet higher angles, large-amplitude out-of-plane oscillations are excited immediately above the critical current. Fig. 2.22 shows that nonlinear damping significantly extends the angular range for the soft onset of the auto-oscillations and leads to an extended angular range where auto-oscillatory dynamics are present. The same applied

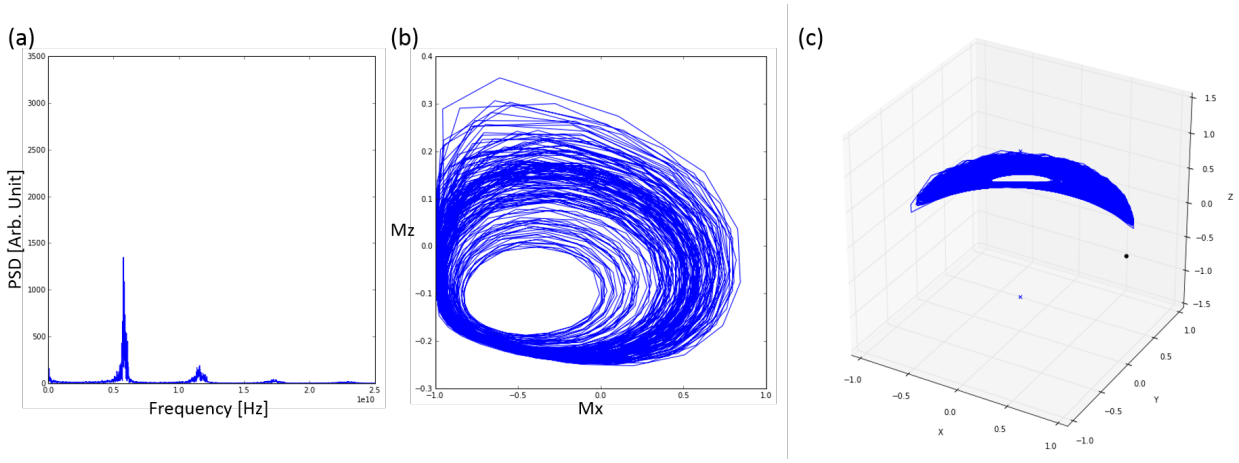

Figure 2.21: A stochastic simulation example of the auto-oscillatory state for the free layer of our STO device at $T > 0$. 600 G field is applied perpendicular to the exchange bias. (a) FFT of x component of the oscillating magnetization. (b) Projection of the magnetization trajectories: z-component vs. x-component. (c) 3D plotting of the magnetization trajectories.

field condition with experiment ($H_{ext} = 600\,G$) corresponds to the HeffAng of 66° seen in Fig. 2.22, at which the onset of auto-oscillation requires the nonlinear damping to balance out the extra amount of spin torque contribution. Deeper study of the non-linear damping term will be discussed within the framework of Fokker Planck approach in the next section.

2.6 Calculation in the Fokker-Planck Theory

2.6.1 Introduction of General Fokker-Planck Equation

Instead of concerning the stochastic variants in the LL or LLG equations, the time evolution of the probability distribution p of the magnetic moment can be expressed deterministically through the magnetic Fokker-Planck equation, bypassing the integration of individual random thermal field. This prescription was first proposed by Brown in 1963 [52]. The

derivation of p,

$$\frac{\partial p}{\partial t} = -(\frac{\partial J_\theta}{\partial \theta} + \frac{\partial J_\varphi}{\partial \varphi}), \tag{2.22}$$

is determined by the currents of probability:

$$J_\theta = [-\frac{1}{\sin\theta}\frac{\partial g_L}{\partial \varphi} - \alpha\frac{\partial \Phi}{\partial \theta} + \nu^2 \cot\theta]\, p + \frac{\nu^2}{2}\frac{\partial p}{\partial \theta}, \tag{2.23}$$

$$J_\varphi = [\frac{1}{\sin\theta}\frac{\partial g_L}{\partial \theta} - \frac{\alpha}{\sin^2\theta}\frac{\partial \Phi}{\partial \varphi}]\, p + \frac{\nu^2}{2}\frac{1}{\sin^2\theta}\frac{\partial p}{\partial \varphi} \tag{2.24}$$

where θ and φ are the polar and azimuthal angles, g_L is the free energy, and Φ represents the generalized potential of the system (including the non-equilibrium torques) [48]. The field-like torque is always considered as an effective field contribution to g_L. Since g_L and Φ are explicitly known, derivative of these equations with respect to the spherical coordinates are readily evaluated.

The main problem now is that of drift and diffusion on the magnetization sphere starting from some initial probability distribution of the magnetization. For convenience, we generalize the Fokker-Planck equation into the form of

$$\frac{\partial p}{\partial t} = \nabla[-\mathbf{A}\cdot p + \frac{1}{2}\nabla(\underline{\mathbf{B}\mathbf{B}}^T \cdot p)] \tag{2.25}$$

where $\mathbf{A}$ is the drift vector and $\underline{\mathbf{BB}}^T$ is the diffusion tensor in Cholesky form. The gradient operator ∇ is not defined on the spherical manifold, but rather on the projected circular surface of polar and azimuthal angles: $\nabla \equiv < \partial/\partial\theta, \partial/\partial\varphi >$. Thus, the drift vector and diffusion tensor relate to the coefficients of Eq. 2.22 by:

$$\mathbf{A} = \begin{pmatrix} -\frac{1}{\sin\theta}\frac{\partial g_L}{\partial\varphi} - \alpha\frac{\partial\Phi}{\partial\theta} + \nu^2\cot\theta \\ \frac{1}{\sin\theta}\frac{\partial g_L}{\partial\theta} - \frac{\alpha}{\sin^2\theta}\frac{\partial\Phi}{\partial\varphi} \end{pmatrix}, \underline{\mathbf{B}} = \begin{pmatrix} \nu & 0 \\ 0 & \nu/\sin\theta \end{pmatrix}. \tag{2.26}$$

Then one multiplies both sides of Eq. 2.25 by a test function q and integrates over the entire spherical manifold $(\sum)$. Distribution p is recognized as the trial function in this procedure. After integration and careful evaluation of the boundary conditions, the first term on the right hand side (RHS) of Eq. 2.25 becomes

$$\int_{\sum} d\mathbf{x}\nabla q \cdot \mathbf{A}p; \tag{2.27}$$

meanwhile, the second term yields

$$-\int_{\sum} d\mathbf{x}[\frac{1}{2}(\underline{\mathbf{BB}}^T \cdot \nabla q) \cdot \nabla p - [q\underline{\mathbf{B}} \cdot (\nabla \cdot \underline{\mathbf{B}})] \cdot \nabla p] \tag{2.28}$$

where the divergence is defined to proceed along rows of $\underline{\mathbf{B}}$. The time evolution is discretized

by the Crank-Nicolson method before integration:

$$\begin{aligned}
&\frac{\partial p}{\partial t} = F(\mathbf{x}, t) \\
&\frac{\partial p}{\partial t} \approx \frac{p - p_0}{\Delta t} \equiv \frac{p^{n+1} - p^n}{\Delta t} = \frac{1}{2}[F(\mathbf{x}, t^{n+1}) + F(\mathbf{x}, t^n)]
\end{aligned} \tag{2.29}$$

where $p \equiv p^n$ is the known solution for the previous time step and $p_0 \equiv p^{n+1}$ is the solution for the current step. By assembling Eq. 2.27, 2.28, and 2.29, p can be solved implicitly through the final time stepping algorithm:

$$\begin{aligned}
&\int_{\sum} d\mathbf{x}(pq + \frac{\Delta t}{2}[-\nabla q \cdot \mathbf{A}p + \frac{1}{2}(\underline{\mathbf{B}}\underline{\mathbf{B}}^T \cdot \nabla q) \cdot \nabla p - [q\underline{\mathbf{B}} \cdot (\nabla \cdot \underline{\mathbf{B}})] \cdot \nabla p]) \\
&= \int_{\sum} d\mathbf{x}(p_0 q - \frac{\Delta t}{2}[-\nabla q \cdot \mathbf{A}p_0 + \frac{1}{2}(\underline{\mathbf{B}}\underline{\mathbf{B}}^T \cdot \nabla q) \cdot \nabla p_0 - [q\underline{\mathbf{B}} \cdot (\nabla \cdot \underline{\mathbf{B}})] \cdot \nabla p_0]).
\end{aligned} \tag{2.30}$$

The left hand side of this equation is of the bilinear form $a(p, q)$ which depends on both the test and trial functions. The RHS is of the linear form $L(p)$ which only depends on the test function and the solution of the previous step. The initial probability distribution p_0 must be supplied, which is chosen to be a 2D Gaussian distribution in θ and φ. Detailed codes and packages for the evolution of magnetization distribution p are shown in Ref [1].

While much information can be gained from solving this general Fokker-Planck formalism for stochastic magnetization dynamics, much effort is lost due to the expensive computation and the physical meaning of the contribution from spin-torque or non-linear damping term is blurred during the derivation. In next section, we demonstrate a simplified method which transforms the calculation coordinate to the energy system, and therefore reduces the computational burden as well as relates the physical terms to the non-linear behavior more

directly.

2.6.2 Calculations in the Effective Energy Framework

In the circumstance of the steady state of self-oscillations, one can assume that magnetic moment mainly evolves along conservative orbits, although it is induced by thermal torques to slowly diffuse among these trajectories (on a timescale much longer than its oscillation period). It turns out to be a valid assumption for many STO systems, as the non-conservative terms like spin-torque and damping are fairly small compared to the conservative fields from demagnetization and Zeeman interaction (besides, they will cancel out to some extent since they are opposite to each other). Inspired by this assumption, one can collapse the dynamics represented in the spherical coordinates onto the energy wells corresponding to the conservative orbits [53]. This procedure relies on the one-to-one mapping between orbits and energies according to the in-plane crossing angles, thus each well must be separated into which the manifold may be divided and then subsequently be stitched together with these separate solutions.

When a steady self-oscillation is being excited, one cannot ignore the non-conservative contributions to the magnetization dynamics from spin-torque and damping torque. In this scenario, the occupation of various orbits is not only determined by the conservative energy terms, but rather the effective energy which has been modified by the non-equilibrium torques acting on the magnetization. The following steps illustrate the prescription on how to calculate this effective energy surface of a nano-magnet:

1. Derive the conservative energy expression $E(\theta, \varphi)$ of the nano-magnet system, including contributions from external field, dipolar field, demag field, etc.. φ corresponds to the in-plane crossing angles.

2. Find the corresponding effective field $\vec{H}_{eff}(\theta,\varphi) = -dE/d\vec{M}$. $\vec{H}_{eff} = \vec{H}_{external} + \vec{H}_{dipolar} + \vec{H}_{demag}$ for the free layer in our sample (detailed expression shown in appendix A.5).

3. Starting from the minimum of the energy well at φ_0 (E_0), numerically integrate over all conservative trajectories of $\vec{m}_j(t)$ based on the starting coordinate $\varphi_j = \varphi_0 + \Delta\varphi$, and gradually farther from the bottom of the energy well by increments of $\Delta\varphi$. The orbit marked by the starting in-plane crossing angles φ_j can also be indexed by the corresponding conservative energy E_j.

4. Calculate the work done by the spin-torque along each conservative trajectory,

$$I_M(E) = \oint \beta(\varphi)[d\vec{M} \times \vec{M}] \cdot \hat{p}, \tag{2.31}$$

where $\hat{p}$ is the unit polarization vector of the spin current. $\beta(\varphi) = \frac{P(\chi+1)}{\chi+2+\chi\cos\varphi}$ gives the angular dependence of spin-torque in metallic spin valve structures, in which $P = 0.224$ represents the polarization efficiency of our sample (calculated according to Ref. [33]), χ is the asymmetry parameter fitted earlier, φ stands for the angle between $\vec{m}_f$ and $\vec{m}_p$.

5. Calculate the work done by the damping torque along the same trajectories,

$$I_E(E) = \oint \alpha(\xi)[d\vec{M} \times \vec{H}_{eff}] \cdot \hat{m}, \tag{2.32}$$

where $\alpha(\xi)$ provides the non-linear damping term, which is equal to $\alpha_G(1+q_1\xi+q_2\xi^2+...)$; $\xi \sim \left| \frac{\partial \vec{M}}{\partial t} \right|^2$ described in Eq. 2.11. $\xi \sim \left| [\hat{h}_{eff} \times \hat{m}] \right|^2$ when spin torque and damping torque are negligibly small in comparison to the conservative torques.

6. Numerical integrations of $I_M(E)$ and $I_E(E)$ for each trajectory can be easily accomplished

in software packages as Python. Once we know the ratio of these two works,

$$\eta(E) = \frac{I_M(E)}{I_E(E)}, \tag{2.33}$$

the effective energy surface is able to be obtained by integrating this ratio from the bottom of the well up to the current energy value,

$$E_{eff}(E) - E_{eff}(E_0) = E - E_0 - \frac{J}{M_s}\int_{E_0}^{E} \eta(E^{'})dE^{'}, \tag{2.34}$$

which tunes the conservative energy well through the work done by non-conservative torques.

7. The energy distribution is normally non-Boltzmann, except for the case of conservative torques only. However, the probability distribution can be expressed in the Boltzmann form as

$$\rho^{'}(E) = \frac{1}{Z} exp(-V[E_{eff}(E) - E_{eff}(E_0)]/k_B T), \tag{2.35}$$

where $\rho^{'}(E)$ shows the probability per unit area of the system existing at the energy level of E, V is the domain's volume, k_B is the Boltzmann constant, and Z is the partition function as following:

$$Z = \int dE^{'} \gamma M_s \tau(E^{'}) \rho^{'}(E^{'}) \tag{2.36}$$

in which $\tau(E)$ gives the period of the trajectories.

So far, all of the basic machinery is ready for making any ensemble calculation in the Fokker-Planck effective energy approach. For example, the ensemble of the averaged value of some parameter $y(E)$ (which depends on the occupation of a particular orbit) can be generalized in the manner below:

$$< y >= \int dE^{'} \rho^{'}(E^{'}) A(E^{'}) \delta(E^{'} - y^{-1}(E^{'})), \tag{2.37}$$

where $A(E)dE = \gamma M_s \tau(E)dE$ is the area of the orbits between energy E and $E + dE$, and δ represents the Dirac delta function.

Detailed derivation of the effective energy based on the LL equation and Fokker-Planck theory is shown in Appendix A.4. In addition, the numerical calculation of E_{eff} at various currents is implemented by Python programming, which is included in Appendix A.5.

2.6.3 Result Analysis in comparison with Experiment

According the macrospin energy model of the free layer of our sample (Eq. 2.4), one can determine the oscillation trajectory corresponding to each conservative energy (equivalent to the crossing angle of the sample plane). Thus, numerical integration over these trajectories can be accomplished for our sample's free layer. Fig. 2.23 shows the angular dependence of the effective energy profiles calculated by the Fokker-Planck approach with constant damping parameter. At zero current, effective energy is equal to the conservative energy and the equilibrium angle is defined to be zero in our coordinate. As current increases, the effective energy well becomes shallower due to the influence of spin torque. When current approaches

the critical, the well becomes flat. Correspondingly, the crossing angle distributions turn to be broadened in this region as the restoring torques on the orbits become smaller. When the current exceeds the critical, the potential well splits into two wells and the plane crossing angles become clustered near these two minima. These current (or spin-torque) dependent effective energy profiles theoretically explain the dynamics of the magnetic moment from the static state to the state far above the onset of auto-oscillatory regime.

Now, based on the measured crossing distributions, we can apply the Fokker-Planck approach to calculate the experimental effective energy profile of the free layer in our sample. The Fokker-Planck approach gives a Boltzmann-like energy distribution for the system shown in Eq. 2.35. Meanwhile, the crossing angle distribution can be connected with the energy probability as following:

$$\rho_{cross}(\varphi) = \rho(E(\varphi)) \left| \frac{dE}{d\varphi} \right| \tau(E) \tag{2.38}$$

Therefore, from these two equations, one can obtain the effective energy just by using the angular distribution from the experiment. Fig. 2.24 describes the translating procedure from the measured angular distributions to the experimental effective energy profiles.

In Fig. 2.25, we compare effective energies predicted by the macrospin Fokker-Planck theory to our experimentally measured effective energy profiles. Two striking differences are found between theory and experiment. First, the angular separation of the two effective energy wells above the critical current is much smaller in the experiment than in theory. In experiment, the largest oscillation cone angle is around 20° at 2.7 mA; while in theory with constant damping, the cone angle already achieves 100° at only 1.5 mA. Second, the inter-well separation starts to decrease at the highest current employed in the measurements,

while it is a monotonically increasing function in the theory. One possible explanation of the observed discrepancies would be that the theory does not take into account non-linear damping which tends to decrease the precession amplitude.

As one can tell from Eq. 2.11, the nonlinear damping increases with the precession cone angle, which to some extent indicates its importance for the large angle oscillation regime. Hence, in the next step, we modify the Fokker-Planck model with the nonlinear damping term as well as tune the characterizing parameters q_i to achieve the best fit with experiment. Fig. 2.26 shows that with $q_1 = 4.35$, the cone angles are almost consistent between experiment and theory, which demonstrates the effect of non-linear damping on limiting the precession cone angle in the regime far above critical current.

In conclusion, we have shown that time domain measurements are able to provide direct mapping of the spin-torque dependent effective energy of the STO even at the regime far above critical current. Also, we developed a macrospin Fokker-Planck effective energy model which allows for a quantitative determination of the non-linear damping parameters (q_i in Eq. 2.11) through the comparison with experiment. We demonstrated that above the critical current, the inter-well separation in the measured energy profile appears to be smaller than that expected from Fokker-Planck approach with constant damping. However, a modified Fokker-Planck model with nonlinear damping term is capable to reach qualitative agreement with the experiment, which confirms the crucial effect of non-linear damping in oscillation regime far above critical current.

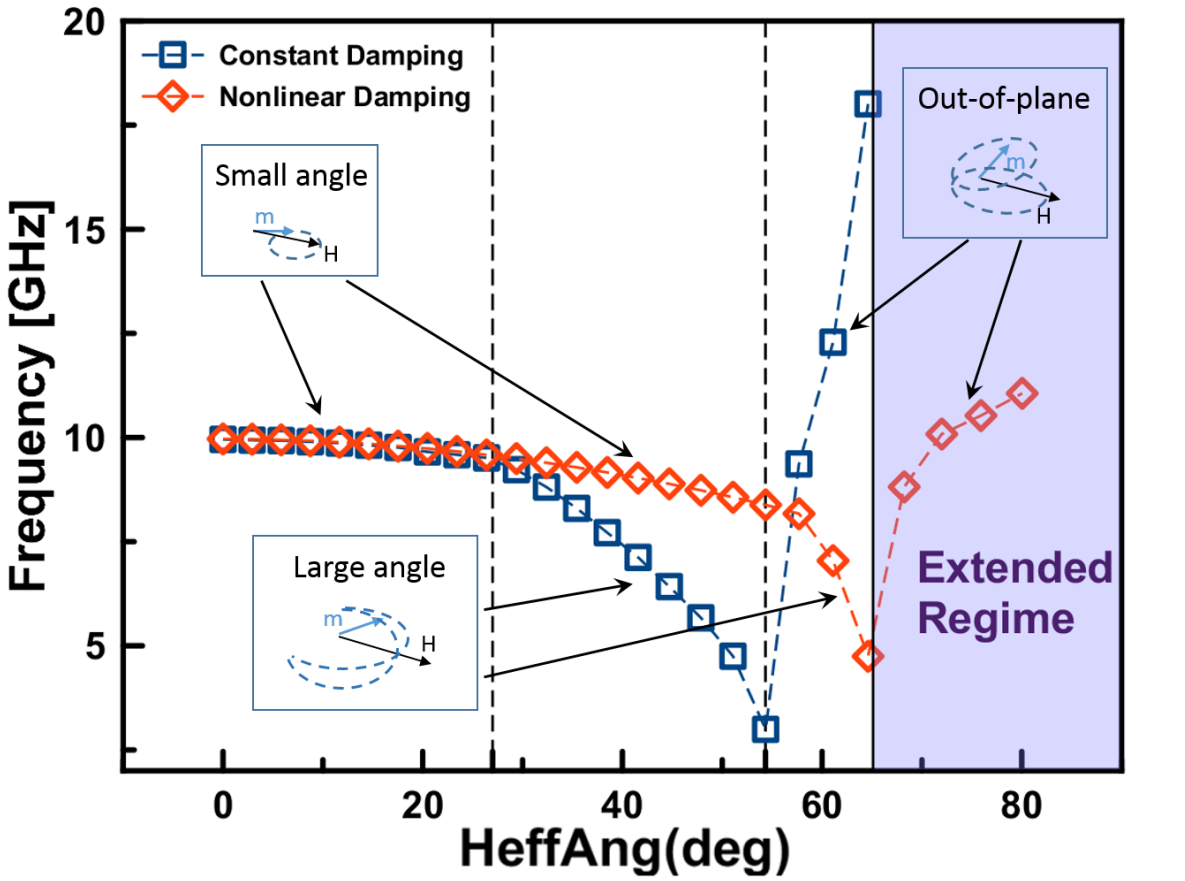

Figure 2.22: Comparison of auto-oscillation frequency at the critical current for constant Gilbert damping and nonlinear damping ($q_1 = 0.3$) in the macrospin approximation. HeffAng is the effective field angle with respect to the opposite direction of the polarizer. The effective field is composed of external field and dipolar field from pinned layer. Three regimes of auto-oscillatory dynamics at the critical current are observed: small-amplitude, large-amplitude in-plane and large-amplitude out-of-plane oscillations. Nonlinear damping is found to extend the angular range of auto-oscillatory dynamics.

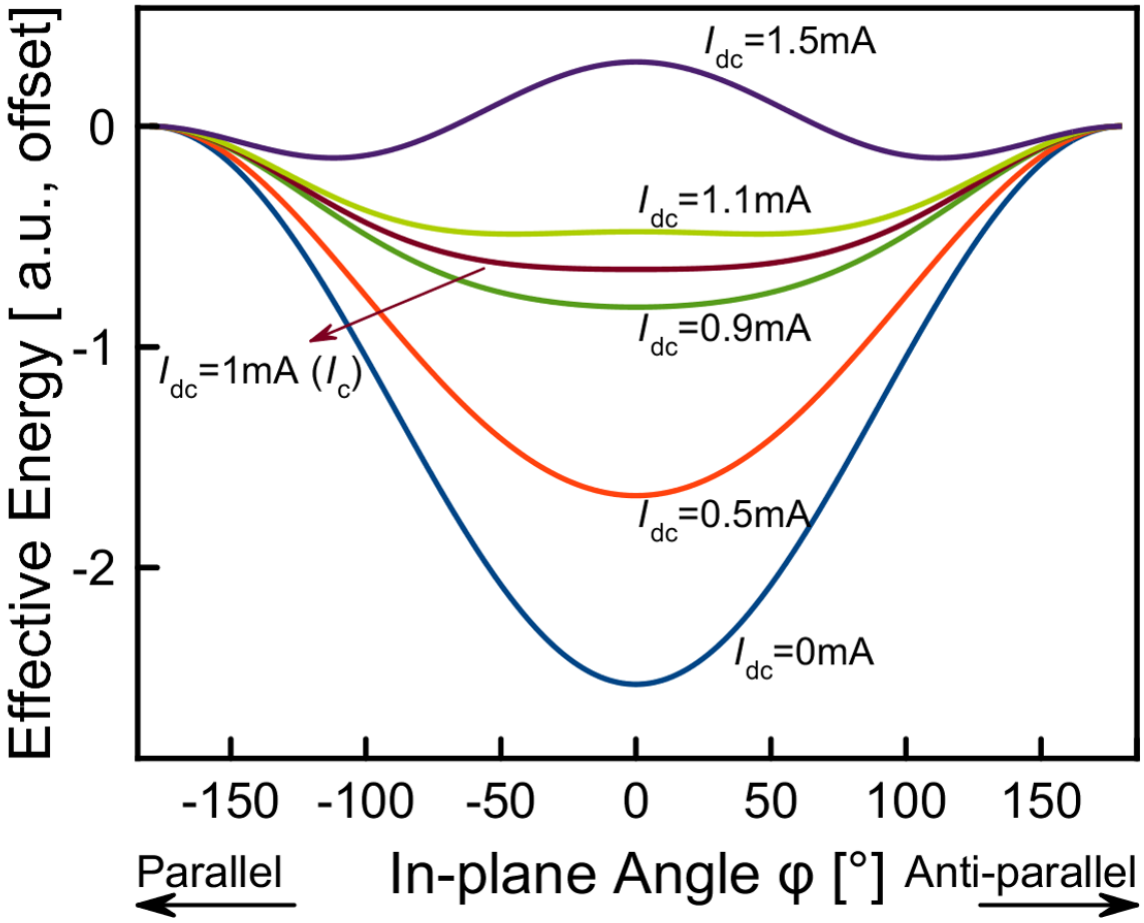

Figure 2.23: Effective energy profiles for various currents developed by the spin-torque dependent Fokker-Plank model. Constant damping is applied.

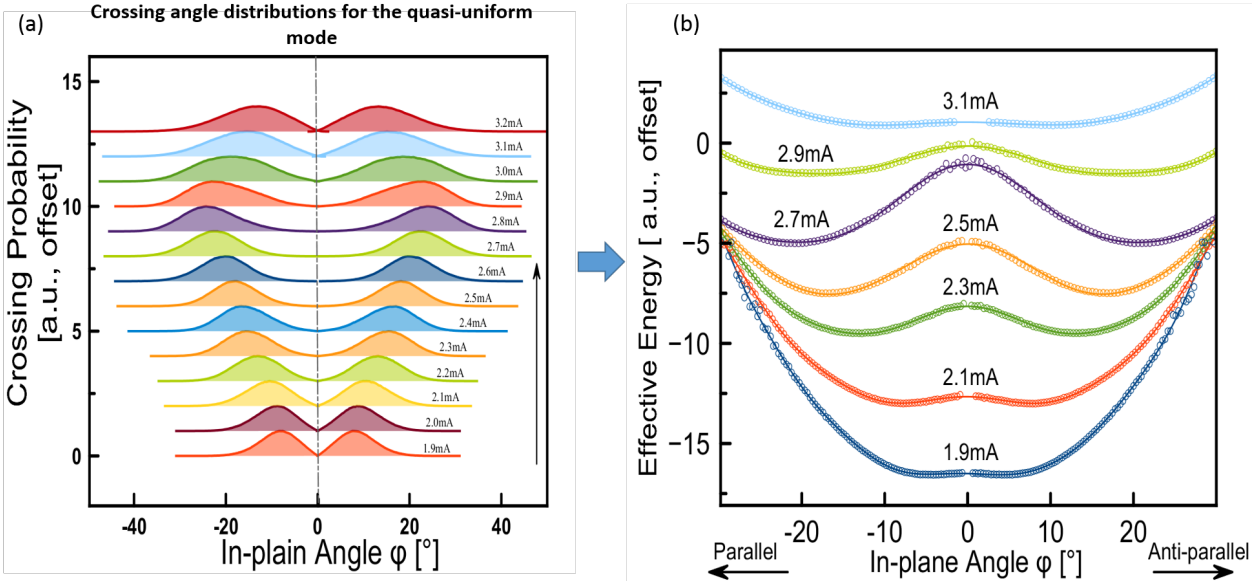

Figure 2.24: (a) Measured in-plane crossing angle distributions for currents far above the critical. (b) Experimental effective energy profiles calculated by the Fokker-Planck method, based on the measured crossing distributions shown in (a).

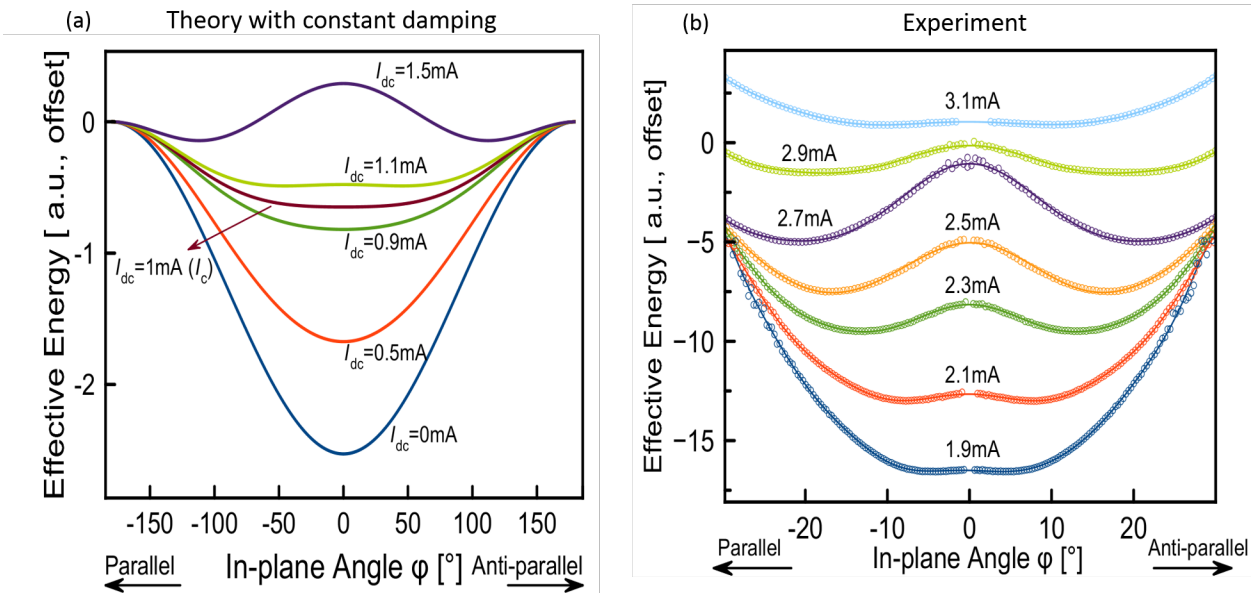

Figure 2.25: (a) Effective energies predicted by the macrospin Fokker-Planck theory with constant damping applied. (b) Experimentally measured effective energy profiles.

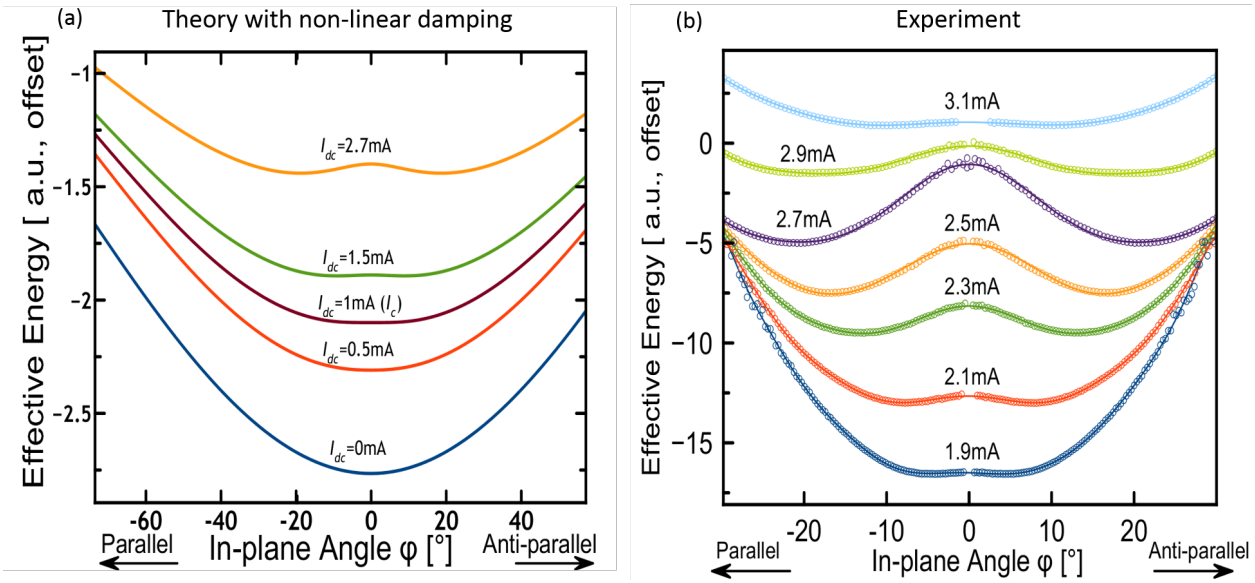

Figure 2.26: (a) Effective energies predicted by the macrospin Fokker-Planck theory with implementation of non-linear damping ($q_1 = 4.35$). (b) Experimentally measured effective energy profiles.

Chapter 3

Microwave Radiation Detector based on Spin Torque Diode Effect

The microwave radiation detector discussed in this chapter is based on spin torque ferromagnetic resonance (ST-FMR)[19, 20]. Some prior work has explored the use of tunnel junctions as sensing elements [19, 21, 22, 23, 24, 25] using the spin torque diode effect. It has been shown that high detecting sensitivity has already been achieved[26], however, so far wireless detection of microwaves using a magnetic tunnel junction has not been demonstrated. It will be shown that the wireless microwave radiation detector discussed in this chapter has a relatively high sensitivity[21] comparable to a semiconductor diode and is designed to be frequency tunable by adjusting the magnet installed inside. Electrostatic discharge (ESD) protection and mechanical protection have also been implemented in order to make the detector ruggedized for normal use.

Unlike an electromagnetic signal confined in a transmission line (microwave waveguide, microwave cable, etc.), a radiated microwave signal decays quickly. As a result, in order to measure microwave radiation signal, a relatively sensitive detector should be implemented.

The control over source and cable impedances is possible when a source is connected directly to a detector, allowing improved impedance matching and better overall detection efficiency. However, the impedance of air is a constant so that some circuit optimization is required to couple microwave signals to the sensing element. The design presented in this chapter includes a compact antenna suitable for this purpose.

In this chapter I will describe the design of this microwave radiation detector and the characterization of detectors with two different types of tunnel junctions. We compared their sensitivities and demonstrated the frequency tunable function. Furthermore, a detector with a pair of two parallel MTJs is developed for enlarging the frequency detection range. The characterization result will also be discussed in this chapter. In this project, the formal group member Brian Youngblood designed the detector and ran the basic performance comparison between detectors with different types of MTJs. I have improved the ESD and mechanical protection onto the circuit of the detector. I also accomplished the demonstration of the frequency tunable function and the working detector with an MTJ array.

3.1 Detector Design

A schematic circuit diagram of the detector is given in Fig. 3.1. In our detector, we use MTJs with MgO barrier due to its large magnetoresistance[9, 15, 54]. The source of RF current is a coplanar waveguide (CPW) acting as an antenna, which is directly attached to the MTJ. The top lead of the MTJ is connected to the AC+DC port of a bias-tee while the DC port of the bias-tee is connected to the signal pin of a K-connector. The bottom lead of the MTJ is connected to the flange ground and the chassis of the detector. The DC voltage across the MTJ can be measured through the K-connector. The detector also includes an ESD protection circuit. A permanent magnet is affixed to a set screw to provide DC magnetic field.

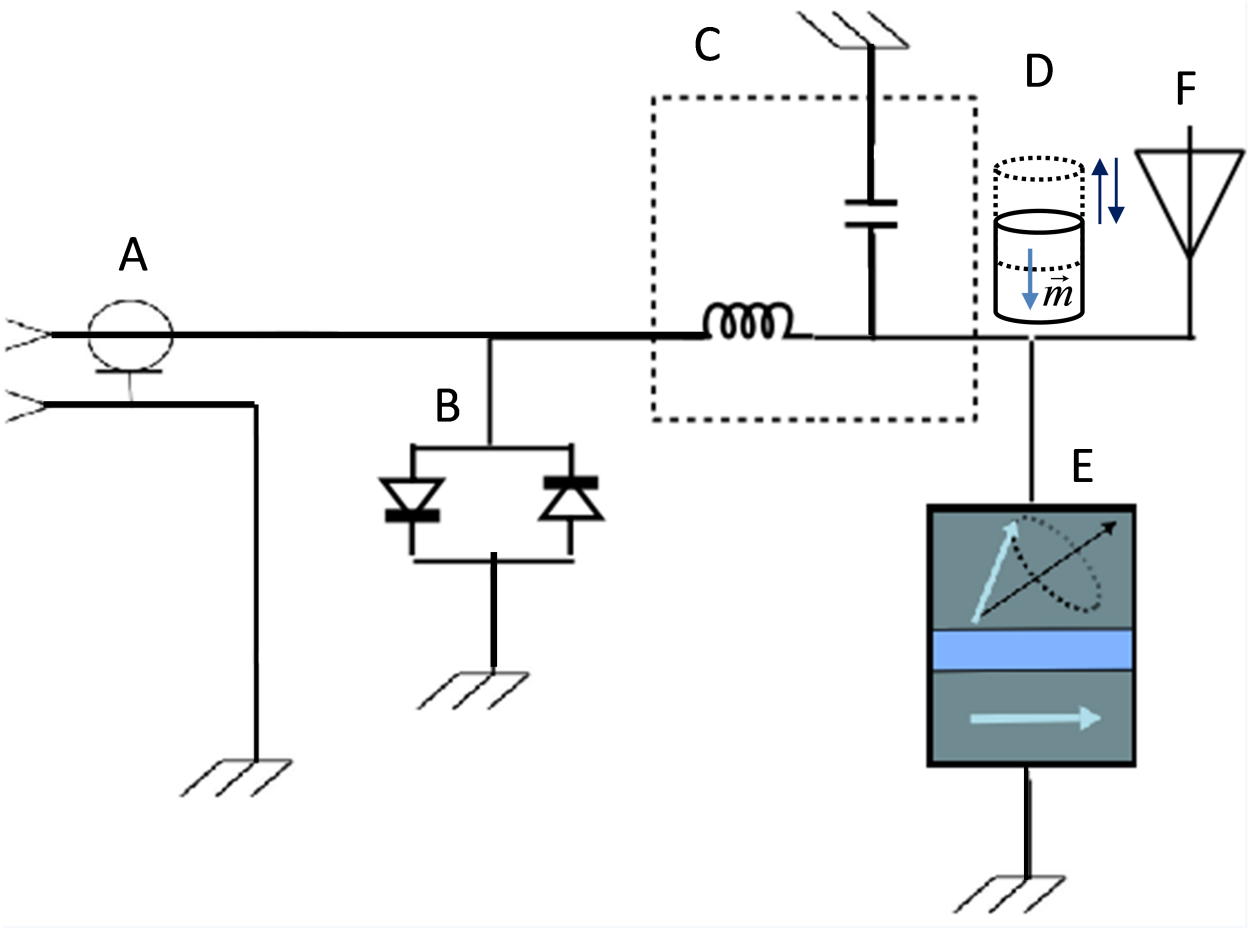

Figure 3.1: Schematic circuit diagram of an MTJ microwave detector. Part A: K-connector; part B: ESD protection circuit; part C: bias tee; part D: magnet with tunable position; part E: MTJ device; part F: coplanar waveguide antenna for receiving microwave signal.

The magnet inside provides a constant field that can be adjusted to obtain the best possible response from the magnetic tunnel junction and to tune the detection frequency range. The magnet is made from $Nd_2Fe_{14}B$ (3.175 mm diameter $\times$ 3.175 mm long) with a nominal surface field of 4 kG. The tunable position of the magnet provides a magnetic field range between 0 and 800 G applied at the MTJ. This range covers the fields which give the maximum response for the two types of detectors in our measurement.

The CPW makes the detector capable of picking up ambient microwave radiation (of the correct polarization) and, via the MTJ, converting it to a measureable DC voltage. It couples

the microwave radiation to an input RF signal at the tunnel junction efficiently. This requires reasonably good matching between the impedance of CPW and that of air.

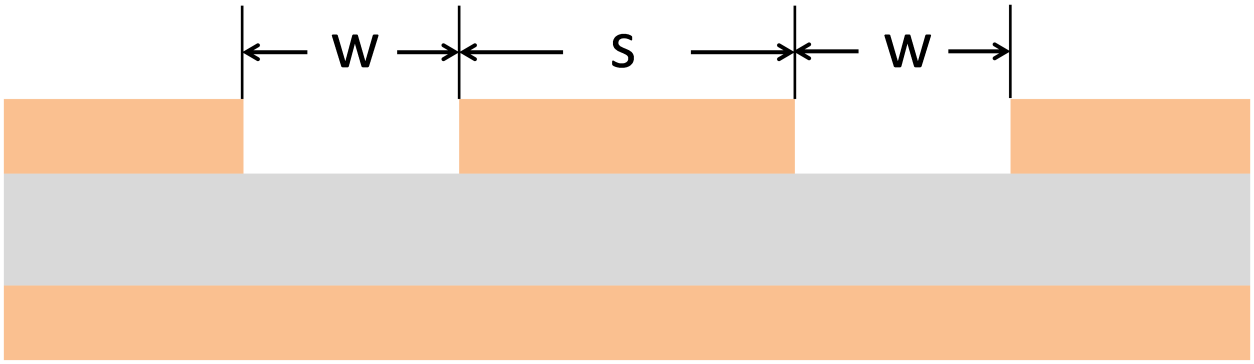

Figure 3.2: Cross-sectional view of a coplanar waveguide showing relevant dimensions. The yellow section stands for the metal part of the coplanar waveguide. The grey part represents the dielectric substrate in the middle, which is made of Duroid.

In an analytic model, a grounded CPW as depicted in Fig. 3.2 with a dielectric (ϵ_r) substrate of thickness $h >> b = s + 2w$ has an impedance [55]:

$$\frac{60\pi}{\sqrt{\epsilon_{eff}}} \frac{1}{\frac{K(k)}{K(k')} + \frac{K(k_1)}{K(k_1')}} \tag{3.1}$$

$$\epsilon_{eff} = \frac{1 + \epsilon_r \kappa}{1 + \kappa} \tag{3.2}$$

$$\kappa = \frac{K(k')}{K(k)} \frac{K(k_1)}{K(k_1')} \tag{3.3}$$

$$k = s/b \tag{3.4}$$

$$k' = \sqrt{1 - k^2} \tag{3.5}$$

$$k_1 = \frac{tanh(\pi s/4h)}{tanh(\pi b/4h)} \tag{3.6}$$

$$k_1' = \sqrt{1 - k_1^2} \tag{3.7}$$

As indicated by these equations, the characteristic impedance of the CPW is proportional to w and is inversely proportional to s. By modeling the coplanar waveguide structure in the finite element calculation software CST Microwave Studio, we were able to determine the parameters (s,w) showed in Fig. 3.2, which maximize the gain of the CPW antenna but still render the sample relatively easy to fabricate. For the 0.254 mm thick Duroid substrate we used, the optimal parameter set is $s = 0.2\,\text{mm}$ and $w = 0.1\,\text{mm}$ giving an impedance of $76\,\Omega$ according to the modeling software. The impedance with the same dimension is $86\,\Omega$ according to the analytical model. This discrepancy between numerical modeling and analytical approximation can be explained by the fact that our real CPW doesn't fulfill the condition $h >> b$.

An additional feature of this detector is the ESD protection circuit designed to prevent damage to the delicate magnetic tunnel junction. The junction is susceptible to breakdown and becomes shorted across its thin insulating layer when exposed to relatively large transient voltages. The ESD protection circuit consists of two Schottky diodes connected in opposite directions which will shunt large voltages of either polarity to ground.

Fig. 3.3 shows the detailed design layout of our entire detector and the major dimensions are given by Fig. 3.4.

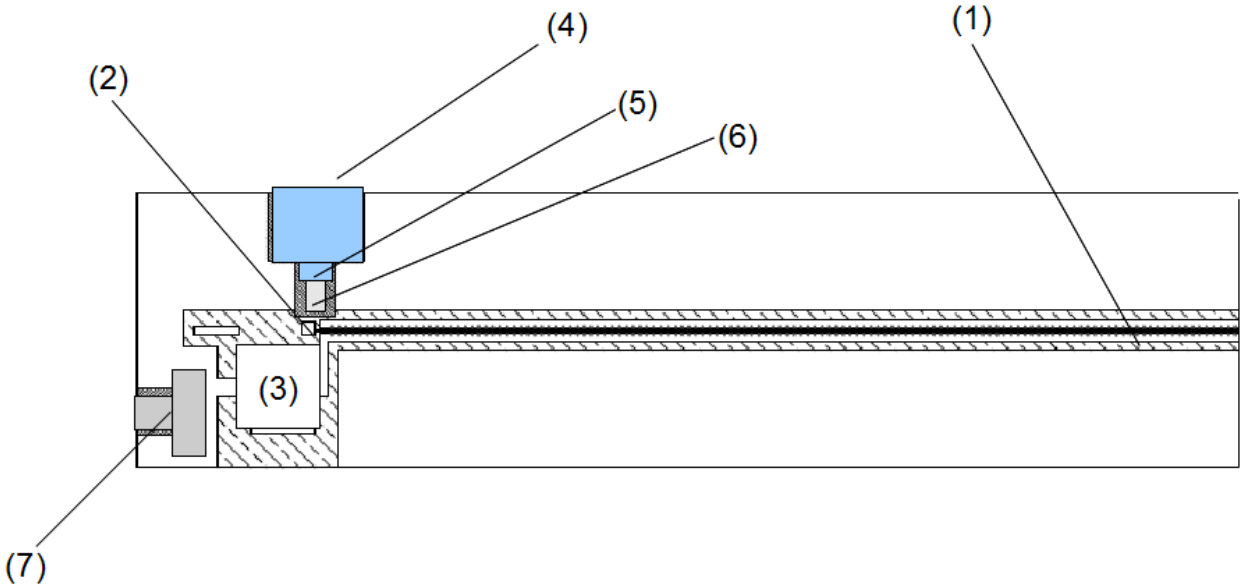

Figure 3.3: Microwave detector layout components: (1) Coplanar waveguide antenna, (2) MTJ device, (3) Bias-tee, (4) Brass screw holder, (5) Brass set-screw, (6) NdFeB magnet, (7) K-connector flange

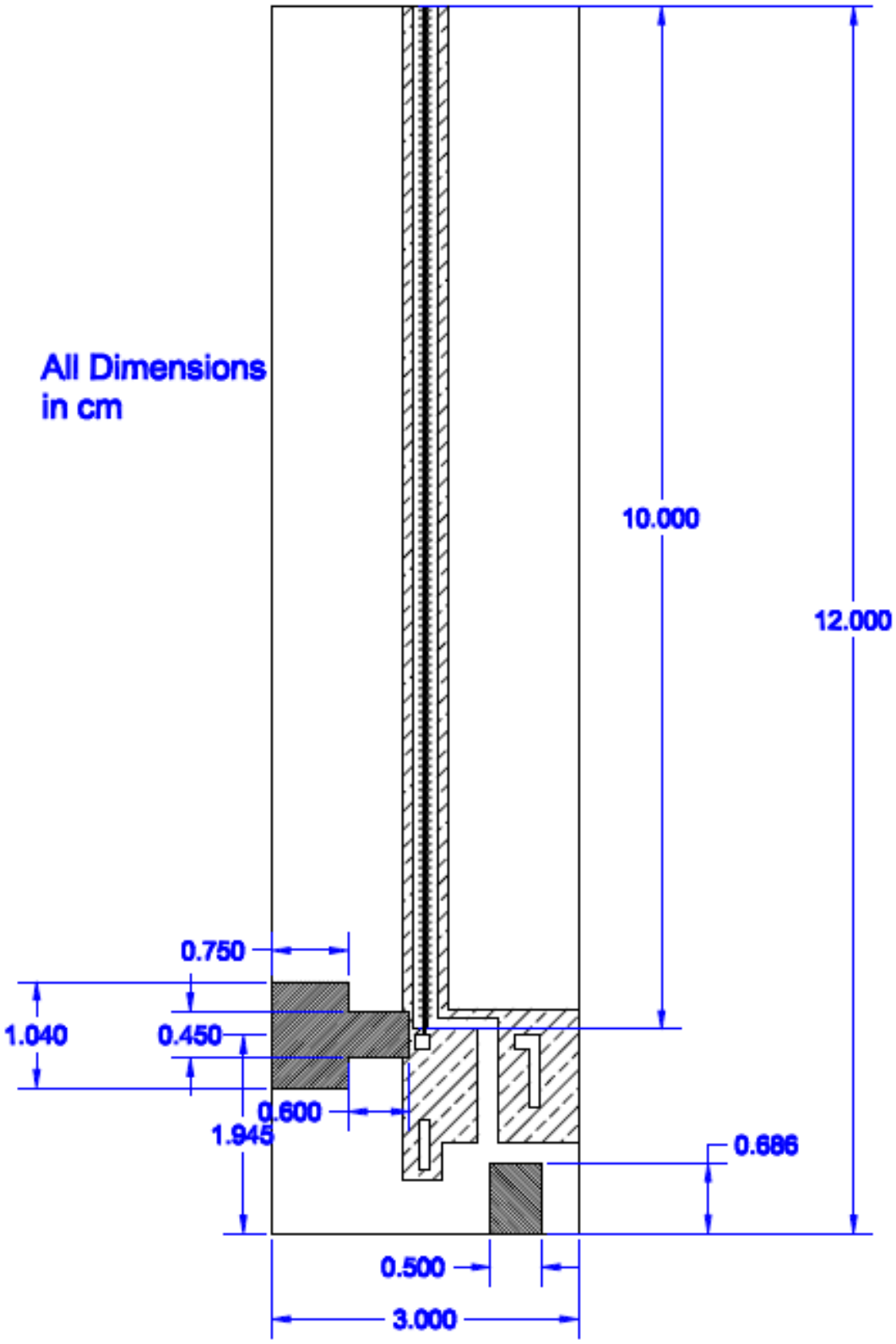

Figure 3.4: Dimensions of the assembled microwave detector

3.2 Experimental Results

For the detectors studied in this project, two different types of MTJs[9, 15, 54] were used, which will be referred to as type A and type B. Both are elliptical MgO tunnel junctions with CoFeB fixed and free layers. The layer structure is Substrate/buffers/SAF/MgO/FL. SAF refers to the synthetic anti-ferromagnet layer. FL is the free layer in the MTJ device. For type A junctions, the SAF is composed of PtMn(16)/$Co_{70}Fe_{30}$(2.5)/Ru(0.85)/$Co_{60}Fe_{20}B_{20}$(2.4), and the FL is $Co_{60}Fe_{20}B_{20}$(1.8) which is magnetized entirely in plane. The SAF structure for type B junctions is PtMn(15)/$Co_{70}Fe_{30}$(2.3)/Ru(0.85)/$Co_{40}Fe_{40}B_{20}$(2.4). The FL of type B junctions is composed of $Co_{20}Fe_{60}B_{20}$(1.8) which has partially out of plane magnetization. All thicknesses are given in nanometers. A type A junction has Co-rich free layer while type B is Fe-rich.

The resistance of most type A MTJs is between 300 Ω and 350 Ω at zero applied field. For type B junctions, resistances at zero applied field is higher, mostly ranging from 600 Ω to 620 Ω. Resistance vs. field plots for both types of junctions are shown in Fig. 3.5. The field is along the in-plane hard axis, which is the short axis of our elliptical device.

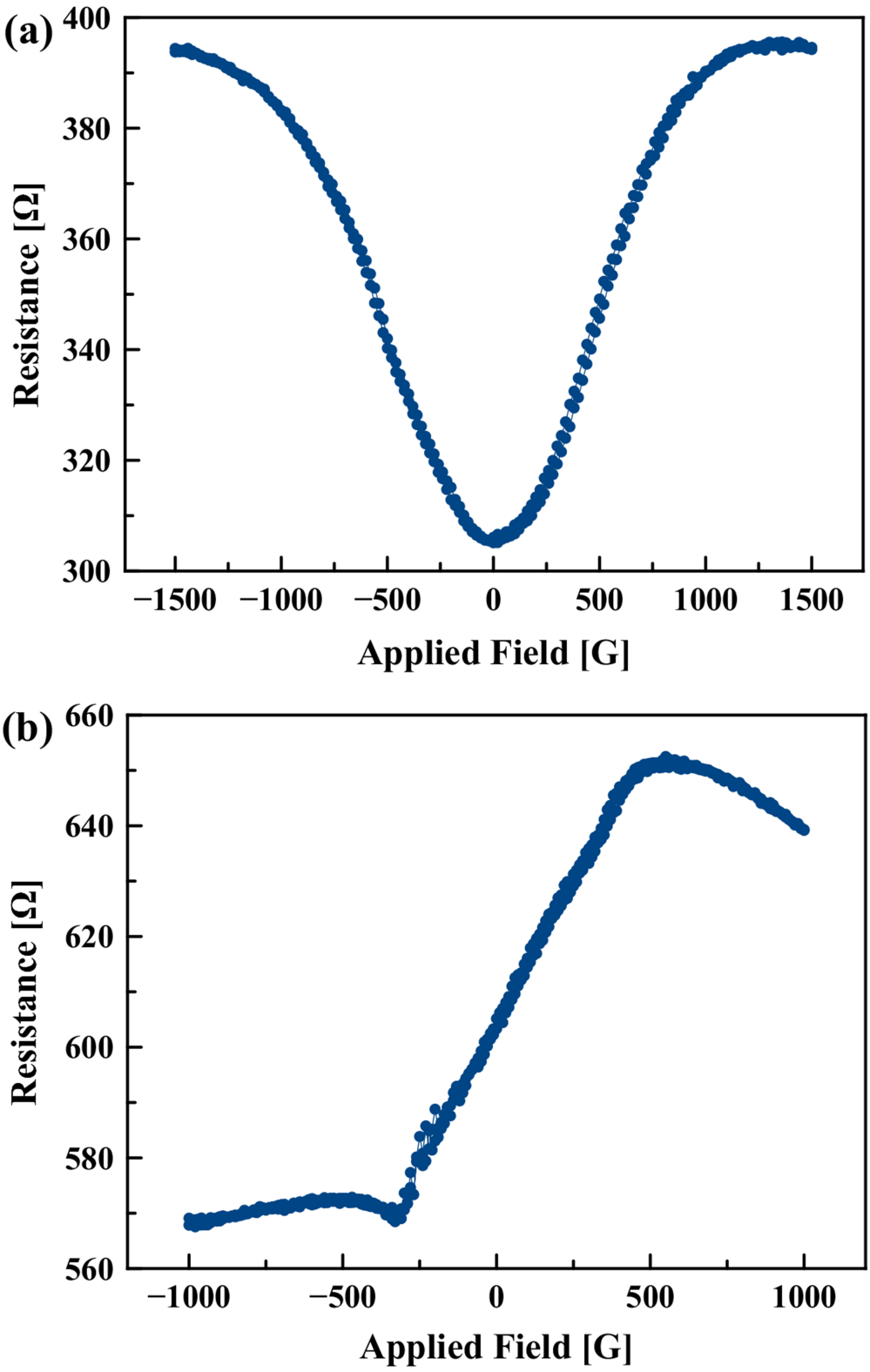

Figure 3.5: Resistance vs field curve for a typical type A(a), and type B(b) MTJ device, with nominal lateral dimensions 160 nm × 65 nm and 150 nm × 70 nm, respectively. Both fields are along in-plane hard axis.

Tests on the full microwave detectors were run by placing the detectors at a set distance (approximately 18 cm) underneath a microwave horn antenna which was in turn connected to a microwave generator. The voltage signal was read by a Keithley 2182A nanovoltmeter which can measure down to 1 nV. This DC voltage was recorded as the frequency of the microwave emissions was varied. Fig. 3.6(a) shows the output voltage at the applied field giving the best signal for a typical detector with a type A tunnel junction patterned into $160 \times 65\,nm^2$ elliptical nanopillar. This result was obtained with an external field of about 650 G along in-plane hard axis and a signal generator power output of 15 dBm.

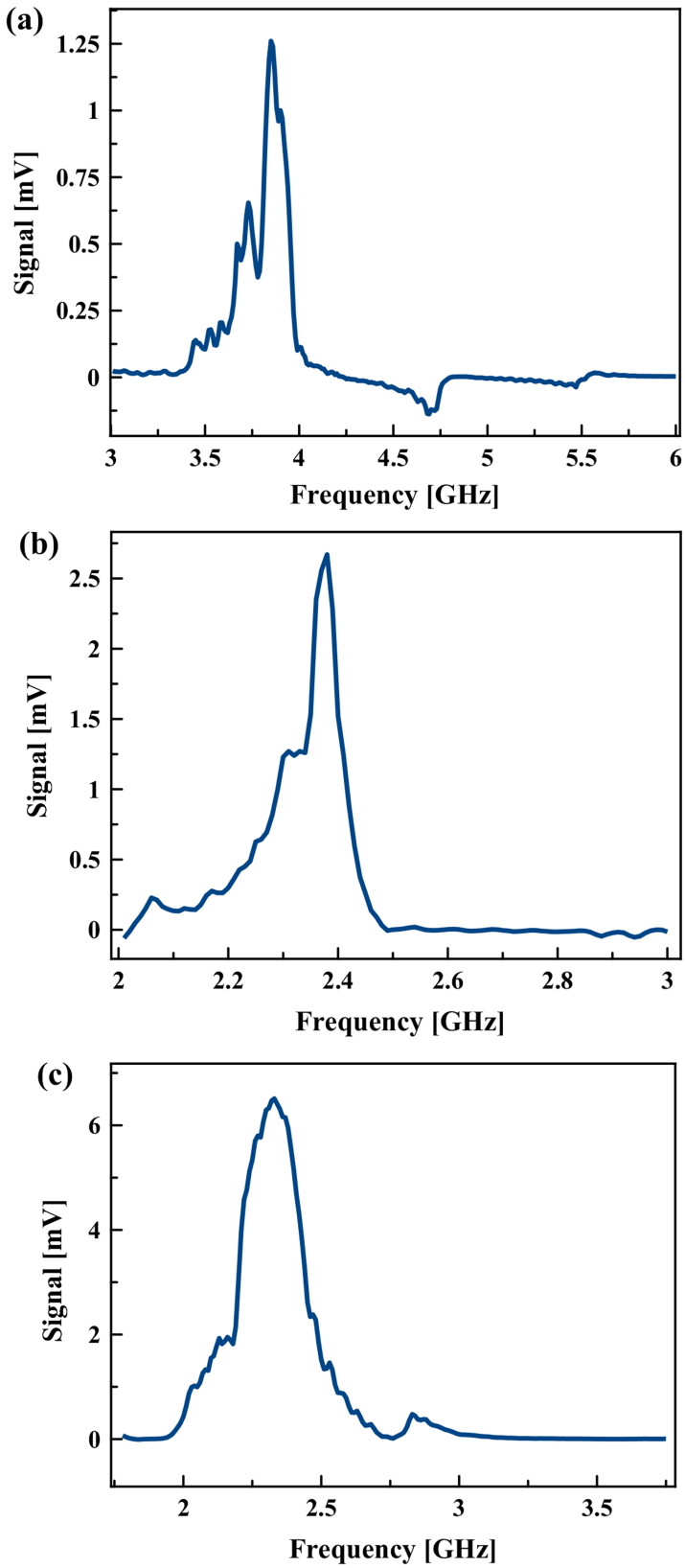

Figure 3.6: Detector response to P = +15 dBm RF power: (a) Response of a type A detector. (b) Response of a type B detector. (c) Response of the best detector, a type B detector.

Next, Fig. 3.6(b) shows the typical response of a type B detector. The output power from signal generator is also 15 dBm. Besides the stronger response of the type B detector, the best resonance is at a lower frequency for this kind of MTJ with a lower in-plane hard axis field of about 200 G, compared to fields at which the best response for type A samples occurs.

Fig. 3.6(c) shows the signal obtained from our best performing sample, which was of type B. As the figure shows, the response of this sample was atypically strong under the same generator output power and magnet position in Fig. 3.6(b), though the resonance frequency was the same as for other type B samples. This best performing sample was larger than the other type B samples tested, measuring 210 nm × 60 nm while the other type B samples measured 150 nm×70 nm. Also, since these tunnel junctions were designed to have equal resistance-area (RA) products regardless of size, the MTJ in the detector of Fig. 3.6(c) has a lower resistance (340 Ω), closer to the impedance of the CPW antenna.

In order to calculate the sensitivity, we show in Fig. 3.7 the response of a type B sensing element ($150 \times 70\,nm^2$) under controlled conditions with the microwave power applied directly to the MTJ via a set of RF cables and a titanium probe. The RF power applied was -36 dBm and the applied field was 150 G along in-plane hard axis. The sensitivity is defined by the formula below:

$$\epsilon = \frac{V}{P_{inc}} \tag{3.8}$$

where V is the output voltage signal, while P_{inc} is the power applied onto the sample. Thus, the detector has a maximal sensitivity of 240 mV/mW when a power of 0.25 μW is applied. This is comparable to the best sensitivity for an MTJ-based detector reported to date[26] under zero bias. It is also on the same order with the sensitivity of the commercial diode we used for calibration, which is quoted as 400 mV/mW.

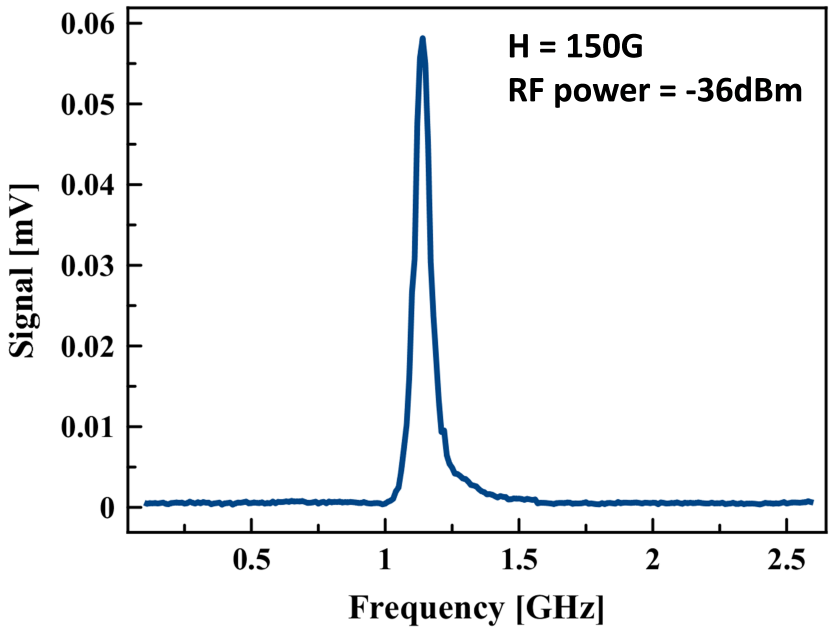

Figure 3.7: Response of a type B MTJ to a direct microwave input at -36 dBm power.

Our detector is also a frequency tunable microwave detector. Fig. 3.8 shows the signal of a type B detector ($210 \times 60\,nm^2$) for radiated microwave signal as a function of applied field along the in-plane hard axis, which is provided by the attached magnet. By adjusting the position of the magnet, the resonance frequency of the detector can be tuned from 0.73 GHz to 1.28 GHz. The detection frequency range is determined by the intrinsic properties of each tunnel junction used for each detector.

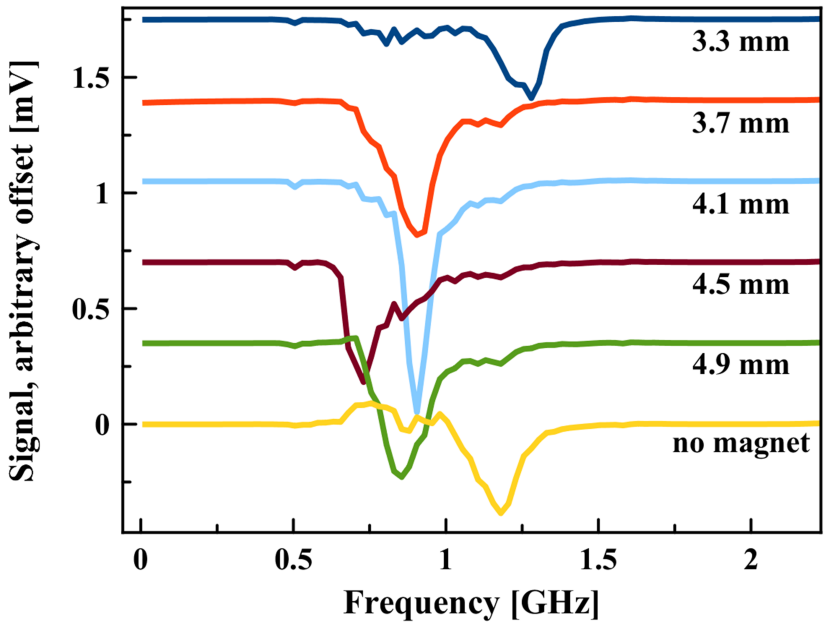

Figure 3.8: Response of a type B detector under different applied field. Labels for each curve represent the distance between the MTJ and the magnet surface which is closer to the MTJ.

Finally, we assembled a detector with two parallel tunnel junctions of different resonance frequency ranges. In this case, we show in fig.3.9 that we can detect microwave signals with two different frequencies at same time, which are around 1 GHz and 2.7 GHz. +15 dBm RF power provided by the microwave generator was delivered to the horn antenna. This type of detector fulfills the multi-range detecting function used to achieve by implementing two separate sensing elements. The resonance frequency can also be tuned by adjusting the inner magnet position, as described in fig. 3.9. The resonance signal around 1 GHz is not as sensitive as the signal around 2.7 GHz. It is possibly due to the coupling between the microwave signals from the MTJ and that transmitted in the rest of the detector circuit. For the application purpose, reliability test on the ESD protection circuit and the mechanical protection (vanish seal on all wire bonds) has also been done as following. First, we applied 1 mA DC currents with different polarities to the input port of the detector, and then tested the detector performance. The results are shown in fig. 3.10. No significant changes in characteristics were found after the ESD test. Second, we dropped the detector from three

feet height after vanishing all the bonded wires. The performance after this mechanical test is given by fig. 3.11. It demonstrates that no damage occurred to either the circuit holder or the detecting function of the detector.

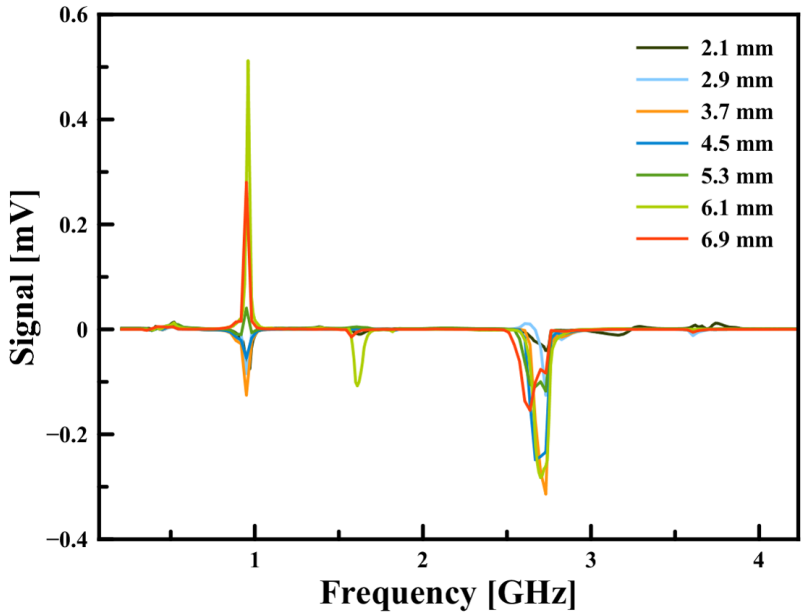

Figure 3.9: Response of a detector assembled with a pair of parallel MTJs (type B with $170 \times 70\,nm^2$ and $170 \times 60\,nm^2$ lateral dimensions) under different applied fields. The detector is placed under a horn antenna connected to a microwave generator, which outputs +15 dBm RF power. Labels for each curve represent the distance between the MTJ array and the magnet surface which is closer to the MTJ array.

3.3 Discussion

To explain why the type B MTJs have a stronger response we can examine Fig. 3.7 and note the asymmetry of the resonance peak. The asymmetric component of the spectrum is a signature of an out-of-plane torque[45]. Such an out-of-plane torque could cause the precession angle of the free layer magnetization to be larger, resulting in both a lower resonant precession frequency and a larger change in resistance which would result in a larger signal. The natural perpendicular-to-plane anisotropy of the type B junctions' free layers can achieve

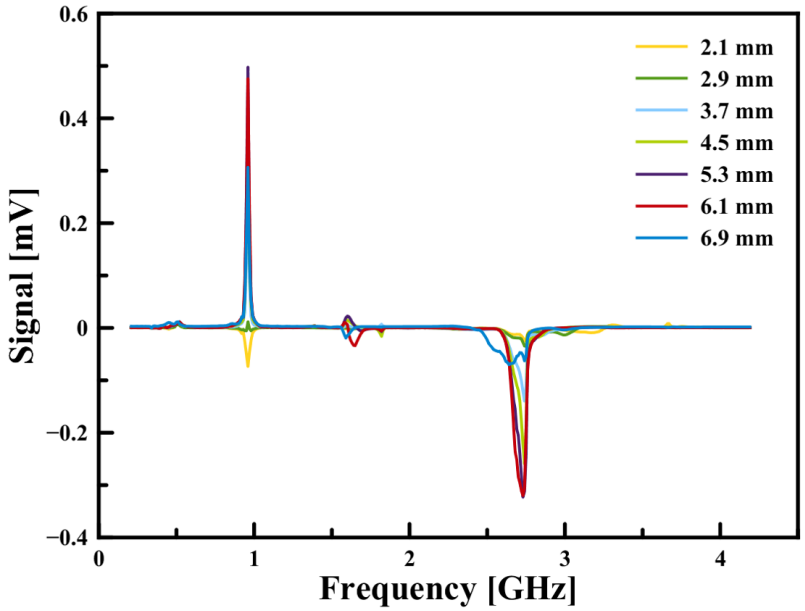

Figure 3.10: Response of the same detector with a pair of parallel MTJs under the exact same condition after ESD protection test. Labels for each curve represent the distance between the MTJ array and the magnet surface which is closer to the MTJ array.

this effect. No such out-of-plane torque was observed in Ref. [45] for a non-biased system with in-plane magnetized free layer, though one is predicted in Ref. [56]. We will explain how this observable out-of-plane torque can arise at zero bias.

ST-FMR spectra obtained for other type B tunnel junction samples at various bias voltages indicate that the antisymmetric component of the peaks is the result of voltage induced magnetic anisotropy [57, 58, 16, 59, 60, 61], which is demonstrated in Ref. [62].

The RF voltage across the tunnel junction due to the oscillating RF current induces change of perpendicular anisotropy, resulting in an additive time-dependent term to $\vec{H}_{eff}$ in the precession term of the Landau-Lifshitz-Gilbert equation for magnetization dynamics:

$$\partial_t \vec{M} = -\gamma_0 \vec{M} \times \vec{H}_{eff} \tag{3.9}$$

We can separate the contribution of voltage induced anisotropy from the rest of the effective

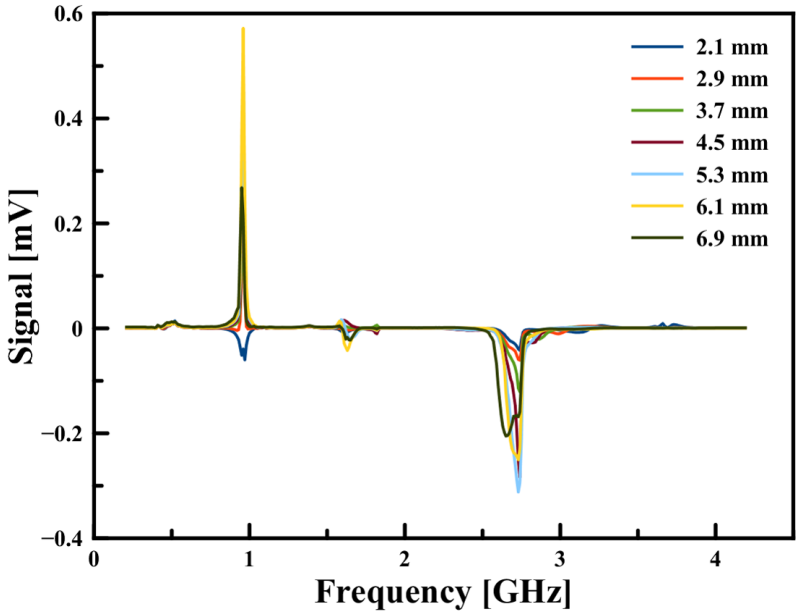

Figure 3.11: Response of the same detector with a pair of parallel MTJs under the exact same condition after vanish sealing and dropping test. Labels for each curve represent the distance between the MTJ array and the magnet surface which is closer to the MTJ array.

field, which we label $\vec{H}^0_{eff}$, giving

$$\partial_t \vec{M} = -\gamma_0(\vec{M} \times \vec{H}^0_{eff} + \vec{M} \times \vec{H}_{via} \sin(2\pi f t) \cos\theta) \tag{3.10}$$

Here, θ is the angle between the magnetizations of the free and pinned layers, and f represents the frequency of RF voltage. The voltage induced contribution to the anisotropy is uniaxial, hence the factor of $\cos\theta = \hat{H}_{via} \cdot \hat{M}$ makes the contribution zero when the sample is magnetized in-plane. Equation (3.10) also shows us that this contribution is zero when the sample is magnetized completely perpendicular to the sample plane. The effect of voltage induced anisotropy is therefore important in MTJs with a significant component of magnetization perpendicular to the layer planes like our type B junctions. This torque due to voltage induced anisotropy change contributes to the antisymmetric part of the ST-FMR spectra. This out-of-plane torque is not field-like spin-torque, but the voltage induced anisotropy torque. Therefore, it appears at zero DC bias and is linear in applied DC bias to the extent

that the out-of-plane anisotropy responds linearly to voltage.

In summary, we have demonstrated a compact, ruggedized, and ESD-protected microwave radiation detector based on magnetic tunnel junctions as sensing elements. Also, we show that the junctions' sensitivity (240 mV/mW) under zero bias approaches that of current commercial semiconductor diode based detectors. In addition, this MTJ-based radiation detector has the feature of being intrinsically frequency tunable by adjusting the position of its magnet. We have also shown that tunnel junctions with free layers partially magnetized out of plane have enhanced sensitivity when compared to junctions with in-plane free layer. This enhancement is due to the voltage induced anisotropy. Furthermore, a more advanced detector based on two parallel MTJs has been demonstrated with the functionality of detecting microwave signals at two different ranges of frequencies. Reliability test on both the ESD and mechanical protection provided good feedback from the response of the detector.

For further improvement of the sensitivity, MTJs with partially perpendicular magnetized free layer are recommended to be implemented as sensing elements in active, dc biased detectors. Therefore, voltage induced anisotropy will play as a greater role and damping can be reduced due to the current induced spin transfer torque[26] in the MTJ device. Besides improvements to the MTJ sensing elements, impedance matching circuits can also be applied to optimize the impedance match between air, antenna, and the sensing element in the detector. Following the suggestions above, a microwave detector with a much larger sensitivity could possibly be achieved in the future.

Chapter 4

Frequency Determination by a pair of Spin-Torque Microwave Detectors

4.1 Introduction

This work was done in collaboration with professor Prokopenko, who proposed the concept of using a pair of MTJ detectors for microwave frequency measurements and performed theoretical analysis. My contribution is experimental realization of the MTJ-based microwave frequency meter and the corresponding data analysis. In typical experiments [19, 20, 23, 26, 63] spin-torque microwave detector (STMD) operates in the dynamic regime, where the spin transfer torque (STT) excites a small-angle magnetization precession about the equilibrium direction of magnetization in the free layer (FL) of an MTJ (description of the other possible non-resonance operation regime of an STMD is not considered in this work and can be found in [27, 64, 24, 13]). In this regime the detector operates as a frequency-selective, quadratic microwave detector with a resonance signal frequency f that is close to the ferromagnetic resonance (FMR) frequency f_{res} of the FL. The rectified dc voltage U_{dc}

generated by an STMD is directly proportional to the input microwave power P_{rf}, while the detector's frequency operation range has an order of the FMR linewidth Γ (here and below specified in frequency units) [19, 20, 23, 26, 63]. This makes an STMD a natural microwave frequency detector at frequencies that are close to the resonance frequency f_{res}. However, such a device has many limitations preventing its wide application in microwave technology: (i) a valid frequency detection by an STMD is only possible for input microwave signals of known power P_{rf} only, (ii) the detection procedure is not completely unambiguous and gives two possible frequency values, (iii) the STMD's frequency detection error Δf is quite large and comparable to the FMR linewidth Γ, which in typical experiments can exceed 100 MHz [19, 20, 23, 27, 65], (iv) the detector's frequency operation range is also limited by the FMR linewidth Γ.

This work introduces a simple and unambiguous method of the determination of a microwave signal frequency. The method is based on the application of two uncoupled STMDs connected in parallel to a microwave signal source and can be easily realized experimentally even for the signals of unknown microwave power. We show theoretically and experimentally that such pair of STMDs can act as a high-efficiency microwave frequency detector having substantially reduced frequency determination error Δf (2–5 times less) and greatly expanded frequency operation range and thereby it may overcome the limitations of the frequency detector based on a single STMD.

4.2 Theory

So far, a single STMD has been applied for determining frequencies of microwave signals. The absolute value of a rectified output dc voltage U_{dc} (neglecting the phase relations between the input microwave signal and magnetization oscillations in the FL) of a resonance-type

quadratic STMD is given by [21, 13, 19]

$$U_{\rm dc} = \varepsilon_{\rm res} P_{\rm rf} \frac{\Gamma^2}{\Gamma^2 + (f - f_{\rm res})^2} \,. \tag{4.1}$$

Here $P_{\rm rf}$ is the input microwave power, $f_{\rm res}$ and Γ are the FMR frequency and FMR linewidth, respectively, and $\varepsilon_{\rm res}$ is the resonance volt-watt sensitivity of an STMD defined as $U_{\rm dc}/P_{\rm rf}$ at $f = f_{\rm res}$. In [21] $\varepsilon_{\rm res}$ is predicted to be approximately 10^4 mV/mW for a passive (no dc bias) STMD, while the best experimental value achieved to date is $\varepsilon_{\rm res} = 630$ mV/mW for a conventional unbiased STMD [26] and $\varepsilon_{\rm res} = 970$ mV/mW for a passive detector based on MTJ having a voltage-controlled interfacial perpendicular magnetic anisotropy of the FL [63]. The resonance volt-watt sensitivity of an STMD can be greatly enhanced by applying a dc bias current to the detector sufficiently large to compensate the natural damping in the FL of an MTJ. Recent experiments show that such dc-biased STMDs may have the resonance volt-watt sensitivity of $\varepsilon_{\rm res} \approx 1.2 \cdot 10^4$ mV/mW [26] and $\varepsilon_{\rm res} \approx 7.4 \cdot 10^4$ mV/mW [63]. These values of the resonance volt-watt sensitivity $\varepsilon_{\rm res}$ of an STMD are comparable to (passive detector) or greater than (dc-biased detector) the volt-watt sensitivity of a semiconductor Schottky diode.

According to Eq. (4.1) the frequency f of an input microwave signal can be determined by measuring the output dc voltage of the detector $U_{\rm dc}$ if the input microwave power $P_{\rm rf}$, the detector's resonance volt-watt sensitivity $\varepsilon_{\rm res}$, its resonance frequency $f_{\rm res}$ and FMR linewidth Γ are known:

$$f = f_{\rm res} \pm \Gamma \sqrt{\frac{\varepsilon_{\rm res} P_{\rm rf} - U_{\rm dc}}{U_{\rm dc}}} \,. \tag{4.2}$$

Typically the last three parameters, $\varepsilon_{\rm res}$, $f_{\rm res}$ and Γ, can be measured experimentally or calculated theoretically for a particular detector prior to the measurement of the input microwave signal frequency f. However, even for the signal of known microwave power $P_{\rm rf}$

and arbitrary frequency $f \neq f_{\mathrm{res}}$ it is impossible to clearly determine the frequency f from the solution (4.2) of the second-order Eq. (4.1) using only *one* measured value – the detector's output dc voltage U_{dc}. Although this problem could be solved by selecting a particular work frequency range of the detector ($f < f_{\mathrm{res}}$ or $f > f_{\mathrm{res}}$) and/or by using an additional low-pass ($f < f_{\mathrm{res}}$) or high-pass ($f > f_{\mathrm{res}}$) microwave filter for input microwave signal subjected to the detector, it also seriously affects the complexity and cost of the entire device. Regardless of whether the microwave filter is used or not, the frequency determination error Δf in this case is significant, because it is comparable to the FMR linewidth Γ that can exceed 100 MHz in typical experiments [19, 20, 23, 27, 65]. In addition, the single STMD method of frequency determination becomes unacceptable if the power P_{rf} of the input microwave signal is unknown.

Here we propose a simple model of the microwave frequency detector consisting of two uncoupled resonance-type quadratic STMDs [13, 19, 20, 23, 26, 63]. In general, we assume that the detectors have different volt-watt sensitivities $\varepsilon_{\mathrm{res},1}$ and $\varepsilon_{\mathrm{res},2}$, the resonance frequencies $f_{\mathrm{res},1}$ and $f_{\mathrm{res},2}$, and the FMR linewidths Γ_1 and Γ_2 (here parameters of the first and second detectors are labeled by indexes 1 and 2, respectively). Considering each STMD as an independent device, the output dc voltages generated by the detectors, $U_{\mathrm{dc},1}$ and $U_{\mathrm{dc},2}$, can be written similarly to Eq. (4.1) as

$$\begin{aligned} U_{\mathrm{dc},1} &= \varepsilon_{\mathrm{res},1} P_{\mathrm{rf},1} \frac{\Gamma_1^2}{\Gamma_1^2 + (f - f_{\mathrm{res},1})^2}\,, \\ U_{\mathrm{dc},2} &= \varepsilon_{\mathrm{res},2} P_{\mathrm{rf},2} \frac{\Gamma_2^2}{\Gamma_2^2 + (f - f_{\mathrm{res},2})^2}\,, \end{aligned} \tag{4.3}$$

where $P_{\mathrm{rf},1}$ and $P_{\mathrm{rf},2}$ are the input microwave powers acting on the first and second detector, respectively. We can assume that the detectors are located quite close to each other (the distance between them should be much smaller than the wavelength of detected microwave signal), but the coupling between the detectors remains negligible. We also assume that the detectors are connected in parallel to a microwave signal source and their microwave

impedances are approximately equal. In this case, the input microwave power applied to each detector is the same: $P_{\mathrm{rf},1} = P_{\mathrm{rf},2} = P_{\mathrm{rf}}$. Using these assumptions, the input microwave powers $P_{\mathrm{rf},1}$ and $P_{\mathrm{rf},2}$ can be eliminated from Eq. (4.3) and the equation for the frequency f of the input microwave signal could be written in the form:

$$f = \frac{\kappa f_{\mathrm{res},1} - f_{\mathrm{res},2} + \sqrt{(\kappa-1)\left(\Gamma_2^2 - \kappa\Gamma_1^2\right) + \kappa\Delta f_{\mathrm{res}}^2}}{\kappa - 1}\,. \tag{4.4}$$

Here, we assume that $f_{\mathrm{res},2} > f_{\mathrm{res},1}$, and introduce a dimensionless variable $\kappa = (U_{\mathrm{dc},1}/U_{\mathrm{dc},2})$ $(\varepsilon_{\mathrm{res},2}/\varepsilon_{\mathrm{res},1})(\Gamma_2/\Gamma_1)^2$, which can be easily calculated for a particular set of detectors and use anzatz $\Delta f_{\mathrm{res}} = f_{\mathrm{res},2} - f_{\mathrm{res},1} > 0$. The presented solution (4.4) is unique in the frequency range $f_{\mathrm{res},1} \le f \le f_{\mathrm{res},2}$ and can be used for the determination of unknown frequency f of the input microwave signal from the measured voltages $U_{\mathrm{dc},1}$, $U_{\mathrm{dc},2}$ and known detector's parameters ($\varepsilon_{\mathrm{res},1}$, $\varepsilon_{\mathrm{res},2}$, $f_{\mathrm{res},1}$, $f_{\mathrm{res},2}$, Γ_1, Γ_2). This solution is valid for the case $\kappa \neq 1$, i.e. when we have detectors with different working parameters. Otherwise, in the case $\kappa = 1$, expression (4.4) transforms to $f = 0.5(f_{\mathrm{res},2} + f_{\mathrm{res},1}) + 0.5(\Gamma_2^2 - \Gamma_1^2)/\Delta f_{\mathrm{res}}$ and becomes almost equivalent to the solution (4.2) for a single STMD.

If we consider the detector's parameters $\varepsilon_{\mathrm{res},1}$, $\varepsilon_{\mathrm{res},2}$, $f_{\mathrm{res},1}$, $f_{\mathrm{res},2}$, Γ_1, Γ_2 as frequency-independent values (at least in the frequency range $f_{\mathrm{res},1} \le f \le f_{\mathrm{res},2}$), the expression for the frequency error Δf can be estimated from Eq. (4.4) as:

$$\begin{aligned}\Delta f = \sqrt{\left(\frac{\partial f}{\partial U_{\mathrm{dc},1}}\right)^2 \Delta U_{\mathrm{dc},1}^2 + \left(\frac{\partial f}{\partial U_{\mathrm{dc},2}}\right)^2 \Delta U_{\mathrm{dc},2}^2} = \\ \frac{\kappa}{2(\kappa-1)^2}\frac{|Q|}{S}\sqrt{\left(\frac{\Delta U_{\mathrm{dc},1}}{U_{\mathrm{dc},1}}\right)^2 + \left(\frac{\Delta U_{\mathrm{dc},2}}{U_{\mathrm{dc},2}}\right)^2}\,.\end{aligned} \tag{4.5}$$

Here $Q = (\kappa-1)(\Gamma_1^2 - \Gamma_2^2) + \Delta f_{\mathrm{res}}[2S - (1+\kappa)\Delta f_{\mathrm{res}}]$, $S = \sqrt{\kappa(\Gamma_1^2 + \Gamma_2^2 + \Delta f_{\mathrm{res}}^2) - \kappa^2\Gamma_1^2 - \Gamma_2^2}$, $\Delta U_{\mathrm{dc},1}$, $\Delta U_{\mathrm{dc},2}$ are the total intrinsic fluctuations of the output dc voltages $U_{\mathrm{dc},1}$, $U_{\mathrm{dc},2}$ (noise voltages), respectively. Depending on the features of a particular experiment voltage fluctu-

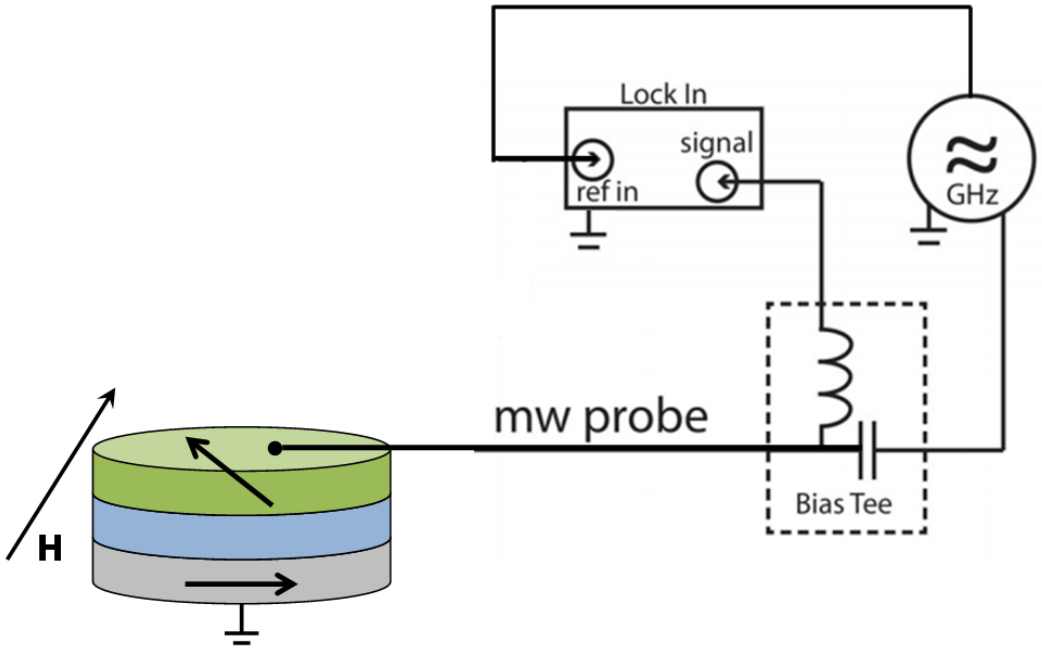

Figure 4.1: Schematic diagram of the amplitude-modulation ST-FMR setup.

ations $\Delta U_{\mathrm{dc},1}$, $\Delta U_{\mathrm{dc},2}$ may have contributions from a thermal noise, shot noise (important for a dc biased STMDs), flicker noise etc. For the most typical case of a passive STMD operating in the presence of a thermal noise the voltage fluctuations $\Delta U_{\mathrm{dc},1}$ and $\Delta U_{\mathrm{dc},2}$ can be calculated from Eq. (3) in Ref. [66] (see also [13] for details).

The equation (4.5) for Δf is complicated and nonlinearly depends on the detectors' parameters. In the discussion section it will be simplified and used for the explanation of our experimental data.

4.3 Experiment

Fig. 4.1 shows the schematic setup of our amplitude-modulated spin torque ferromagnetic resonance

(ST-FMR) [67, 68] measurement of an MTJ based microwave detector. In the experiment, the microwave generator applies a microwave current $I(t)$ to the MTJ via a bias-tee and a microwave probe. The generated STT drives the magnetization precession in the FL of an MTJ, leading to concurrent resistance oscillation $R(t)$ owing to the sample's TMR. The resistance oscillation $R(t)$ then rectifies with the microwave current $I(t)$ and produces a dc voltage $U_{\rm dc}$. By keeping the external magnetic field applied to the MTJs constant and sweeping the microwave drive frequency f, the amplitude of this dc voltage signal $U_{\rm dc}$ changes accordingly and reaches extrema when certain resonant conditions are met. In order to improve the signal-to-noise ratio (SNR), lock-in detection technique was employed. We utilize a pair of uncoupled MTJ detectors as a detector array for precision frequency detection. In order to separately control the resonance frequencies of the two detectors, we can apply different external fields, $B_{\rm dc,1}$ and $B_{\rm dc,2}$ to the first and the second detector, respectively. Detailed description of the used experimental technique can be found in [68].

All MTJs discussed in this paper are of elliptical shape with both free and pined layers in-plane magnetized. The sample stack structure is of the form: Substrate / SAF / MgO / FL / Cap (SAF: synthetic anti-ferromagnetic layer). The compositions of SAF and FL are PtMn(15) / $Co_{70}Fe_{30}$(2.5) / Ru(0.85) / $Co_{40}Fe_{40}B_{20}$(2.4), and $Co_{60}Fe_{20}B_{20}$(1.6 – 3.0), respectively (thicknesses in nanometers). In this paper, we discuss three detector arrays of different FL thicknesses: $l = 3.0$ nm [case (a)], $l = 2.3$ nm [case (b)], and $l = 1.6$ nm [case (c)].

In our experiment, ST-FMR was performed separately on each of the two uncoupled MTJ detectors inside the same detector array. The microwave power $P_{\rm rf}$ was carefully adjusted so that both detectors received nearly equal power. External dc magnetic field was applied

Table 4.1: The FL thicknesses l, applied external fields $B_{\mathrm{dc},1}$, $B_{\mathrm{dc},2}$ and delivered microwave power P_{rf} for the three detector arrays studied in the experiment (see Fig. 4.2)

Case	l, nm	$B_{\mathrm{dc},1}$, G	$B_{\mathrm{dc},2}$, G	P_{rf}, μW
(a)	3.0	-300	-700	1.51
(b)	2.3	-600	700	0.39
(c)	1.6	-900	1000	0.25

along MTJ FL hard axis in order to obtain the optimal volt-watt sensitivity $\varepsilon_{\mathrm{res}}$ [21]. The delivered microwave power P_{rf} and the applied external fields, $B_{\mathrm{dc},1}$ and $B_{\mathrm{dc},2}$, used in the experiment are summarized in table 4.1.

4.4 Results and Discussion

Fig. 4.2 summarizes the FMR measurement results of the three detector arrays: solid lines are the measured FMR curves, while dashed lines are the fitted curves calculated from Eq. (4.1). From these fitted curves we obtain the resonance frequencies $f_{\mathrm{res},1}$ and $f_{\mathrm{res},2}$, FMR linewidths Γ_1 and Γ_2, and the resonance volt-watt sensitivities $\varepsilon_{\mathrm{res},1}$ and $\varepsilon_{\mathrm{res},2}$ for the three sets of detector arrays shown in table 4.2. The insets in Fig. 4.2 represent the discrepancy between the determined frequency f_{det} and real frequency f_{real} (frequency error $\Delta f = |f_{\mathrm{det}} - f_{\mathrm{real}}|$) as a function of the real frequency f_{real}, where f_{det} is calculated from Eq. (4.4) based on the measured frequency-dependent output dc voltages $U_{\mathrm{dc},1}(f_{\mathrm{real}})$, $U_{\mathrm{dc},2}(f_{\mathrm{real}})$ of the detectors and the fitting of the corresponding FMR signals using data from table 4.2.

When the microwave drive frequency falls between the resonances of the two detectors, the determined frequency error Δf is generally smaller than the FMR signal linewidths Γ_1, Γ_2 (Fig. 4.3). In Fig. 4.3 orange, violet and green points show the dependence of the frequency error $\Delta f = |f_{\mathrm{det}} - f_{\mathrm{real}}|$ on the real microwave driven frequency f_{real} for the three mentioned cases of studied detector arrays: (a), (b) and (c), respectively (see table 4.1 for details). The

Table 4.2: The resonance frequencies $f_{\mathrm{res},1}$ and $f_{\mathrm{res},2}$ (in GHz units), FMR linewidths Γ_1 and Γ_2 (in GHz units), and resonance volt-watt sensitivities $\varepsilon_{\mathrm{res},1}$ and $\varepsilon_{\mathrm{res},2}$ (in mV/mW units) calculated from the fitted curves shown in Fig. 4.2 for the three detector arrays studied in the experiment

Case	$f_{\mathrm{res},1}$	$f_{\mathrm{res},2}$	Γ_1	Γ_2	$\varepsilon_{\mathrm{res},1}$	$\varepsilon_{\mathrm{res},2}$
(a)	4.810	6.515	0.199	0.202	5.30	5.97
(b)	4.242	5.813	0.218	0.248	28.20	17.72
(c)	5.419	6.019	0.232	0.148	35.71	59.21

values of Γ_1 and Γ_2 are shown in Fig. 4.3 by horizontal solid and dashed lines, respectively.

To explain the experimental results shown in Figs. 4.2 and 4.3 we make several simplifications of the theoretical model considered in the two STMD model. First, we assume that for both detector's noise voltages, $\Delta U_{\mathrm{dc},1}$, $\Delta U_{\mathrm{dc},2}$ in (4.5), have almost the same values and can be replaced with a single quantity $\Delta U_{\mathrm{dc}} = \Delta U_{\mathrm{dc},1} = \Delta U_{\mathrm{dc},2}$. In general, this is not always the case. For instance, taking into account the existence of a thermal noise only, the noise voltages $\Delta U_{\mathrm{dc},1}$, $\Delta U_{\mathrm{dc},2}$ depend on the output dc voltages $U_{\mathrm{dc},1}$, $U_{\mathrm{dc},2}$ of the STMDs and the driving frequency [66]. On the other hand, in actual experiments there is always coupling between the closely-located detectors that causes a deviation of the detector's output voltages from the value given by Eq. (4.1), so this coupling manifests itself as effective frequency-dependent "coupling noise". Fully accounting this noise is a complicated task and, therefore, we employ a simplified approach in our analysis of the experimental data assuming the noise voltage ΔU_{dc} to be an adjustable parameter. This approximation gives good qualitative agreement between the experimental data (green points in Fig. 4.3) and theoretically calculated curve of Δf from Eq. (4.5) (black dash-dotted line in Fig. 4.3, $\Delta U_{\mathrm{dc}} = 1\,\mu\mathrm{V}$) for the STMDs with closely-located resonance frequencies where one could neglect the frequency dependence of $\Delta U_{\mathrm{dc},1}$ and $\Delta U_{\mathrm{dc},2}$.

As one can see in Fig. 4.3, generally, the frequency error Δf decreases substantially in the range $f_{\mathrm{res},1} + \Gamma_1 \leq f \leq f_{\mathrm{res},2} - \Gamma_2$, while at frequencies f that close to the detector's

resonance frequencies it increases. This behavior can be explained by the effective increase of the SNR in the mentioned frequency range $f_{\mathrm{res},1} + \Gamma_1 \leq f \leq f_{\mathrm{res},2} - \Gamma_2$. In this case both output dc voltages $U_{\mathrm{dc},1}$, $U_{\mathrm{dc},2}$ of the detectors are similar and have values exceeding the voltage fluctuations $\Delta U_{\mathrm{dc},1}$ and $\Delta U_{\mathrm{dc},2}$. Thus, the contribution of the first and the second term under the square root in Eq. (4.5) are almost the same and the values of both terms are substantially less than 1 forcing a small value of the frequency error Δf. In contrast, at signal frequencies f that are very close to one of the detector's resonance frequencies ($f - f_{\mathrm{res},1} < \Gamma_1$ or $f_{\mathrm{res},2} - f < \Gamma_2$) the total SNR ratio of the microwave frequency detector decreases due to the deterioration of optimal work condition for both STMDs. As it follows from Eq. (4.5) (see also black dash-dotted curve in Fig. 4.3), the frequency error Δf increases if $U_{\mathrm{dc},1} \gg U_{\mathrm{dc},2}$ ($f \approx f_{\mathrm{res},1}$) or $U_{\mathrm{dc},1} \ll U_{\mathrm{dc},2}$ ($f \approx f_{\mathrm{res},2}$). This situation is similar to the case of a single detector operating in a frequency range near its resonance frequency, while a signal from the other detector acts like a weak additional noise signal that slightly pushes the first STMD from its optimal working point.

The advantages of the considered microwave frequency detector in the frequency range $f_{\mathrm{res},1} + \Gamma_1 \leq f \leq f_{\mathrm{res},2} - \Gamma_2$, however, disappear when previously introduced dimensionless parameter κ becomes approximately equal to 1 (the case of almost identical detectors) or when one of the detectors's output dc voltages becomes comparable to its noise voltage (so, the SNR becomes approximately equal to 1). For a system of two almost identical detectors (case (a) of the studied detectors arrays, see Fig. 4.2(a) and table 4.2), $\Gamma_1 \approx \Gamma_2$, $\varepsilon_{\mathrm{res},1} \approx \varepsilon_{\mathrm{res},2}$ and κ is close to 1 in almost the whole optimal frequency range $f_{\mathrm{res},1} + \Gamma_1 \leq f \leq f_{\mathrm{res},2} - \Gamma_2$, which leads to the substantial increase in the frequency error Δf and the proposed method of frequency determination becomes too inaccurate (see orange squares in Fig. 4.3). The considered frequency determination method also loses its efficiency when the difference between the resonance frequencies Δf_{res} becomes too large ($\Delta f_{\mathrm{res}} \gg \Gamma_1 + \Gamma_2$) forcing a substantial decrease of the measured output dc voltages at frequencies far from the resonance frequencies of the detectors. In this case, the measured voltages could become comparable to the noise

voltages leading to the considerable decrease of the SNR of the system and the increase of the frequency error. Thus, a high-efficiency microwave frequency detector can be achieved in case of two STMDs having substantially different FMR linewidths and/or resonance volt-watt sensitivities, and closely-located resonance frequencies.

Furthermore, the analysis of data in Fig. 4.3 and numerical calculations based on Eq. (4.5) show that the frequency error decreases as the FL becomes thinner. The frequency error attributed to the enhanced resonance volt-watt sensitivity of an STMD for thinner FLs [21] (see table 4.2) and to the change of the voltage fluctuations $\Delta U_{\mathrm{dc},1}$, $\Delta U_{\mathrm{dc},2}$ (the performance of STMD operating in the presence of a thermal noise is considered in Refs. [66, 13]). As one can see from Fig. 4.3, the frequency determination error Δf reduces approximately by a factor of 3 when the FL thickness l decreases from 3 nm to 1.6 nm. This result can be useful for the development and optimization of high-accuracy microwave frequency detectors.

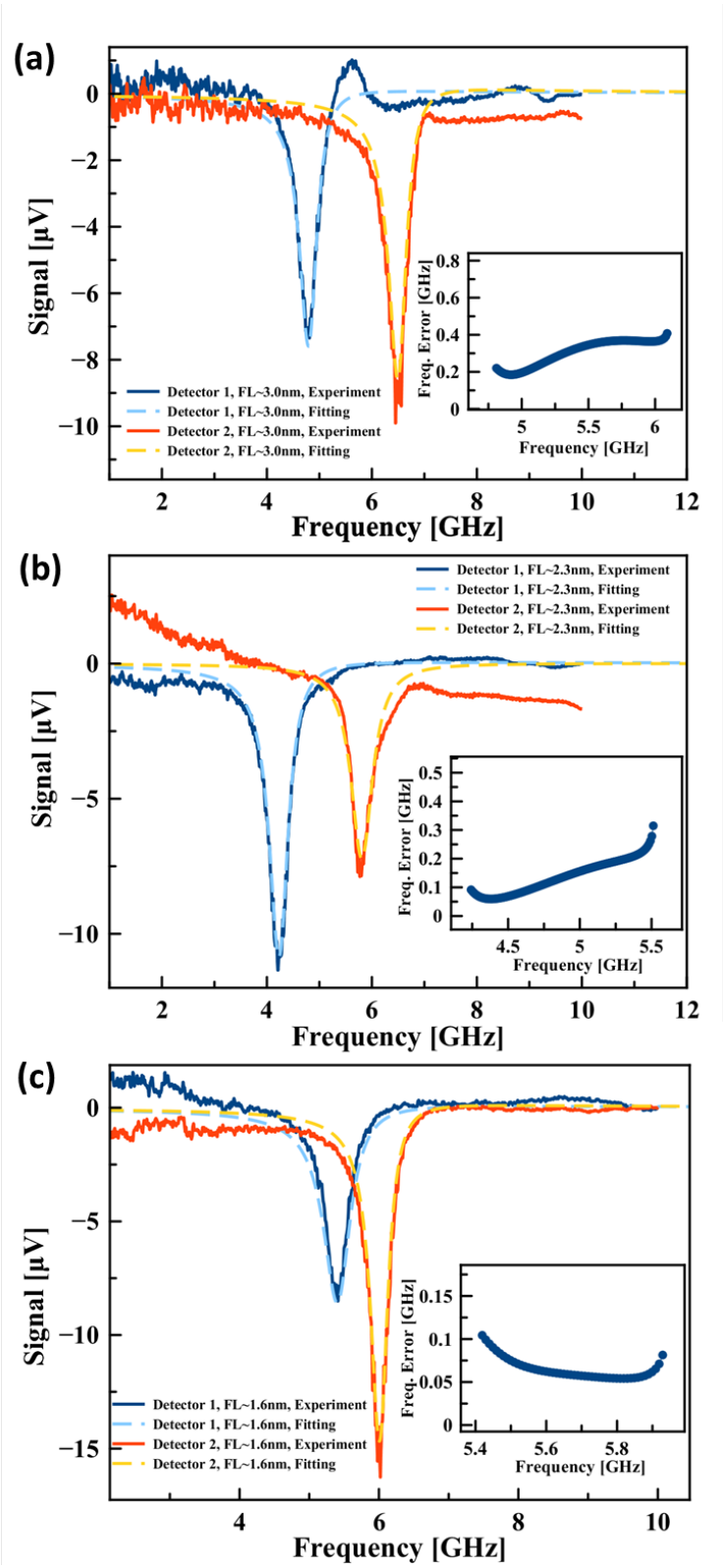

Figure 4.2: Measured FMR signals (solid lines) and fitted curves (dashed lines) versus microwave drive frequency for three sets of detector arrays of different FL thicknesses: (a) $l = 3.0$ nm, (b) $l = 2.3$ nm, and (c) $l = 1.6$ nm. The insets show the determined frequency error Δf as a function of the drive frequency.

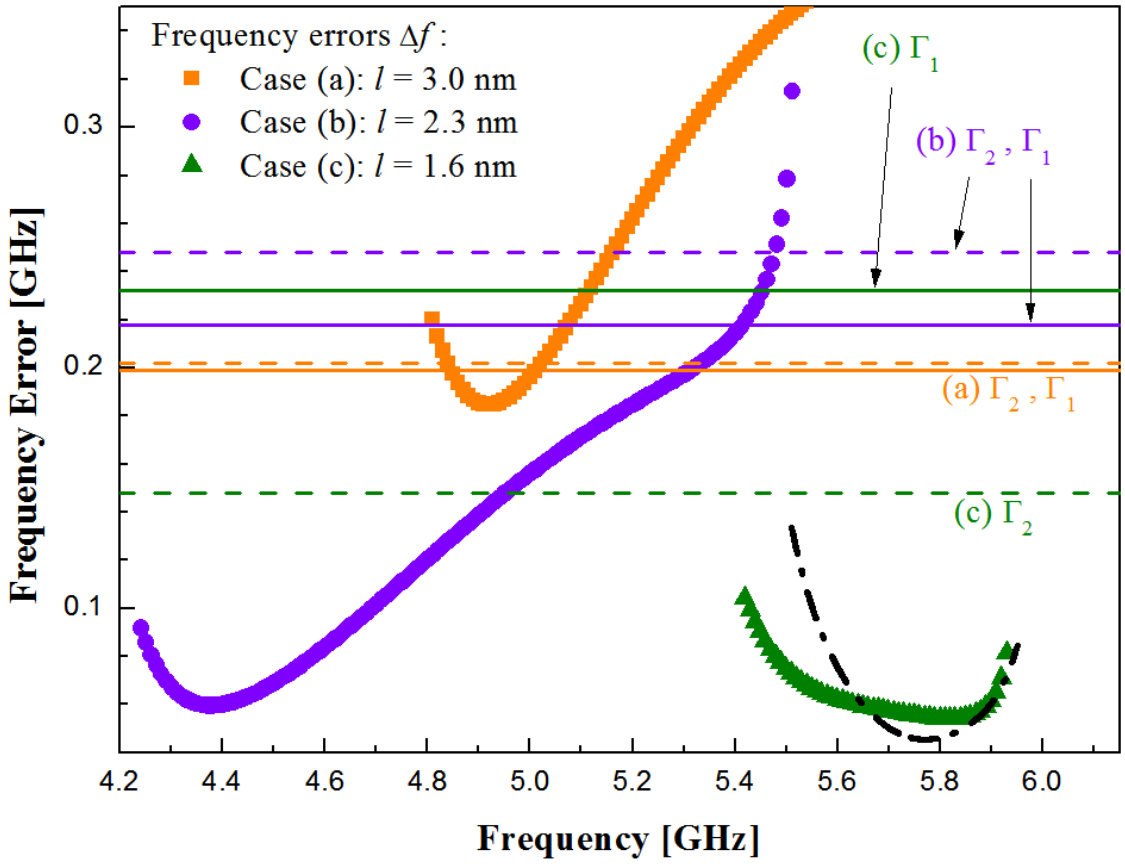

Figure 4.3: Frequency errors $\Delta f = |f_{\rm det} - f_{\rm real}|$ (color points) calculated from the determined frequency $f_{\rm det}$ [given by Eq. (4.4)] and real frequency $f_{\rm real}$ as a function of microwave drive frequency $f_{\rm real}$ for three studied cases of detector arrays: (a) orange squares, (b) violet circles, and (c) green triangles. The values of the detector's FMR linewidths for three detector arrays are indicated by color-coded solid (Γ_1) and dashed (Γ_2) horizontal lines, respectively. Black dash-dotted line is the theoretically calculated dependence Δf from Eq. (4.5) for the third detector array (c).

Chapter 5

Conclusion

This dissertation mainly demonstrated various experimental and computational techniques for observing stochastic, nonlinear magnetization dynamics of the steady auto-oscillatory state far above the critical current. For applying wide range of DC current, instead of MTJs, metallic spin valves have been chosen as our STO in experiment. For our particular sample, we developed a method for obtaining the asymmetry parameter of the angular dependence of GMR based on our bridge measurement of the R-vs-H curve (with extra high accuracy) and a macrospin energy model. We have shown that time-domain measurements of the voltage generated by STO can be processed to rapidly map statistical ensembles of STO magnetization trajectories and thereby determine spin-torque dependent Fokker-Planck effective energy of the STO. Also, a macrospin Fokker-Planck effective energy model has been derived theoretically including the non-linear damping term. The convergence of these two approaches allows for a direct comparison of theoretical and experimental results at the large angle oscillation regime. Therefore, to achieve the best matching with experiment, one can quantitatively determine the nonlinear damping parameters in the theoretical model, which was previously unattainable. We demonstrated that with constant damping in theory, the inter-well separation grows a lot faster than that observed in the experimental effective

energy profiles when the current exceeds the critical. In the meanwhile, with proper nonlinear damping terms, theoretical model can agree with the experimental result qualitatively. Such direct comparison proves the fact that nonlinear damping plays a very important role in the large angle auto-oscillatory dynamics.

Since the macrospin Fokker-Planck theory relies on an uniform distribution of magnetic moments, we may have neglect one discrepancy caused by the micromagnetic effect existing in our sample. So for further improvement, micromagnetic simulation may be helpful since it provides the spatially resolved oscillation trajectories, and therefore may be able to generalize the effective energy Fokker-Planck model to non-uniform magnetized samples.

In the second part of this thesis, we have shown a successful design of a compact, ruggedized, and ESD-protected microwave radiation detector using magnetic tunnel junctions as sensing elements. The detection frequency range of this MTJ-based radiation detector can be tuned via adjusting the magnet installed inside. Besides this additional feature, the detector's sensitivity (240 mV/mW) under zero current bias is comparable with that of current Schottky diode detectors. We have also shown that MTJ samples with larger perpendicular anisotropy of free layers performed with better sensitivity than in-plane MTJs. This improvement is due to the voltage induced anisotropy. To achieve wider range detection function, detectors with two parallel MTJs were assembled, which can detect two different ranges of microwave signals simultaneously. The first-hand experimental results provided robustness and reliability for application purpose.

For further performance enhancement, active dc biased detectors can be considered since i) the voltage induced anisotropy can be more effective and ii) the effective damping can be reduced by the current induced spin transfer torque[26]. In addition to the improvements on the MTJ sensing elements, better impedance matching between the air, the antenna, and the sensing element using a more optimized circuit design will also be helpful. On the other hand, more investigation on the noise properties of these detectors is desired as it is another

crutial factor for further increasing the sensitivity.

In addition, we introduced an effective approach for reducing the error in detecting the frequency of the microwave signal based on two uncoupled STMDs connected in parallel to a microwave signal source. This method is applicable for the signals of unknown microwave power and could determine the frequency with an error substantially smaller than the detector's FMR linewidth. In both theoretical and experimental work, we demonstrated that when the two thin-free-layer STMDs have similar resonance frequencies, but different FMR linewidths and resonance volt-watt sensitivities, the accuracy of microwave frequency detection will be improved compared to a single STMD based detector.

Bibliography

[1] G. E. Rowlands. Stochastic magnetic dynamics in patterned nanostructures. *PhD thesis*, 2012.

[2] D. C. Ralph and M. D. Stiles. Spin transfer torques. *Journal of Magnetism and Magnetic Materials*, 320:1190–1216, 2008.

[3] X. Cheng. Stochastic resonance in magnetic nanostructures. *PhD thesis*, 2011.

[4] A. Slavin and V. Tiberkevich. Nonlinear auto-oscillator theory of microwave generation by spin-polarized current. *IEEE TRANSACTIONS ON MAGNETICS*, 45:4, 2009.

[5] G. E. Rowlands, J. A. Katine, J. Langer, and etc. Time domain mapping of spin torque oscillator effective energy. *PHYSICAL REVIEW LETTERS*, 111:087206, 2013.

[6] J. C. Slonczewski. Conductance and exchange coupling of two ferromagnets separated by a tunneling barrier. *Physical Review B*, 39:6995, 1989.

[7] W. H. Butler, X. G. Zhang, T. C. Schulthess, and etc. Spin-dependent tunneling conductance of fe—mgo—fe sandwiches. *Physical Review B*, 63:054416, 2001.

[8] J. Mathon and A. Umerski. Theory of tunneling magnetoresistance of an epitaxial fe/mgo/fe(001) junction. *Physical Review B*, 63:220403, 2001.

[9] S. P. Parkin, C. Kaiser, A. Panchula, and etc. Giant tunnelling magnetoresistance at room temperature with mgo (100) tunnel barriers. *Nature Materials*, 3:862, 2004.

[10] J. Hayakawa, S. Ikeda, F. Matsukura, and etc. Dependence of giant tunnel magnetoresistance of sputtered cofeb/mgo/cofeb magnetic tunnel junctions on mgo barrier thickness and annealing temperature. *Japanese Journal of Applied Physics*, 44:16, 2005.

[11] H. X. Wei, Q. H. Qin, M. Ma, and etc. 80% tunneling magnetoresistance at room temperature for thin al–o barrier magnetic tunnel junction with cofeb as free and reference layers. *Journal of Applied Physics*, 101:09B501, 2007.

[12] S. Ikeda, J. Hayakawa, Y. Ashizawa, and etc. Tunnel magnetoresistance of 604% at 300k300k by suppression of ta diffusion in cofeb/mgo/cofebcofeb/mgo/cofeb pseudo-spin-valves annealed at high temperature. *Applied Physics Letters*, 93:082508, 2008.

[13] O. V. Prokopenko, I. N. Krivorotov, T. J. Meitzler, E. Bankowski, V. S. Tiberkevich, and A. N. Slavin. Spin-torque microwave detectors. *Magnonics: From Fundamentals to Applications*, 125, 2013.

[14] M. Julliere. Tunneling between ferromagnetic films. *Phys. Lett. A*, 54:225, 1975.

[15] S. Yuasa, T. Nagahama, A. Fukushima, Y. Suzuki, and K. Ando. Giant room-temperature magnetoresistance in single-crystal fe/mgo/fe magnetic tunnel junctions. *Nature Mater.*, 3:868, 2004.

[16] S. Ikeda, K. Miura, H. Yamamoto, K. Mizunuma, H. D. Gan, and etc. A perpendicular-anisotropy cofeb–mgo magnetic tunnel junction. *Nature Mater.*, 9:721, 2010.

[17] J. C. Slonczewski. Current-driven excitation of magnetic multilayers. *J. Magn. Magn. Mater.*, 159, 1996.

[18] L. Berger. Emission of spin waves by a magnetic multilayer traversed by a current. *Phys. Rev. B*, 54:9353, 1996.

[19] A. A. Tulapurkar, Y. Suzuki, A. Fukushima, H. Kubota, H. Maehara, and etc. Spin-torque diode effect in magnetic tunnel junctions. *Nature*, 438:339, 2005.

[20] J. C. Sankey, P. M. Braganca, A. G. F. Garcia, I. N. Krivorotov, R. A. Buhrman, and D. C. Ralph. Spin-transfer-driven ferromagnetic resonance of individual nanomagnets. *Phys. Rev. Lett.*, 96:227601, 2006.

[21] C. Wang, Y. T. Cui, J. Z. Sun, K. Mizunuma, and etc. Sensitivity of spin-torque diodes for frequency-tunable resonant microwave detection. *Journal of Applied Physics*, 106:053905, 2009.

[22] X. Fan, R. Cao, T. Moriyama, and etc. Magnetic tunnel junction based microwave detector. *Applied Physics Letters*, 95:122501, 2009.

[23] S. Ishibashi, T. Seki, T. Nozaki, and etc. Large diode sensitivity of cofeb/mgo/cofeb magnetic tunnel junctions. *Applied Physics Express*, 3:073001, 2010.

[24] O. V. Prokopenko, I. N. Krivorotov, E. Bankowski, and etc. Spin-torque microwave detector with out-of-plane precessing magnetic moment. *Journal of Applied Physics*, 111:123904, 2012.

[25] O. V. Prokopenko and A. N. Slavin. Microwave detectors based on the spin-torque diode effect. *Low Temperature Physics*, 41:353, 2015.

[26] S. Miwa, S. Ishibashi, H. Tomita, and etc. Highly sensitive nanoscale spin-torque diode. *Nature Materials*, 13:3778, 2013.

[27] X. Cheng, C. T. Boone, J. Zhu, and I. N. Krivorotov. Nonadiabatic stochastic resonance of a nanomagnet excited by spin torque. *Phys. Rev. Lett.*, 105:047202, 2010.

[28] M. T. Johnson, P. J. H. Bloemen, F. J. A. den Broeder, and etc. Magnetic anisotropy in metallic multilayers. *Journal of Applied Physics*, 59:11, 1996.

[29] R. L. Stamps, L. Louail, M. Hehn, and etc. Anisotropies, cone states, and stripe domains in co/pt multilayers. *Journal of Applied Physics*, 81:8, 1998.

[30] J. C. Slonczewski. Currents, torques, and polarization factors in magnetic tunnel junctions. *Phys. Rev. B*, 71:1–10, 2005.

[31] G. Binasch and P. Grünberg. Enhanced magnetoresistance in layered magnetic structures with antiferromagnetic interlayer exchange. *Phys. Rev. B*, 39:4828–4830, 1989.

[32] M. Baibich and J. Broto. Giant magnetoresistance of(001) fe/(001) cr magnetic superlattices. *Phys. Rev. Letters*, 61:2472–2475, 1988.

[33] J. Slonczewski. Currents and torques in metallic magnetic multilayers. *Journal of magnetism and magnetic materials*, 247:324–338, 2002.

[34] B. Oliver, Q. He, X. Tang, and J. Nowak. Dielectric breakdown in magnetic tunnel junctions having an ultrathin barrier. *J. Appl. Phys.*, 91:4348, 2002.

[35] J. C. Slonczewski and J. Z. Sun. Theory of voltage-driven current and torque in magnetic tunnel junctions. *J. Magn. Magn. Mater.*, 310:169–175, 2007.

[36] I. Theodonis, N. Kioussis, A. Kalitsov, and etc. Anomalous bias dependence of spin torque in magnetic tunnel junctions. *Phys. Rev. Letters*, 97:237205, 2006.

[37] S. I. Kiselev, J. C. Sankey, I. N. Krivorotov, and etc. Microwave oscillations of a nanomagnet driven by a spin polarized current. *Nature*, 425:380–3, 2003.

[38] W. H. Rippard, M. R. Pufall, S. Kaka, and etc. Direct-current induced dynamics in co90fe10/ni80fe20 point contacts. *Phys. Rev. Letters*, 92:90–93, 2004.

[39] J. A. Katine, F. J. Albert, R. A. Buhrman, and etc. Current driven magnetization reversal and spin-wave excitations in co/cu/co pillars. *Phys. Rev. Letters*, 84:3149–52, 2000.

[40] P. M. Braganca, B. A. Gurney, B. A. Wilson, and etc. Nanoscale magnetic field detection using a spin torque oscillator. *Nanotechnology*, 21:23, 2010.

[41] J. C. Sankey, I. N. Krivorotov, S. I. Kiselev, and etc. Mechanisms limiting the coherence time of spontaneous magnetic oscillations driven by dc spin-polarized currents. *Phys. Rev. B*, 72:224427, 2005.

[42] P. K. Muduli, O. G. Heinonen, and J. Åkerman. Decoherence and mode hopping in a magnetic tunnel junction based spin torque oscillator. *Phys. Rev. Lett.*, 108:207203, 2012.

[43] C. Kittel. On the theory of ferromagnetic resonance absorption. *Physical Review*, 73:155–161, 1948.

[44] B. K. Kuanr, R. E. Camley, Z. Celinski, and etc. Extrinsic contribution to gilbert damping in sputtered nife films by ferromagnetic resonance. *Journal of Magnetism and Magnetic Materials*, 286:276–281, 2005.

[45] J. Sankey and etc. Measurement of the spin-transfer-torque vector in magnetic tunnel junctions. *Nature Physics*, 4:67–71, 2008.

[46] I. N. Krivorotov, N. C. Emley, and J. C. Sankey. Time-domain measurements of nanomagnet dynamics driven by spin-transfer torques. *Science*, 307:5707, 2005.

[47] T. Nagasawa, K. Mizushima, and H. Suto. Amplitude noise in spin-torque oscillators. *Applied Physics Express*, 4:6, 2011.

[48] G. Bertotti, I. Mayergoyz, and C. Serpico. Nonlinear magnetization dynamics in nanosystems. *Elsevier Science*, 9780080443164, 2008.

[49] M. D'Aquino, C. Serpico, G. Miano, and etc. Numerical integration of landau–lifshitz–gilbert equation based on the midpoint rule. *J. Appl. Phys.*, 97:10E319, 2005.

[50] M. D'Aquino, C. Serpico, G. Coppola, and etc. Midpoint numerical technique for stochastic landau-lifshitz-gilbert dynamics. *J. Appl. Phys.*, 99:08B905, 2006.

[51] V. Tiberkevich and A. Slavin. Nonlinear phenomenological model of magnetic dissipation for large precession angles: Generalization of the gilbert model. *PHYSICAL REVIEW B*, 75:014440, 2007.

[52] W. Brown. Thermal fluctuations of a single-domain particle. *Phys. Rev.*, 1963.

[53] D. M. Apalkov and P. B. Visscher. Spin-torque switching: Fokker-planck rate calculation. *PHYSICAL REVIEW B*, 72:180405, 2005.

[54] D. D. Djayaprawira, K. Tsunekawa, M. Nagai, and etc. 230% room-temperature magnetoresistance in cofeb/mgo/cofebcofeb/mgo/cofeb magnetic tunnel junctions. *Applied Physics Letters*, 86:092502, 2005.

[55] R. N. Simons. Coplanar waveguide circuits components systems. *Wiley-IEEE Press*, 2001.

[56] J. Xiao, G. E. W. Bauer, and A. Brataas. Spin-transfer torque in magnetic tunnel junctions: Scattering theory. *Phys. Rev. B*, 77:224419, 2008.

[57] T. Maruyama, Y. Shiota, T. Nozaki, and etc. Large voltage-induced magnetic anisotropy change in a few atomic layers of iron. *Nature Nanotechnology*, 4:158 – 161, 2009.

[58] T. Nozaki, Y. Shiota, M. Shiraishi, and etc. Voltage-induced perpendicular magnetic anisotropy change in magnetic tunnel junctions. *Appl. Phys. Lett.*, 96:022506, 2010.

[59] Y. Shiota, S. Murakami, F. Bonell, and etc. Quantitative evaluation of voltage-induced magnetic anisotropy change by magnetoresistance measurement. *Applied Physics Express*, 4:4, 2011.

[60] H. Kubota, S. Ishibashi, T. Saruya, and etc. Enhancement of perpendicular magnetic anisotropy in feb free layers using a thin mgo cap layer. *J. Appl. Phys.*, 07C723:111, 2012.

[61] K. Yamada, H. Kakizakai, K. Shimamura, and etc. Electric field modulation of magnetic anisotropy in mgo/co/pt structure. *Applied Physics Express*, 6:7, 2013.

[62] J. Zhu, J. A. Katine, G. E. Rowlands, and etc. Voltage-induced ferromagnetic resonance in magnetic tunnel junctions. *Phys. Rev. Lett.*, 108:197203, 2012.

[63] B. Fang, M. Carpentieri, X. Hao, and etc. Giant spin-torque diode sensitivity in the absence of bias magnetic field. *Nature Communications*, 7:11259, 2016.

[64] X. Cheng, J. A. Katine, G. E. Rowlands, and I. N. Krivorotov. Nonlinear ferromagnetic resonance induced by spin torque in nanoscale magnetic tunnel junctions. *Appl. Phys. Lett.*, 103:082402, 2013.

[65] A. G. Gurevich and G. A. Melkov. Magnetization oscillations and waves. *CRC Press, New York*, 1996.

[66] O. Prokopenko, G. Melkov, E. Bankowski, and etc. Noise properties of a resonance-type spin-torque microwave detector. *Appl. Phys. Lett.*, 99:032507, 2011.

[67] C. Wang, Y.-T. Cui, J. A. Katine, and etc. Time-resolved measurement of spin-transfer-driven ferromagnetic resonance and spin torque in magnetic tunnel junctions. *Nature Physics*, 7:496–501, 2011.

[68] A. M. Gonçalves, I. Barsukov, Y.-J. Chen, and etc. Time-resolved measurement of spin-transfer-driven ferromagnetic resonance and spin torque in magnetic tunnel junctions. *Appl. Phys. Lett.*, 103:172406, 2013.

Appendix A

Appendices

A.1 Sliding FFT Angle Mapping for Time Traces for Multi-currents

_____ Sliding FFT Angle Mapping for Time Traces at Multiple Currents _____

```
#!/usr/bin/python
from scipy.interpolate import interp1d
# General libraries
import sys, os, glob, math
import numpy as np
import scipy as sp

def runAnalysis(initial_file, LargeV_file, LargeV_histFile, ampl,
freqlowcut, freqhighcut, P1avg):
```

```
pickupInterval = 10.0e-9
FFTtime = 5e-9                  ## sliding time window
FFTtimestep = 0.025e-9          ## sliding time step
totaltime = 524288*0.025e-9
steps = int((totaltime-FFTtime)/FFTtimestep + 1)
time = np.arange(0, steps*FFTtimestep, FFTtimestep)

for i in range(0,1):
    f = open(initial_file)
    Ravg = float(f.readline().split()[1])
    field = float(f.readline().split()[1])
    current = float(f.readline().split()[1])*0.001 # convert mA to A
    print Ravg, current
    Rext          = 5.0 # from probes, contacts, etc.
    Ravg          = Ravg - Rext
    # Circuit properties
    atten         = -10.0**(-ampl/20.0) # -1 for inverting
    refl          = 50.0/(Ravg + Rext + 50.0)
    attenoverrefl = atten/refl

    deltaR_EA = 0.683
    deltaR_HA = 0.256
    X = 3.05
    if i==0:
        n = int(float(f.readline().split()[1])) # no. of traces
        timestep = float(f.readline().split(')')[1])
```

```
    FFTdatastep = int(FFTtimestep/timestep)
    FFTdata = int(FFTtime/timestep)+1


cols = np.loadtxt(initial_file, unpack = True)
trace = []
phisUp    = []
phisDown  = []
# mark low freq mode in time traces
marker = np.zeros((n,steps))
for j in range(0,n):
    for k in range(0,steps):
        freqdata = 2.0*np.fft.fft(cols[j,(FFTdatastep)*(k):(k)*
        (FFTdatastep)+ FFTdata])/float(FFTdata)
        l1 = int(np.ceil(freqlowcut*FFTtime)) # df = 1/FFTtime
        l2 = int(freqhighcut*FFTtime)
        P1 = np.sum(np.abs(freqdata[l1:l2+1])**2)
        if P1 > P1avg/2:
            marker[j,k] = 1  # keep this data point
        else:
            marker[j,k] = 0
# record beginning and ending index of time domain data
# corresponding to low freq mode, LF means LowFreq,
# mat means matrix
length = int(pickupInterval/timestep)
LF_index_mat = []
for j in range(0,n):
    LF_index = []
```

```
        flag = 0
        for k in range(0,steps-length+1):
            test = np.sum(marker[j,k:k+length])
            if test < length and flag == 1:
                LF_index.append(k+length-1)
                flag = 0
            if test == length and flag == 0 and k == steps-length:
                LF_index.append(k)
                LF_index.append(k+length)
                flag = 1
            elif test == length and flag == 0:
                LF_index.append(k)
                flag = 1
        LF_index_mat.append(LF_index)
        del LF_index
    # Peak selection and angle mapping for qualified time intervals
    for j in range(0,n):
        for k in range(0,len(LF_index_mat[j])-1,2):

            FFT = np.fft.fft(cols[j,LF_index_mat[j][k]:
            LF_index_mat[j][k+1]])
            timelen = float(LF_index_mat[j][k+1]-LF_index_mat[j][k])*
            timestep
            lowcutIndex = int(np.ceil(freqlowcut*timelen))
            highcutIndex = int(freqhighcut*timelen)+1
            # band pass filter the noise
            FFT[0:lowcutIndex] = np.zeros( (lowcutIndex) )
```

```
FFT[highcutIndex:len(FFT)-highcutIndex] =
np.zeros( ((len(FFT)-2*highcutIndex)) )
FFT[len(FFT)-lowcutIndex:] = np.zeros( (lowcutIndex) )
newtimedata = np.fft.ifft(FFT)
newtimedata_cutedge = newtimedata[51:len(newtimedata)-50]
partV = np.real(newtimedata_cutedge)
# interpolation:
partV_time = np.linspace(0,timestep*(len(partV)-1),
len(partV))
#print len(partV_time), len(partV)
partV_inp = np.zeros(len(partV)*10)
partVtime_inp = np.zeros(len(partV)*10)
# interpolate the trace piece by piece (400 data points)\
# and add together, as the interpolation time increases\
# exponentially with the length of data
for i in range(0,len(partV),400):
    if len(partV[i:])<410:
        func = interp1d(partV_time[i:],partV[i:],
        kind = 'cubic')
        partVtime_inp[i*10:] = np.linspace(partV_time[i],
        partV_time[-1], (len(partV[i:]))*10)
        partV_inp[i*10:] = func(partVtime_inp[i*10:])
        break
    else:
        func = interp1d(partV_time[i:i+400],partV[i:i+400],
        kind = 'cubic')
        partVtime_inp[i*10:i*10+4000] =
```

```
                np.linspace(partV_time[i],partV_time[i+399],400*10)
                partV_inp[i*10:i*10+4000] =
                func(partVtime_inp[i*10:i*10+4000])

        # calculate the crossing angle distributions:
        deltaR = (partV_inp*attenoverrefl/current) + deltaR_HA
        # Clip results above the maxmimum and minimum values
        clipping = np.where(deltaR > deltaR_EA)[0]
        if np.alen(clipping)>0:
            print "Number of clipped maxima:",np.alen(clipping)
            for loc in clipping:
                deltaR[loc] = deltaR_EA-0.001

        clipping1 = np.where(deltaR < 0)[0]
        if np.alen(clipping1)>0:
            for loc in clipping1:
                deltaR[loc] = 0.001
        #Calculate phi
        phi =
        np.arccos((deltaR_EA-(2+X)*deltaR)/(deltaR_EA+deltaR*X))
        diffPhi   = np.diff(phi) # Derivative
        crossings = np.where(np.diff(np.sign(diffPhi)))[0]+1
        # Here are the extrema
        avgPhi    = np.mean(phi)
    # Loop over all of these crossings
    # Ignore peaks on the same side of avgPhi unless they are
    # spaced out by some number greater than the factor given below
```

```
        ignore = 0
        # Containers for crossings
        for i in range(0,len(crossings)-8):
            thisCrossing = phi[crossings[i]]
            nextCrossing = phi[crossings[i+1]]
            thisDiff     = thisCrossing - avgPhi
            nextDiff     = nextCrossing - avgPhi
            thisSign     = np.sign(thisDiff)
            nextSign     = np.sign(nextDiff)
            if (ignore > 0):
            # Decrement ignore counter, but ignore this peak
                ignore -= 1
            else:
                if (thisSign==nextSign and
                np.abs((nextDiff-thisDiff)/thisDiff) < 0.2 ):
    # Crossing on the same side, and the change is small
                    ignore = ignore + 1
                elif (deltaR[crossings[i]] < deltaR_EA):
                    if (nextCrossing < thisCrossing):
    # We are low at the next crossing, and are now high
                        phisUp.append(thisCrossing)
                    else:
    # We are high at the next crossing, and are now low
                        phisDown.append(thisCrossing)
        trace.append(partV_inp)
tracesave = np.concatenate(trace)
print "len(trace):", len(trace)
```

```
print "len(tracesave)", len(tracesave)
# Save picked-up LargeV into file
if (LargeV_file!=""):
    outputLargeV = open(LargeV_file,'w')
    np.savetxt(outputLargeV, tracesave[:596000], fmt="%12.6g")
    #np.savetxt(outputLargeV, tracesave, fmt="%12.6g")
    outputLargeV.close()

f.close()

phisAll  = []
phisAll.extend(phisUp)
phisAll.extend(phisDown)

n1, bins1 = np.histogram(phisUp, bins=100, normed=True)
n2, bins2 = np.histogram(phisDown, bins=100, normed=True)
n3, bins3 = np.histogram(phisAll,  bins=100, normed=True)

binCenters1 = np.abs(np.abs(bins1[0:-1] + (bins1[1]-bins1[0])/2.0))
# return every bin's center
binCenters2 = np.abs(np.abs(bins2[0:-1] + (bins2[1]-bins2[0])/2.0))
binCenters3 = np.abs(np.abs(bins3[0:-1] + (bins3[1]-bins3[0])/2.0))
# Store to file
if (LargeV_histFile!=""):
    RAVG = [Ravg + Rext]
    output     = open(LargeV_histFile, 'w')
    outputData = np.transpose(np.array([binCenters1, n1/np.max(n1),
```

```
            binCenters2, n2/np.max(n2), binCenters3, n3/np.max(n3)]))
            np.savetxt(output, outputData, fmt="%12.6g")
            output.close()
        # Clear memory
        del cols
        del trace
        del tracesave
        del phisAll
        del phisDown
        del phisUp
        del LF_index_mat

if __name__=="__main__":
    print "RUNNING"
    path = "directory contains a folder with all time traces files for\
    different currents"
    parameter_file = "a text file contains parameters for multiple\
    currents: current, amplification value, lowcut_frequency,\
    highcut_frequency, average power of quasi-uniform mode"

    info = np.loadtxt(parameter_file)
    filelist = sorted( glob.glob(
    os.path.join(path+"/Timetrace 600G newfile/","*.txt") ) )
    N = len(filelist)
    print "no. of files corresponding to different currents: ", N
    for i in range(0,N):
        filename = filelist[i]
```

```
current = info[i,0]
ampl = info[i,1]
freqlowcut = info[i,2]
freqhighcut = info[i,3]
P1avg = info[i,4]
print filename
print current, ampl, freqlowcut, freqhighcut, P1avg
runAnalysis(filename,
            LargeV_file= path + "/Lowfreq V for
            600G/"+"TimeTraces_HA-600G-"+
        str(current)+"mA_"+str(freqlowcut)+"-"+str(freqhighcut)+
            "_cutedge100_inp10.txt",
            LargeV_histFile=path + "/Lowfreq V for 600G/"+
            "/angle mapping/"
        +"Histo_600G_"+str(current)+"mA_"+
        str(freqlowcut)+"-"+ str(freqhighcut)+
        "_cutedge100_inp10.txt", ampl=ampl,
        freqlowcut=freqlowcut, freqhighcut=freqhighcut,
        P1avg=P1avg)
```

A.2 Mapping distributions between real signals and toy model

_ Mapping between extrema distributions of R(t)(1st harmonic) and φ(t) from toy model _

```
import sys, os, glob, math
import numpy as np
import scipy as sp

p = math.pi
X = 3.05
Phi0 = 1.9968 ## equilibrium position in experiment
dPhi = np.arange(0,0.8,0.01) ## oscillation range
Phi = Phi0 + dPhi
Phi1 = Phi0 - dPhi
Phi_tot = []
Phi_tot.append(Phi)
Phi_tot.append(Phi1)
Phi_tot = np.concatenate(Phi_tot)

parameter_file = "a text file contains parameters for multiple\
currents: current, amplification value, lowcut_frequency,\
highcut_frequency, average power of quasi-uniform mode"
info = np.loadtxt(parameter_file)
i = 8 ## choose the time trace file for a DC current
current = info[i,0]
ampl = info[i,1]
freqlowcut = info[i,2]
freqhighcut = info[i,3]
R_kei = 19.2407 ## Resistance read by keitheley source meter

R_filtered = []
```

```
V_scope = []
n = np.arange(0,500000,1) ## length of time trace
f = 6.3e9 ## oscillation frequency in Hz
dt = 0.025e-9 ## time step corresponding to 40Gs/s sampling rate
timelen = dt*len(n)
df = 1/timelen
lowcutIndex = int(np.ceil(freqlowcut*dt*len(n)))
highcutIndex = int(freqhighcut*dt*len(n))+1

# Record Rt_filtered upcrossings/V_scope downcrossings which
# correspond to +dPhi #
for dPhim in dPhi:
    print dPhim
    Phit = Phi0 + dPhim*np.sin(2*p*f*dt*n)
    Rt = ((1 - np.cos(Phit))/(2 + X + X*np.cos(Phit)))*0.683 +
    13.533 + (14.275 - 14.216)
    FFT = np.fft.fft(Rt)
    FFTfreq = np.fft.fftfreq(len(n),dt)
    FFT[0:lowcutIndex] = np.zeros( (lowcutIndex) )
    FFT[highcutIndex:len(FFT)-highcutIndex] =
    np.zeros(((len(FFT)-2*highcutIndex)) )
    FFT[len(FFT)-lowcutIndex:] = np.zeros( (lowcutIndex) )
    Rt_filtered = np.real(np.fft.ifft(FFT))
    crossingRup = []
    diffR   = np.diff(Rt_filtered) # Derivative
    crossings = np.where(np.diff(np.sign(diffR)))[0]+1
    # Here are the extrema
```

```
avgR    = np.mean(Rt_filtered)
# Loop over all of these crossings
# Ignore peaks on the same side of avgPhi unless they are spaced
# out by some number greater than the factor given below
ignore = 0
# Containers for crossings
for i in range(0,len(crossings)-8):
    thisCrossing = Rt_filtered[crossings[i]]
    nextCrossing = Rt_filtered[crossings[i+1]]
    thisDiff     = thisCrossing - avgR
    nextDiff     = nextCrossing - avgR
    thisSign     = np.sign(thisDiff)
    nextSign     = np.sign(nextDiff)
    if (ignore > 0):
    # Decrement ignore counter, but ignore this peak
        ignore -= 1
    else:
        if (thisSign==nextSign and np.abs((nextDiff-thisDiff)/thisDiff)
            < 0.2 ):
        # Crossing on the same side, and the change is small
            ignore = ignore + 1
        else:
            if (nextCrossing < thisCrossing):
               crossingRup.append(Rt_filtered[crossings[i]])
               #due to the inverting -1
R_filtered.append(np.mean(crossingRup))
del crossingRup
```

```
# record Rt_filtered downcrossings/V_scope upcrossings which
# correspond to -dPhi
for dPhim in dPhi:
    print dPhim
    Phit = Phi0 - dPhim*np.sin(2*p*f*dt*n)
    Rt = ((1 - np.cos(Phit))/(2 + X + X*np.cos(Phit)))*0.683 + 13.533
    + (14.275 - 14.216)
    FFT = np.fft.fft(Rt)
    FFTfreq = np.fft.fftfreq(len(n),dt)
    FFT[0:lowcutIndex] = np.zeros( (lowcutIndex) )
    FFT[highcutIndex:len(FFT)-highcutIndex] = np.zeros(
    ((len(FFT)-2*highcutIndex)) )
    FFT[len(FFT)-lowcutIndex:] = np.zeros( (lowcutIndex) )
    Rt_filtered = np.real(np.fft.ifft(FFT))
    crossingRdown = []
    diffR   = np.diff(Rt_filtered) # Derivative
    crossings = np.where(np.diff(np.sign(diffR)))[0]+1
    # Here are the extrema
    avgR    = np.mean(Rt_filtered)
    ignore = 0
    for i in range(0,len(crossings)-8):
        thisCrossing = Rt_filtered[crossings[i]]
        nextCrossing = Rt_filtered[crossings[i+1]]
        thisDiff     = thisCrossing - avgR
        nextDiff     = nextCrossing - avgR
        thisSign     = np.sign(thisDiff)
        nextSign     = np.sign(nextDiff)
```

```
        if (ignore > 0):
            ignore -= 1
        else:
            if (thisSign==nextSign and np.abs((nextDiff-thisDiff)/thisDiff)
            < 0.2 ):
                ignore = ignore + 1
            else:
                if (nextCrossing > thisCrossing):
                    crossingRdown.append(Rt_filtered[crossings[i]])
    R_filtered.append(np.mean(crossingRdown))
    del crossingRdown
###### record the V_scope/R_filtered vs Phi_tot ######
RPhi_file =  "a file recording the extrema of R_filtered vs extrema of\
Phi in toy model"
if (RPhi_file!=" "):
    output = open(RPhi_file,'w')
    outputdata = np.transpose(np.array([R_filtered,Phi_tot]))
    np.savetxt(output, outputdata, fmt="%12.6g")
    output.close()
```

A.3 Macrospin Simulation with Stochastic Fields

```
import matplotlib.pyplot as plt
from   mpl_toolkits.mplot3d import Axes3D
import numpy as np
import scipy as sp
from   scipy.optimize import fsolve
import sys
import random

############## Parameters ############
# Damping
alpha0 = 0.011
ast = 1.0 #### strength of in-plane spin-torque
P    = 0.224
X = 3.05
N = 50000
print 'total sim steps N: ', N
q1 = 50
q2 = 0
# cutoff freqs for smoothing the time traces of angles
High = 10.0 ### in GHz
#####################################
# Constants in CGS, so watch out for AbAmps and such!
ech   = 1.6022e-20
hbar  = 6.6261e-27 / (2.0*np.pi)
muB   = 9.2740e-21
kB    = 1.3807e-16
g     = 2.1
```

```
gamma = g*muB / hbar
T     = 300.0
# Saturation magnetization
Ms    = 1030.1     ### in emu/cm3
# Geometry in cm
diameter = 90.0e-7
d      = 5.0e-7
area   = np.pi*(diameter/2)**2
vol    = area*d
G = X + 1 ## X is the angular dependence parameter for metallic spin valve
# Demag tensor
Nxx = 0.0523*4.0*np.pi # Easy Axis
Nyy = 0.0523*4.0*np.pi # Short axis of the plane
Nzz = 0.8954*4.0*np.pi # adding perpendicular anistropy
# Dipolar offset field
Hdip   = 430.4
# External Field
Hext      = 600.0
HextTheta = 1.0*np.pi/2.0
HextPhi   = -0.409*np.pi  #### assume mp is along (1,0,0);
## Hext is perpendicular to the exchange bias direction (not same with mp)
hExtX = (Hext*np.sin(HextTheta)*np.cos(HextPhi))/Ms
hExtY = (Hext*np.sin(HextTheta)*np.sin(HextPhi))/Ms
hExtZ =  Hext*np.cos(HextTheta)/Ms
timeUnit   = 1.0/(gamma*Ms)     # characteristic time of the system
dt         = 10e-12/timeUnit    # measured in units of (gamma Ms)^-1
dtSqrt     = np.sqrt(dt)        # For stochastic evolution
```

```
nu          = np.sqrt(alpha0*kB*T/(0.5*vol*Ms*Ms))
# Diffusion at room temperature
#nu = 0.0 # diffusion at zero temperature
# Other
ident = np.diag([1.0,1.0,1.0])
print "Simulation Time:", 10e-12*N

def matrixRep(Y):
# Matrix representation of the cross product. Much faster than np.cross
    return np.array([[0,    -Y[2],  Y[1]],
                     [ Y[2],    0, -Y[0]],
                     [-Y[1], Y[0],    0]])

def heff(Y):
    hd   = -Y*[Nxx, Nyy, Nzz] ## demag field
    hext = [hExtX, hExtY, hExtZ] ## external field
    hdip = [-Hdip/Ms, 0.0, 0.0] ## dipolar field
    return hd + hext + hdip

def hstt(Y):
    return np.array([sttPreSlon*G/(G+1+(G-1)*Y[0]), 0.0, 0.0])

def functional(y, m, nudW):
    c1        = 0.5*(y + m)
    c2        = matrixRep(c1)
    heffMidDt = heff(c1, conservative)*dt
```

```
    hsttMidDt = hstt(c1)*dt
    consVec = np.dot(c2,heff(c1,conservative))
    alpha = alpha0 + alpha0*q1*(np.dot(consVec,consVec))/16/np.pi/np.pi +
            alpha0*q2*((np.dot(consVec,consVec))/16/np.pi/np.pi)**2 +
            alpha0*q3*((np.dot(consVec,consVec))/16/np.pi/np.pi)**3
    alphaCoeff = 1.0/(1.0 + alpha*alpha)
    c3         = ident + alpha*c2
    c4         = alphaCoeff
    return (y - m) + c4*np.dot( c2, np.dot(c3, heffMidDt + nudW) +
            np.dot(c2, hsttMidDt) )

def midpointEvolve(mx, my, mz):
    nudW  = np.random.randn(3)*nu*dtSqrt
    # Weiner process, incorporating nu
    Ynew  = fsolve(functional, [mx,my,mz], args=([mx,my,mz], nudW),
    xtol=1.0e-13)  ## fsolve(func,x0,args,xtol); x0: ndarray,
    ## starting estimate for roots of func(x)=0; args: func(x,*args),
    ## doesn't include the first variable x.
    return Ynew

def run(arg):
    # Seed the generator with uneccesary randomness
    np.random.seed(random.randint(0,123129))
    # Starting parameters Theta and Phi are with respect to mp(1,0,0)
    # direction
    startTheta = 90.0*np.pi/180.0
    startPhi   = -110*np.pi/180.0
```

```
    # Cartesian coords
    mxs         = [np.sin(startTheta)*np.cos(startPhi)]
    mys         = [np.sin(startTheta)*np.sin(startPhi)]
    mzs         = [np.cos(startTheta)]
    times       = [0.0]
    print 'starting point: ', [mxs,mys,mzs]
    for n in xrange(0,N):
        mx, my, mz = midpointEvolve(mxs[n], mys[n], mzs[n])
        mxs.append(mx)
        mys.append(my)
        mzs.append(mz)
        times.append(n*dt*timeUnit)
    print "Finished #:",arg
    return [mxs,mys,mzs,times]

if __name__ == '__main__':
    # Only the main thread runs here...
    print "Time Step: ", dt*timeUnit
    Ilist = np.arange(1.9, 4.0, 0.2)
    for I in Ilist:
        I    = float(I)*1.0e-3 #in mA
        ### leaving out the angular dependence of ST part
        sttPreSlon = ast*(hbar*P*I)/(2.0*ech*Ms*Ms*vol)
        print "current: ", I

        results = run(1)
        m = 0  ###### 0: mx; 1: my; 2: mz
```

```
begin    = int(np.floor(len(results[m])/10))
end      = int(np.floor(len(results[m])))
#### Mapping the Max and Min of angles between mp and mf
trimmedX  = np.asarray(results[0][begin:end])
trimmedY  = np.asarray(results[1][begin:end])
trimmedZ  = np.asarray(results[2][begin:end])
Phi = np.arccos(trimmedX/np.sqrt(trimmedX**2+trimmedY**2+
trimmedZ**2))
## smooth trace of Phi: filtering out higher order harmonics
## in freq domain
tottime = dt*timeUnit*len(Phi)
print 'tottime: ', tottime
cutoffHigh  = int(np.ceil(High*10**9/(1.0/tottime)))# np.ceil(f/df)
print 'cutoffHigh: ', cutoffHigh
FFT = np.fft.fft(Phi)
FFT[cutoffHigh:len(FFT)-cutoffHigh] =
np.zeros( ((len(FFT)-2*cutoffHigh)) )
newPhi = np.fft.ifft(FFT)
newPhi_cutedge = newPhi[141:len(newPhi)-140]# eliminate 7 osc
# periods at both the beginning and end of smoothed time trace
smoothPhi = np.real(newPhi_cutedge)
print 'len of smoothPhi:', len(smoothPhi)
diffPhi = np.diff(smoothPhi)
extremes = np.where(np.diff(np.sign(diffPhi)))[0]+1
print 'no. of extremes:', len(extremes)
avgPhi    = np.mean(smoothPhi)
phisHigh  = []
```

```
    phisLow   = []
    phisAll   = []
    ignore = 0
    for i in range(0,len(extremes)-8):
        thisExtreme = smoothPhi[extremes[i]]
        nextExtreme = smoothPhi[extremes[i+1]]
        thisDiff     = thisExtreme - avgPhi
        nextDiff     = nextExtreme - avgPhi
        thisSign     = np.sign(thisDiff)
        nextSign     = np.sign(nextDiff)

        if thisSign==nextSign:
            ignore = ignore + 1
        else:
            phisAll.append(thisExtreme*180/np.pi)
            if (thisExtreme < nextExtreme):
                phisLow.append(thisExtreme*180/np.pi)
            else:
                phisHigh.append(thisExtreme*180/np.pi)

    print 'len of phisHigh: ', len(phisHigh)
    print 'len of phisLow: ', len(phisLow)
## ----------- Hist of crossing Phis ----------- ##
fig2 = plt.figure(figsize=(8,8))
ax2 = fig2.add_subplot(111)
#ax2.set_xlim((60,180))
ax2.set_xlim((min(phisLow),max(phisHigh)))
```

```
ax2.hist(phisHigh,50,normed=True)
ax2.hist(phisLow,50,normed=True,alpha=0.5)
fft = np.fft.fft(results[m][begin:end])
spectrum = np.abs(fft)
freqs = np.fft.fftfreq(len(results[m][begin:end]),
d=results[3][begin]-results[3][begin-1])

# plot Mx trace
fig3 = plt.figure(figsize=(8,8))
ax3 = fig3.add_subplot(111)
ax3.plot(dt*timeUnit*np.array(range(0,len(results[m]))),results[m][:])
# plot mx vs mz
fig5 = plt.figure(figsize=(8,8))
ax5 = fig5.add_subplot(111)
ax5.plot(results[m][:],results[m+2][:])
# plot spectrum
fig4 = plt.figure(figsize=(8,8))
ax4 = fig4.add_subplot(111)
ax4.plot(freqs[0:int(0.25*len(freqs))],
spectrum[0:int(0.25*len(freqs))])
# Plot the 3D trajectory
fig1 = plt.figure(figsize=(8,8))
ax1 = Axes3D(fig1)
ax1.set_xlabel('X')
ax1.set_ylabel('Y')
ax1.set_zlabel('Z')
ax1.set_xlim(-1.05,1.05)
```

```
ax1.set_ylim(-1.05,1.05)
ax1.scatter([1.05],[0],[0],color='black',marker='o')
ax1.scatter([-1.05],[0],[0],color='black',marker='o')
ax1.scatter([0],[0],[1.05],color='b',marker='x')
ax1.scatter([0],[0],[-1.05],color='b',marker='x')
ax1.plot(results[0][:], results[1][:], results[2][:])
ax1.scatter([results[0][0]],[results[1][0]],[results[2][0]],color='g',
marker='o', s=80) # Starting Point
ax1.scatter([np.sin(HextTheta)*np.cos(HextPhi)],
[np.sin(HextTheta)*np.sin(HextPhi)],[np.cos(HextTheta)],
color='r',marker='o', s=80) # Hext initial point
plt.show()

del phisHigh
del phisLow
del phisAll
```

A.4 Derivation of E_{eff} via Fokker-Planck Approach

The basic foundation is the LL equation as following:

$$\dot{\vec{M}}_{det} = -\gamma \vec{M} \times \vec{H}_{cons} - \gamma \alpha M_s \cdot \hat{m} \times (\hat{m} \times \vec{H}_{cons}) - \gamma J \beta(\varphi) M_s \cdot \hat{m} \times (\hat{m} \times \hat{m}_p) \quad \text{(A.1)}$$

φ is the angle between free and pin layer's magnetization;$\vec{H}_{cons}$ is the component of $\vec{H}_{eff}$

which is perpendicular to $\hat{m}$:

$$\vec{H}_{cons} = -\hat{m} \times \ (\hat{m} \times \vec{H}_{eff}) \tag{A.2}$$

The current $j(\vec{M}, t)$ is the rate at which systems cross the length element $d\vec{M}$. The total crossing rate from lower to higher E is an integral over the orbit:

$$j^E(E, t) = \oint [j(\vec{M}, t) \times d\vec{M}] \cdot \hat{m} \tag{A.3}$$

The probability current j along the sphere has a convective and a diffusive part: (both the divergence and gradient are two dimentional)

$$j(\vec{M}, t) \equiv \rho(\vec{M}, t)\dot{\vec{M}}_{det}(\vec{M}) - D\nabla\rho(\vec{M}, t) \tag{A.4}$$

So we obtain:

$$j^E(E, t) = \oint [\rho(\vec{M}, t)\dot{\vec{M}}_{det}(\vec{M}) \times d\vec{M}] \cdot \hat{m} - \oint [D\nabla\rho(\vec{M}, t) \times d\vec{M}] \cdot \hat{m} \tag{A.5}$$

The conservative torque in the LLG equation (1) is along $d\vec{M}$ and does not contribute to j^E. So the energy current includes three terms:

$$j^E(E, t) = j^E_{LL}(E, t) + j^E_{Slon}(E, t) + j^E_{diff}(E, t) \tag{A.6}$$

The first(Landau-Lifshitz damping) term comes from the Landau-Lifshitz damping torque:

$$j^E_{LL}(E, t) = -\oint [\rho(\vec{M}, t) \cdot \gamma\alpha M_s \cdot \hat{m} \times (\hat{m} \times \vec{H}_{cons}) \times d\vec{M}] \cdot \hat{m} = -\gamma M_s \rho(E, t) I^E(E) \tag{A.7}$$

$$I^E(E) \equiv \oint \alpha[d\vec{M} \times \vec{H}_{cons}] \cdot \hat{m} = \oint \alpha H_{cons} dM \tag{A.8}$$

Consider the nonlinear damping term:

$$\alpha = \alpha_G + \alpha_G q_1 \xi + ...; \xi = \frac{\left|[\vec{H}_{eff} \times \vec{M}]\right|^2}{16\pi^2 M_s^4} \tag{A.9}$$

Thus

$$I^E(E) = \oint \alpha_G H_{cons} dM + \oint \alpha_G q_1 \xi H_{cons} dM = \alpha_G I_1^E(E) + \alpha_G q_1 I_2^E(E) \tag{A.10}$$

$$I_1^E(E) = \oint H_{cons} dM; I_2^E(E) = \oint \xi H_{cons} dM \tag{A.11}$$

The Slonczewski torque can be expressed here:

$$\dot{\vec{M}}_{Slon} = -\gamma J M_s \beta(\varphi) \hat{m} \times (\hat{m} \times \hat{m}_p) = -\gamma J M_s \beta(\varphi)[\hat{m}(\hat{m} \cdot \hat{m}_p) - \hat{m}_p] \tag{A.12}$$

The energy current contributed from the Slonczewski torque is

$$\begin{aligned} j_{Slon}^E(E,t) &= \oint [\rho(\vec{M},t) \dot{\vec{M}}_{Slon} \times d\vec{M}] \cdot \hat{m} && \text{(A.13)} \\ &= -\gamma J M_s \oint [\rho(\vec{M},t)\beta(\varphi)[\hat{m}(\hat{m} \cdot \hat{m}_p) - \hat{m}_p] \times d\vec{M}] \cdot \hat{m} && \text{(A.14)} \\ &= \gamma J \rho(E,t) \hat{m}_p \oint \beta(\varphi)[d\vec{M} \times \vec{M}] && \text{(A.15)} \end{aligned}$$

$$\beta(\varphi) = \frac{P(\chi+1)}{\chi(\cos\varphi+1)+2} \tag{A.16}$$

We define:

$$I^M(E) = \oint \beta(\varphi)[d\vec{M} \times \vec{M}] \tag{A.17}$$

So the Slonczewski energy current can be expressed below:

$$j^E_{Slon}(E,t) = \gamma J \rho(E,t) \hat{m}_p \cdot I^M(E) \tag{A.18}$$

The diffusive term in (4) involves

$$\nabla\rho(\vec{M},t) = \nabla\rho'(E(\vec{M}),t) = \frac{\partial\rho'(E,t)}{\partial E}\nabla E(\vec{M}) = -\frac{\partial\rho'(E,t)}{\partial E}\vec{H}_{cons} \tag{A.19}$$

According to the fluctuation-dissipation theorem, the diffusivity D can be expressed as:

$$D = \gamma M_s \alpha k_B T/V; D_0 = \gamma M_s \alpha_G k_B T/V; \alpha = \alpha_G + \alpha_G q_1 \xi \tag{A.20}$$

and gives the diffusive energy current as

$$
\begin{aligned}
j^E_{diff}(E,t) &= \frac{\partial \rho'(E,t)}{\partial E} \oint [D \cdot \vec{H}_{cons} \times d\vec{M}] \cdot \hat{m} && \text{(A.21)} \\
&= -\frac{\partial \rho'(E,t)}{\partial E} D_0 \cdot \oint (1 + q_1 \xi)[d\vec{M} \times \vec{H}_{cons}] \cdot \hat{m} && \text{(A.22)} \\
&= -\frac{\partial \rho'(E,t)}{\partial E} D_0 I^E_1(E) - \frac{\partial \rho'(E,t)}{\partial E} D_0 q_1 I^E_2(E) && \text{(A.23)} \\
&= -\frac{\partial \rho'(E,t)}{\partial E} \frac{D_0}{\alpha_G} \cdot I^E(E) && \text{(A.24)}
\end{aligned}
$$

Thus, the total energy current is

$$
\begin{aligned}
j^E(E,t) =& j^E_{LL} + j^E_{slon} + j^E_{diff} \\
=& -\gamma M_s \rho(E,t) I^E(E) + \gamma J \rho(E,t) \hat{m}_p \cdot I^M(E) - \frac{D_0}{\alpha_G} \cdot \frac{\partial \rho'(E,t)}{\partial E} I^E(E)
\end{aligned} \qquad \text{(A.25)}
$$

In the steady state, $j^E(E,t) = 0$, so that

$$
\begin{aligned}
\frac{\partial \ln \rho'(E,t)}{\partial E} &= \frac{\gamma \alpha_G}{D_0}(-M_s + J \cdot \eta(E)) && \text{(A.26)} \\
\eta(E) &= \frac{\hat{m}_p \cdot I^M(E)}{I^E(E)} && \text{(A.27)}
\end{aligned}
$$

So that after integrate (28), we have

$$
\begin{aligned}
\rho'(E,t) &= \rho'(E_0,t) exp(-\frac{V E_{eff}}{k_B T}) && \text{(A.28)} \\
E_{eff} &= \int_{E_0}^{E} (1 - \frac{J}{M_s} \eta(E)) dE && \text{(A.29)}
\end{aligned}
$$

So finally,

$$E_{eff} = E - E_0 - \frac{J}{M_s \alpha_G} \int_{E_0}^{E} \alpha_G \eta(E) dE \tag{A.30}$$

A.5 E_{eff} calculation via Fokker-Planck Approach

```
# General libraries
import sys, os, glob, math
import numpy as np
import scipy as sp

# J here equals to J/Ms/alphaG in the Eeff expression,
# represents a constant
Jlist = np.arange(0.0065,0.011,0.0005)
alpha0 = 0.011 # linear damping value alpha_G
q1 = 0
q2 = 0
print 'q1=',q1
print 'q2=',q2
p = math.pi
X = 3.05
H = 600     #### external field along HA
Hdip = 430.4
Ms_4p = 12938 ### Units in CGS (here this one is in Gauss)
Nz = 0.8954
```

```
Nx = 0.0523

Ny = 0.0523

C = 0.5*Ms_4p*(Nz-Nx)

P = 0.224


ns = 100  # integration steps along each trajectory

PHI = np.linspace(1.9968,1.9968+3.14,501)

# PHI is in-plane crossing angle, each corresponds

# to a conservative trajectory

PHI2 = np.linspace(1.9968-3.14,1.9968,501)


En = Hdip*np.cos(PHI)-H*np.cos(PHI-0.409*p)

En2 = Hdip*np.cos(PHI2)-H*np.cos(PHI2-0.409*p)

Im = []

Ie = []

Id = []


## Coordinate : mp along (1,0,0)  ##

for i in range(1,len(En)):

   trajphi = []

   trajtheta_up = []

   trajtheta_down = []

   phi = np.linspace(PHI[i],PHI[i]-2*(PHI[i]-PHI[0]),ns+1)

   #### in-plane angle steps for each conservative trajectory

   for j in range(0,ns+1):

        A = -H*np.cos(phi[j]-0.409*p)

        B = Hdip*np.cos(phi[j])
```

```
    x = (A+B+np.sqrt((A+B)*(A+B)-4*C*En[i]+4*C*C))/(2*C)
    thetaup = np.arcsin(x)
    thetadown = p-np.arcsin(x)
    trajphi.append(phi[j])
    trajtheta_up.append(thetaup)
    ## out of plane angle step corresponds to each in-plane angle
    for one conservative trajectory
    trajtheta_down.append(thetadown)
xup = np.sin(trajtheta_up)*np.cos(trajphi)
## Here assume polarizer P is along (1,0,0)
yup = np.sin(trajtheta_up)*np.sin(trajphi)
zup = np.cos(trajtheta_up)
xdown = np.sin(trajtheta_down)*np.cos(trajphi)
ydown = np.sin(trajtheta_down)*np.sin(trajphi)
zdown = np.cos(trajtheta_down)

Imdown = 0
Iedown = 0
Iddown = 0
Imup = 0
Ieup = 0
Idup = 0
s = len(trajphi)
## integrate over the trajectory ##
for j in range(0,s-1):
    M1 = np.array([xup[j],yup[j],zup[j]])
    M2 = np.array([xup[j+1],yup[j+1],zup[j+1]])
```

```
        dM = M2-M1
        ## Here the polarizer P is assumed to be along (1,0,0) ##
        Heff = np.array([(H/Ms_4p)*np.cos(0.409*p),(H/Ms_4p)*
        np.sin(0.409*p),0])+ np.array([-Hdip/Ms_4p,0,0])+
        np.array([-Nx*xup[j],-Ny*yup[j],-Nz*zup[j]])
        Hcons = -np.cross(M1,np.cross(M1,Heff))
        ## Heff normalized by Ms_4p
        #### nonlinear damping variable alpha
        eta = np.dot(np.cross(Heff,M1),np.cross(Heff,M1))
        alpha = alpha0 + alpha0*q1*eta + alpha0*q2*eta**2
        #### angular dependence of ST parameter b
        cosphi = np.dot(M1,np.array([1,0,0]))
        b = (X+1)*P/(X*cosphi+X+2)
        Imup = Imup +
        (b/(1+alpha**2))*np.dot(np.cross(dM,M1),np.array([1,0,0]))
        Ieup = Ieup + (alpha/(1+alpha**2))*np.dot(np.cross(dM,Hcons),M1)
        Idup = Idup + alpha*np.dot(np.cross(dM,Hcons),M1)

    for j in range(1,s):
        M1 = np.array([xdown[s-j],ydown[s-j],zdown[s-j]])
        M2 = np.array([xdown[s-j-1],ydown[s-j-1],zdown[s-j-1]])
        dM = M2-M1
        Heff = np.array([(H/Ms_4p)*np.cos(0.409*p),
        (H/Ms_4p)*np.sin(0.409*p),0])+ np.array([-Hdip/Ms_4p,0,0])+
        np.array([-Nx*xdown[s-j],-Ny*ydown[s-j], -Nz*zdown[s-j]])
        Hcons = -np.cross(M1,np.cross(M1,Heff))
        #### nonlinear damping variable alpha
```

```
    eta = np.dot(np.cross(Heff,M1),np.cross(Heff,M1))
    alpha = alpha0 + alpha0*q1*eta + alpha0*q2*eta**2
    #### angular dependence of ST parameter b
    cosphi = np.dot(M1,np.array([1,0,0]))
    b = (X+1)*P/(X*cosphi+X+2)
    Imdown = Imdown +
    (b/(1+alpha**2))*np.dot(np.cross(dM,M1),np.array([1,0,0]))
    Iedown = Iedown + (alpha/(1+alpha**2))*np.dot(np.cross(dM,Hcons),M1)
    Iddown = Iddown + alpha*np.dot(np.cross(dM,Hcons),M1)

M1 = np.array([xup[-1],yup[-1],zup[-1]])
M2 = np.array([xdown[-1],ydown[-1],zdown[-1]])
dM = M2-M1
Heff = np.array([(H/Ms_4p)*np.cos(0.409*p),(H/Ms_4p)*
np.sin(0.409*p),0])+np.array([-Hdip/Ms_4p,0,0])+np.array(
[-Nx*xup[-1],-Ny*yup[-1],-Nz*zup[-1]])
Hcons = -np.cross(M1,np.cross(M1,Heff))
#### nonlinear damping variable alpha
eta = np.dot(np.cross(Heff,M1),np.cross(Heff,M1))
alpha = alpha0 + alpha0*q1*eta + alpha0*q2*eta**2
#### angular dependence of ST parameter b
cosphi = np.dot(M1,np.array([1,0,0]))
b = (X+1)*P/(X*cosphi+X+2)
Imtot = Imup + Imdown +
(b/(1+alpha**2))*np.dot(np.cross(dM,M1),np.array([1,0,0]))
Ietot = Ieup + Iedown + (alpha/(1+alpha**2))*
np.dot(np.cross(dM,Hcons),M1)
```

```
    Idtot = Idup + Iddown + alpha*np.dot(np.cross(dM,Hcons),M1)
    Im.append(Imtot)
    Ie.append(Ietot)
    Id.append(Idtot)
    del trajphi
    del trajtheta_up
    del trajtheta_down

Im = np.array(Im)
Ie = np.array(Ie)
Id = np.array(Id)

PHItot = []
PHItot.append(PHI2[:])
PHItot.append(PHI[1:])
PHITOT = np.concatenate(PHItot)
PHITOT = np.array(PHITOT)

Entot = []
Entot.append(En2[:])
Entot.append(En[1:])
EnTOT = np.concatenate(Entot)
EnTOT = np.array(EnTOT)
print len(En[1:]), len(Ie)
Eeff_folder = "A directory stored all results of same q1 and q2"
if not os.path.exists(Eeff_folder):
    os.makedirs(Eeff_folder)
```

```
for J in Jlist:
    EFFI = Ie/Id - J*Im/Id
    EFFIintg = [] #### half of En_tot
    EFFIintg_tot = [] #### corresponds to En_tot, add the other half
    # when integrate from Emax
    for i in range(1,len(En)):
        effiintg = 0
        for j in range(0,len(En)-i):
            effiintg = effiintg +
            EFFI[len(En)-2-j]*(En[len(En)-j-2]-En[len(En)-j-1])
        EFFIintg.append(effiintg)

    for i in range(0,len(EnTOT)):
        # when integrate from Emax
        if i == 0 or i == len(EnTOT)-1:
            EFFIintg_tot.append(0)
        if 0< i <(len(En2)):
            EFFIintg_tot.append(EFFIintg[-i])
        if i >= (len(En2)) and i < (len(EnTOT)-1) :
            EFFIintg_tot.append(EFFIintg[i-len(En2)+1])

    EFFIintg_tot = np.array(EFFIintg_tot)
    #### Recording into file
    Eeff_file = Eeff_folder +"/Eeff vs\
    PHI_alphaEff_J="+str(J)+"_q1="+str(q1)+"_q2="+str(q2)+".txt"
```

```
output = open(Eeff_file, 'w')
outputData = np.transpose(np.array([PHITOT[:], EFFIintg_tot[:]]))
np.savetxt(output, outputData, fmt="%12.6g")
output.close()

E_file = Eeff_folder +"/Econs vs PHI.txt"
outputE = open(E_file, 'w')
outputDataE = np.transpose(np.array([PHITOT[:], EnTOT[:]]))
np.savetxt(outputE, outputDataE, fmt="%12.6g")
outputE.close()
```
